Projected changes in Northern Hemisphere permafrost in temperature stabilization and overshoot scenarios

by

Nesha Wright

B.Sc., St. Francis Xavier University, 2017

Thesis Submitted in Partial Fulfillment of the

Requirements for the Degree of

Master of Science

in the

Department of Geography

Faculty of Environment

SIMON FRASER UNIVERSITY

Spring 2020

Approval

Name:	**Nesha Wright**
Degree:	**Master of Science**
Title:	**Projected changes in Northern Hemisphere permafrost in temperature stabilization and overshoot scenarios**
Examining Committee:	**Chair:** Dr. Suzana Dragicevic Professor
	Kirsten Zickfeld Senior Supervisor Associate Professor
	Diana Allen Supervisor Professor Department of Earth Sciences
	Karen Kohfeld Internal Examiner Professor School of Resource and Environmental Management
Date Defended/Approved:	January 20, 2020

Abstract

Achieving the Paris Agreement goal of "holding the increase in global temperature to well below 2°C above pre-industrial levels" is increasingly challenging. Overshoot trajectories, which assume that a temperature target is reached after temporarily exceeding it, are becoming prominent in policy discussions. This thesis explores the long-term response of northern permafrost in temperature overshoot and stabilization scenarios used for the 6th Phase of the Coupled Model Intercomparison Project (CMIP6). The University of Victoria Earth System Climate Model, an Earth System model of intermediate complexity, is forced with a range of CMIP6 scenarios. Results suggest that permafrost recovery lags the decrease in surface air temperature associated with overshoot scenarios. Depending on the scenario, 15-30% of permafrost area is lost at the time temperature is restored to the level prior to the overshoot. Furthermore, in high temperature stabilization scenarios permafrost continues to thaw after global mean temperature is stabilized.

Keywords: permafrost; Arctic; overshoot scenarios; climatology

Acknowledgements

I would like to acknowledge and thank my senior supervisor Dr. Kirsten Zickfeld for not only their on-going support and guidance but her patience throughout the research process. I appreciate the time and energy spent to help me understand Earth System components and the field of climate modelling. In addition, Dr. Zickfeld put a substantial amount of effort into commenting on my academic writing. Further, I thank Dr. Diana Allen for her insight and resources in helping me understand permafrost in a changing climate.

In addition, I thank Dr. Nadine Mengis and Dr. Julien Chaput who have been extremely patient in helping me work with Matlab, along with Claude-Michel Nzotungicimpaye, Rachel Chimuka and the rest of the Climate Lab for their help with editing and providing feedback.

Finally, I thank my family and friends who supported me during my studies.

This research was funded by a Natural Sciences and Engineering Research Council of Canada (NSERC) Discovery Grant awarded to Dr. Kirsten Zickfeld.

Table of Contents

List of Tables

List of Figures

Chapter 1. Introduction

Climate change is an increasingly relevant challenge. In recent years, climate change has influenced extreme weather events such as heat waves, droughts, floods and wildfires (Jeong et al., 2016; Jolly et al., 2015; Pachauri, 2014). These events have increased globally in both frequency and intensity (Jeong et al., 2016; Pachauri, 2014), leading to additional stress on the environment and subsequently on agriculture, human health and the global economy (Mladjic et al., 2011; Pachauri, 2014). Other Earth system responses to climate change include, but are not limited to, ocean acidification (Movilla, 2019; Pendleton et al., 2019), a decrease in snow cover (Bokhorst et al., 2016), glacier retreat (Purdie et al., 2014) and, ice and permafrost melt in polar regions (Anisimov et al., 2007; Biskaborn et al., 2019; Quinton et al., 2016). Adapting to a changing climate supports the need for a better understanding of how the Earth's climate could change in the future.

International policy initiatives aim to achieve a future that includes lower greenhouse gas emissions. The objective of the Paris Agreement, an international accord designed within the United Nations Framework Convention on Climate Change, is to "…Strengthen the global response to the threat of climate change by holding the increase in global temperature to well below 2 °C above pre-industrial levels and to pursue efforts to limit the temperature increase to 1.5 °C" (Adoption of Paris Agreement, Article 2.1 (a), 2015). Recent studies suggest the Paris Agreement target of remaining below a 2 °C atmospheric temperature change will be difficult to meet, given current policy, global fossil fuel consumption and insufficient pledges to reduce emissions in the future (Fuss et al., 2016; Rogelj et al., 2016; Search et al., 2016). Without more aggressive climate policies, it is likely the 2 °C target will not be achieved, and an overshoot scenario will be necessary to meet the temperature target in the long term (Fuss et al., 2016; Lowe et al., 2009; Search et al., 2016). An overshoot scenario is

one in which the temperature is restored to the target level after temporarily exceeding it.

An overshoot scenario requires net negative emissions to obtain a reversal in temperature (Tokarska & Zickfeld, 2015a). Negative emissions are achieved through carbon dioxide removal (CDR) techniques to artificially remove CO_2 from the atmosphere. Emissions are said to be "net negative" when more carbon is being removed than is being emitted. Although CDR technologies are still in the early phases of development and have yet to be tested to scale, policy is beginning to consider these technologies in future emissions scenarios (Schäfer et al., 2015; Smith et al., 2016; Vaughan & Gough, 2016).

The primary reason net negative emissions are required to reverse temperature is ocean thermal inertia and the long atmospheric lifetime of CO_2 , which remains in the atmosphere for many centuries to millennia (Eby et al., 2009). Due to this characteristic, reducing CO_2 emissions is not sufficient to achieve a decline in temperature (Tokarska & Zickfeld, 2015). Even reducing CO_2 emissions to zero attains stable, but not decreasing temperature (Gillett et al., 2011; Matthews & Caldeira, 2008). The relationship between atmospheric CO_2 emissions and atmospheric temperature is illustrated in panels (a) and (c) of Fig. 1. A decrease in temperature is not attained until net emissions have dropped below zero.

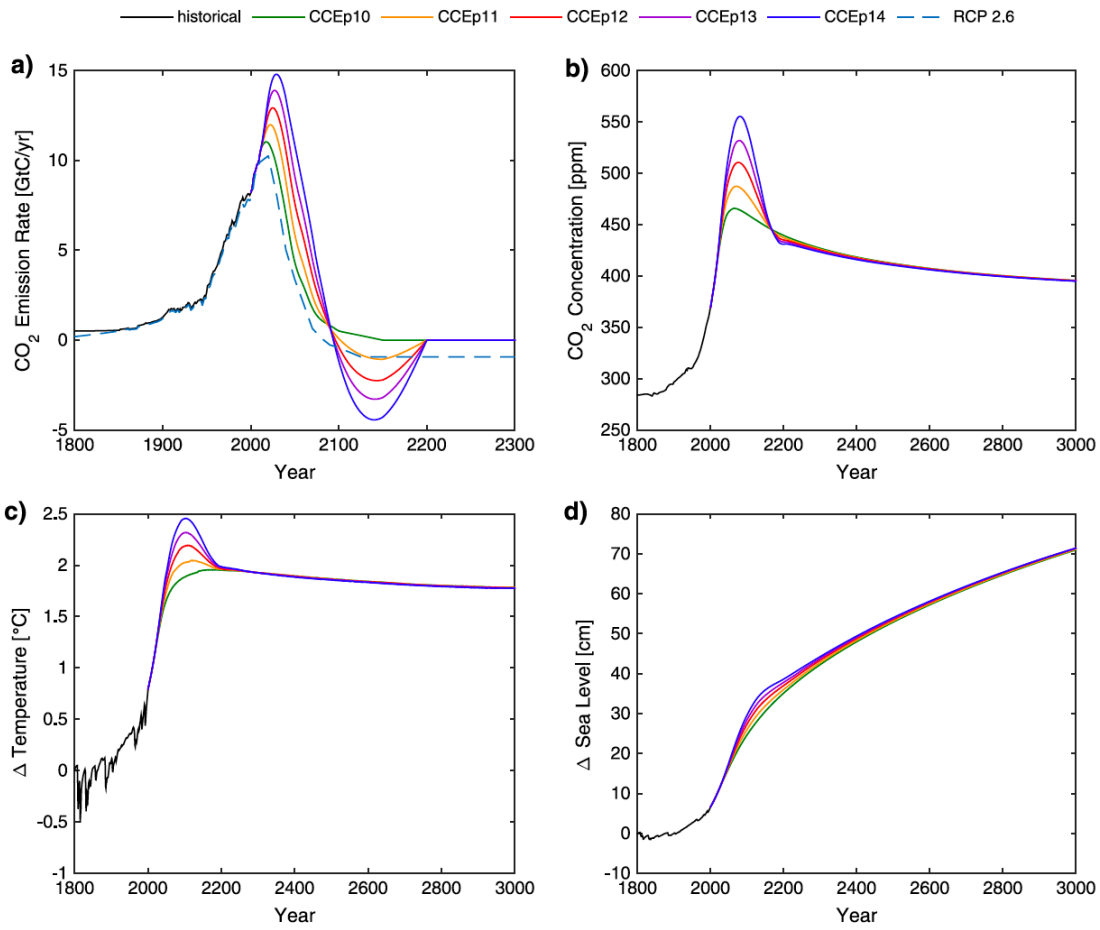

Figure 1.1: (a) CO_2 emissions rate (from both land use change and fossil fuels), (b) atmospheric CO_2 concentration, (c) global mean temperature change (relative to 1801) and (d) thermostatic sea level rise (relative to 1801). Each scenario has a different fossil fuel emissions rate by the year 2100. The dashed green line in panel (a) is RCP2.6 for reference. Note that graph (a) has a different x-axis scale indicating the emissions rate becomes negative just before 2100. Source: Tokarska & Zickfeld (2015), used with permission.

The ability to reverse the effects caused by an increase in temperature for many different components of the Earth system, such as surface air temperature, ocean heat storage and sea level rise, terrestrial carbon content, ocean pH and sea ice changes, has been studied in the context of scenarios where atmospheric CO_2 and surface air temperature decline after reaching a peak (Boucher et al., 2012; Jones et al., 2016; Macdougall, 2013; Tokarska & Zickfeld, 2015; Zickfeld et al., 2016). The time scale on which these variables respond to a decline in atmospheric CO_2 has been found to be

variable and depends on the time scale of the processes involved. Surface air temperature has been determined to have a short lag time relative to a decline in atmospheric CO_2 and therefore to recover quickly (Tokarska & Zickfeld, 2015; Frölicher et al., 2010; Boucher et al., 2012). Global mean precipitation, on the other hand, shows a lag in response to a decline in atmospheric CO_2 (Boucher et al., 2012). Reversal of ocean carbon uptake occurs on time scales of several decades to centuries, due to its dependency on deep ocean mixing (Boucher et al., 2012). Ocean surface pH has been shown to reverse quickly; however, deep ocean pH is slow to reverse due to the long time scale of ocean mixing (Li, 2017). Processes such as ocean heat uptake and ocean thermal expansion require decades to reverse in response to a decline in atmospheric CO_2 (Ehlert & Zickfeld, 2018; Tokarska & Zickfeld, 2015b).

Permafrost is of interest in reversibility studies because of its century-scale response to temperature (Boucher et al., 2012). While a decline in permafrost extent in modelling studies has been shown to be reversible within centuries (Boucher et al., 2012), the loss of carbon content within the permafrost is irreversible on a centennial time scale (Biskaborn et al., 2019; Boucher et al., 2012; Macdougall, 2013).

The influence that an increase in temperature will have on permafrost is poorly understood due in part to the complex nature of the processes individually and few filed studies in permafrost regions. It is vital that the response of permafrost be better understood since it plays a key role in high latitude processes and systems (Chadburn et al., 2017; Loranty et al., 2018; Natali et al., 2014). Permafrost degradation affects soil properties, microbial activity and the release rate of the greenhouse gases CO_2 and CH_4 (Avis et al., 2011; Natali et al., 2014; Zhang et al., 2017). As a result of permafrost degradation, microbial activity increases and CO_2 and CH_4 are released into the atmosphere (Johnston et al., 2019; Schuur & Abbott, 2011; Schuur et al., 2009). Since CO_2 and CH_4 are greenhouse gases, there is concern that permafrost degradation will amplify global warming (Zona, 2016; Schuur et al., 2015).

The presence of permafrost in Arctic and sub-Arctic regions also influences physical processes at high latitudes. For example, permafrost acts as a barrier for soil moisture movement. With warmer temperatures becoming more frequent, this barrier will disappear allowing moisture previously trapped within the top soil layers to move deeper, resulting in a drier top layer. This dry top soil layer will influence vegetation cover and the distribution of wetlands (Avis et al., 2011; Walvoord & Kurylyk, 2016). A change in the subsurface structure caused by ice and permafrost melt will decrease the moisture held in the soil. This change in soil moisture will lead to a decrease in soil stability and increase forest fire frequency and severity causing further permafrost thaw (Brown, 2014; Gibson et al., 2018; Jones et al., 2015; Olefeldt et al., 2016; Pastick et al., 2017). Furthermore the type of ecosystem will change (Pastick et al., 2019), thereby altering migration routes (Berteaux et al., 2017) and causing infrastructure challenges (Hjort et al., 2018; Kanevskiy et al., 2013; Raynolds et al., 2014) due to the change in subsurface structure and therefore stability of the ground. For example, roadways and building legislation and code across the north are rapidly changing to try to adapt to the increase in a changing subsurface (Hjort et al., 2018). Recent studies show that roughly 20% of the permafrost region is susceptible to abrupt thaw (Olefeldt et al., 2016) and that with an increase in thermokarst landscapes and water pooling, there will be a further decrease in permafrost extent (Nitze et al., 2017; Pastick et al., 2019; Ulrich et al., 2017).

Our understanding of how the extent and characteristics of permafrost will evolve in the future is limited (Boucher et al., 2012; Loranty et al., 2018; MacDougall, 2013), particularly in response to overshoot scenarios. Since climate reversibility and overshoot scenarios are new concepts, few studies have explored the Earth system response to these types of scenarios. With climate change affecting the north disproportionally in comparison to lower latitude regions, and overshoot scenarios being considered in current policy discussions, Arctic and sub-Arctic permafrost response to these scenarios requires further research.

With temperature being a primary driver of permafrost thaw (Schuur et al., 2015), this research was designed to answer the following research questions:

1. What are the effects of different levels of warming on the spatial extent of permafrost in the circumpolar north on multi-century time scales?

2. What are the effects of warming on permafrost spatial extent in the circumpolar north under different emission scenarios with the same resulting level of warming?

These two research questions are addressed by studying the response of Arctic and sub-Arctic permafrost spatial extent using the University of Victoria Earth System Climate Model (UVic ESCM) (Weaver et al., 2001), a global model of intermediate complexity, driven by a set of future scenarios following the Coupled Model Inter-comparison Project Phase 6 (CMIP6) protocol (Eyring et al., 2016).

The structure of the remainder of this thesis consists of four sections: Methods, describing the UVic model, components and the scenarios run in this study, Results, divided into subsections for each type of scenario, Discussion and Conclusions, and an Appendix with additional details regarding the creation of CMIP6 forcing data not included in the main body of this thesis.

Chapter 2. Methodology

2.1. Model Description

This research employs the University of Victoria Earth System Climate Model (UVic ESCM, version 2.10), (Mengis et al., in prep.). The UVic ESCM is a model of intermediate complexity (EMIC) with global coverage and a grid resolution of 1.8˚ x 3.6 ˚ (Weaver, 2001). The atmospheric model is a simplified two-dimensional energy moisture balance model (Fanning & Weaver, 1996). It is coupled to a thermodynamic sea-ice model (Bitz et al., 2001) and a three-dimensional ocean general circulation model (the Geophysical Fluid Dynamics Laboratory Modular ocean model 2.2, with 19 vertical layers), (Pacanowski et al.,1995), including both inorganic and organic carbon cycles (Keller2012). The UVic ESCM contains a land surface model (Hadley Center Met Office surface exchange scheme model, MOSES), with the inclusion of permafrost, a vegetation dynamics model, TRIFFID (Top-down Representation of Interactive Foliage and Flora including Dynamics) and a terrestrial carbon cycle model which is based on the Met Office Surface Exchange Scheme (MOSES), (Avis, 2012 and Meissner et al., 2003). The model also includes a permafrost carbon pool. Figure 2.1 illustrates how the model components are connected through water, energy and carbon fluxes.

The model components are coupled at different timesteps. For example, the land-atmosphere fluxes are calculated every 6 hours and coupled to the atmosphere and ocean every 2.5 simulation days but the vegetation model (TRIFFID) and the land-atmosphere fluxes are coupled every 30 days. The ocean and atmosphere are coupled every two ocean timesteps (a single ocean timestep is 5 simulation days) at which point the atmosphere has completed four timesteps.

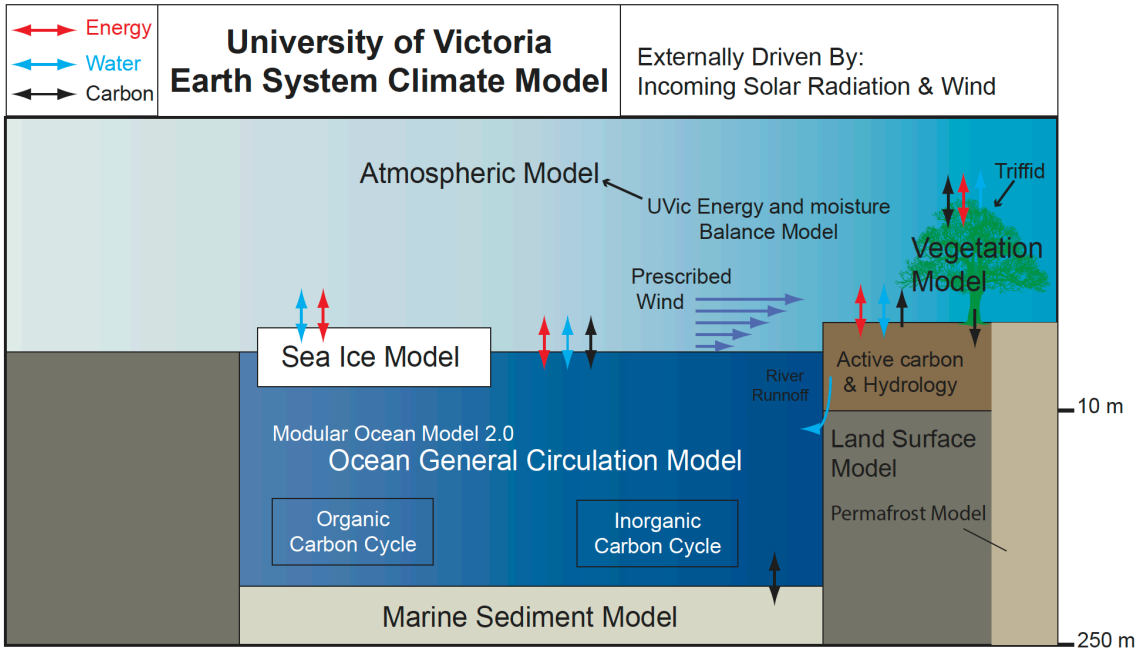

Figure 2.1: A schematic of the UVic Model components and how they are interconnected through energy, water and carbon. Figure reproduced from MacDougall et al. (2015), used with permission.

2.1.1. Atmospheric Model

The atmospheric model is a two-dimensional energy moisture balance model that solves energy and moisture balance equations at the Earth surface. The module accounts for atmospheric heat sources and sinks (Avis, 2012). By including moisture balance in the atmospheric model, latent heat is explicitly determined within the model (Fanning et al., 1996). Given its simplified components, atmospheric heat and fresh water transports are parameterized using Fickian diffusion (Weaver et al., 2001). In addition, it is assumed precipitation will occur if the relative humidity is over 85 % (Weaver et al., 2001). Moisture diffusion is parameterized but varies with latitude (Weaver et al., 2001). The parameterization of long-wave radiation is dependent on temperature and surface relative humidity (Weaver et al., 2001). Heat absorption in the atmosphere is parameterized by an absorption coefficient to represent clouds, water vapour, ozone and dust.

The lapse rate is the change in atmospheric temperature with elevation and is determined primarily by radiation and influenced by the amount of water vapour in the air. In the UVic model, the lapse rate is globally averaged and determined using the outgoing long-wave radiation, surface air temperature (with consideration of the planetary albedo) and specific humidity (Weaver et al., 2001).

Precipitation in the model occurs in the form of snow or rain. For precipitation to occur, the relative humidity must be greater than a pre-determined threshold value of 85 %. To determine if precipitation will occur in the form of snow (over land) instead of rain, the surface air temperature must fall below a pre-defined critical value (-5.0 ˚C).

One of the primary simplifications within the atmospheric model is the use of prescribed winds, instead of having them simulated within the model. Wind stress climatology is determined as the average wind stress over the years 1958-1998 from daily reanalysis data. This data are then converted to wind speed and wind stress and used in the ocean and sea ice models to calculate components such as latent and sensible heat flux, and wind driven ocean circulation (Weaver et al., 2001). Because the atmospheric model does not simulate changes in wind dynamics, wind stress anomalies are parameterized in terms of surface air temperature anomalies (Weaver et al., 2001). There are no cloud feedbacks within the atmospheric model due primarily to the simplicity of the model, but also due to the poor understanding of the physics behind cloud dynamics (Weaver et al., 2001).

2.1.2. Land Surface Model

Representation of land surface processes is through the use of a simplified version of the Met Office Surface Exchange Scheme (MOSES) model, developed by the Hadley Center (Meissner et al., 2003). MOSES uses a surface energy budget, calculated for each grid point and based on three different temperatures: near surface air temperature, soil (ground) temperature and the surface (skin) temperature.

The land surface model consists of 14 subsurface layers. By default, the top 8 layers, to a depth of 10 m, are soil, while the bottom 6 layers, to a depth of 250 m, are bedrock. MOSES further classifies mineral soil based on texture into three classes, fine, medium and coarse (Avis, 2012). The UVic model mineral soil characteristics were initially limited to the medium soil class. To improve accuracy the model was updated to reflect grain size more accurately by using a grain size distribution based on the International Satellite Land Surface Climatology Project Initiative 2 (ISLSCP II Global Gridded Soil Characteristics, 2011) (Avis, 2012). Organic soil is also considered in the land surface model. Organic soils have low thermal conductivity and high hydraulic conductivity and porosity relative to mineral soil. Model simulations were run with a uniform soil to bedrock transition occurring at 10 m depth.

The near surface air temperature is dependent on the fluxes of latent heat, sensible heat and radiation between the surface and atmosphere and the ground heat flux (Avis, 2012). The energy balance at the surface can be simplified as:

$$Q = Q_H + Q_E + Q_G \tag{2.1}$$

where Q is the net radiation at the surface (W/m^2), Q_H is the sensible heat flux (W/m^2), Q_E is the latent heat flux (W/m^2) and Q_G is the ground heat flux (W/m^2) (Woo, 2012).

The sensible heat flux between the land surface and the atmosphere is primarily dependent on the temperature gradient between the surface temperature and the near surface air temperature. The latent heat flux is predominantly determined by the difference in specific humidity between the surface and near surface, although aerodynamic resistance due to wind speed and vegetation height is also accounted for (Avis, 2012). The degree of turbulent mixing in the atmosphere and the snowpack influence both the latent and sensible heat fluxes between the surface and the air in the lower atmosphere (Avis, 2012).

The ground heat flux occurs by diffusion due to the temperature gradient between soil layers and by the advection of water (Avis, 2012). The temperature of each soil layer below the surface is calculated by solving the following equation:

$$C_{s,n}\Delta z_n \frac{dT_{g,n}}{dt} = G_{n-1} - G_n + J_n \tag{2.2}$$

where C_s is soil heat capacity, z_n is the thickness of soil layer n, $T_{g,n}$ is the temperature of soil layer n, G_n is the heat transported by diffusion through the base of layer n, and J_n is the heat transported by advection of water into layer n.

It should be noted that the model simulates the heat flux between soil and bedrock layers (Avis, 2012). For each soil layer, the organic and mineral content, and the liquid moisture content (relative to saturation) are used to determine the thermal and hydrological soil parameters, and therefore, the volume of water (in liquid form) that is transported through the soil (Avis, 2012). In the bedrock, both the heat capacity and thermal conductivity are constant (Avis, 2012). The characteristics of granite are used for the thermal conductivity (3.4 W/m/K) and specific heat capacity (2400000 J/kgK) of the bedrock layers in the UVic ESCM (Avis, 2012).

Within the soil, moisture is transported by gravity and capillary forces, and moves only vertically to the depth of bedrock (10 m) at which point it becomes runoff and is laterally transported off the grid using the river routing scheme (Figure 2.2) (Avis, 2012). The exception is if the rate of precipitation is greater than the hydraulic conductivity of the soil. In that case excess water is sent directly to the river routing system as runoff (Avis, 2012). Terrestrial snow is treated as an extension of the top layer of the land surface scheme rather than separately, since it is a single layer and provides insulation. Snow within the model has no heat capacity and both its thermal conductivity (.25 W/m/K) and density (330 kg/m^3) are constant.

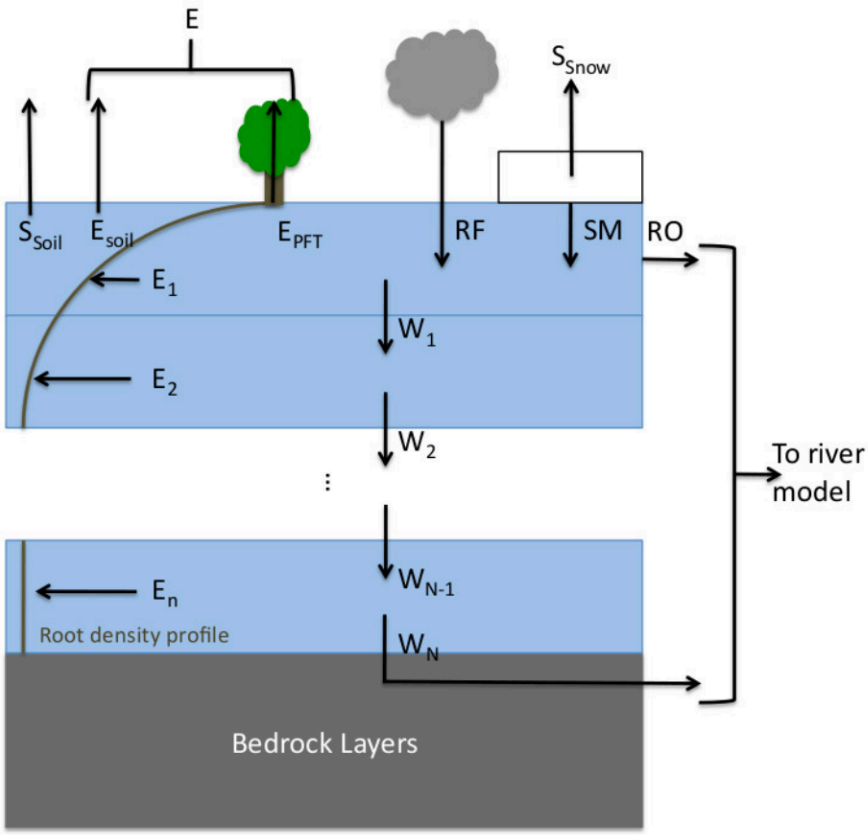

Figure 2.2: Soil moisture fluxes within the UVic Earth System Climate Model. E is evapotranspiration, S is sublimation, W is the water flux (downwards), PFT are the plant functional types, RF is rainfall, SM is snowmelt and RO is runoff. Reproduced from Avis (2012). Figure used with permission.

The presence of permafrost is determined using Equation 2.2 and the standard definition of permafrost: a soil layer that remains frozen for two or more consecutive years. Each soil layer is assessed individually to determine if the layer is permafrost. If one of the layers is permafrost, the grid cell becomes part of the permafrost region.

2.2. Model Simulations

Figure 2.3 shows the timeline of the different model simulations. The various simulation periods are described in detail below.

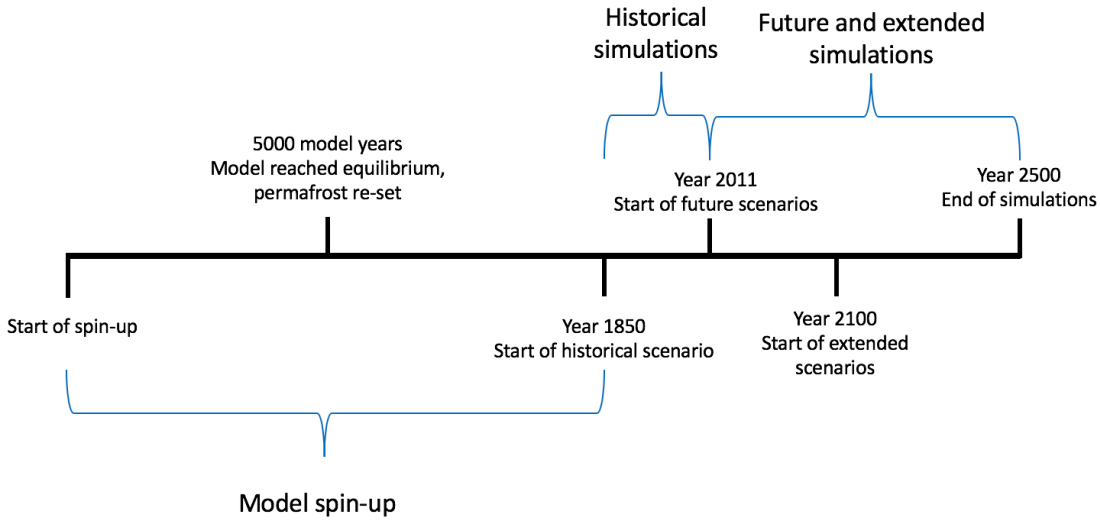

Figure 2.3: Simulation time line. The various simulation periods are described in detail below

2.2.1. Spin-up simulation

The spin-up simulation is used to bring the model to equilibrium given a certain set of radiative forcings. For this study, to be consistent with the protocol of the Coupled Model Intercomparison Project Phase 6 (CMIP6), year 1850 forcing was used (Eyring et al., 2016). The model was run with 1850 forcing data, including CO_2 concentrations, non-CO_2 greenhouse gas (GHG) radiative forcing, aerosol optical depth, land use patterns, and ozone. As defined by CMIP6 protocol, volcanic forcing was implemented as an anomaly relative to the historical period and accordingly set to zero throughout the spin up. Following CMIP6 protocol, the solar forcing during the spin up was set to the mean of the first two solar cycles in the historical period, i.e., the mean of 1850-1873. The spin up was run in two stages, the first 5000 years were run to equilibrate the land, ice and atmosphere. Thereafter, the soil carbon pool was reset. An additional 5,000 model years were simulated to reach a dynamic and equilibrated land carbon pool, and to allow the deep ocean to equilibrate with the prescribed forcing. The climate state at the end of the spin-up simulation was used to initialize the historical simulation.

2.2.2. Historical simulation (1850-2010)

To be consistent with CMIP6 protocol, the historical period began in 1850 and ended in 2010 (Eyring, 2016). 2010 was used as an end date for the historical period to be compatible with the start point of the future pathways (section 2.2.3). The forcing data for the historical simulation included observations-based CO_2 concentrations, non-CO_2 GHG radiative forcing (Meinshausen et al., 2017), aerosol optical depth (Stevens et al., 2017), land use (Hurtt et al., in prep.), ozone (Smith et al., 2018), volcanic (Schmidt et al., 2018a) and solar forcings (Matthes et al., 2017).

2.2.3. Future simulations (2010-2100)

The Shared Socio-economic Pathways (SSPs) were developed to provide scenarios based on different socioeconomic development in combination with different levels of radiative forcing by the year 2100. The five pathways (SSP1-SSP5) range from high mitigation and low fossil-fuel dependency (SSP1) to minimal mitigation and high fossil-fuel dependency (SSP5). The SSP scenarios are combined with different levels of radiative forcing; for example, SSP5-3.4 is a scenario which follows the SSP5 pathway and has a radiative forcing of 3.4 Wm^2 in the year 2100 (O'Neill et al., 2016).

Future scenarios in this study are based on SSPs from 2010 to the year 2100 as defined by O'Neil et al. (2016). Six scenarios were chosen: SSP1-1.9, SSP1-2.6, SSP4-3.4, SSP4-6.0, SSP5-3.4-OS and SSP5-8.5. These include, an overshoot (OS) scenario (SSP5-3.4OS) wherein the target radiative forcing is temporarily exceeded. An additional scenario was designed for the purpose of determining the impact of the magnitude and duration of overshoot. This scenario, referred to as SSP4-3.4w2.6, follows SSP4-3.4 to the peak surface air temperature of the overshoot at which point the forcing of SSP1-2.6 is followed to allow for surface air temperature to converge with SSP1-2.6. In the future simulations, natural forcings (volcanic and solar) are prescribed. Anthropogenic forcing in these simulations is prescribed in terms of CO_2 concentration, radiative forcing from non-CO_2 greenhouse gases, ozone, aerosol optical depth and land-use change for each

scenario. The forcing is specific to each scenario and the details of how each forcing was created can be found in Appendix A. The prescribed atmospheric CO_2 concentrations for the SSPs used in this study are shown in Figure 2.4. Note that due to atmospheric CO_2 being prescribed, carbon released from carbon stores (including the permafrost carbon store) due to warning has no effect on temperature.

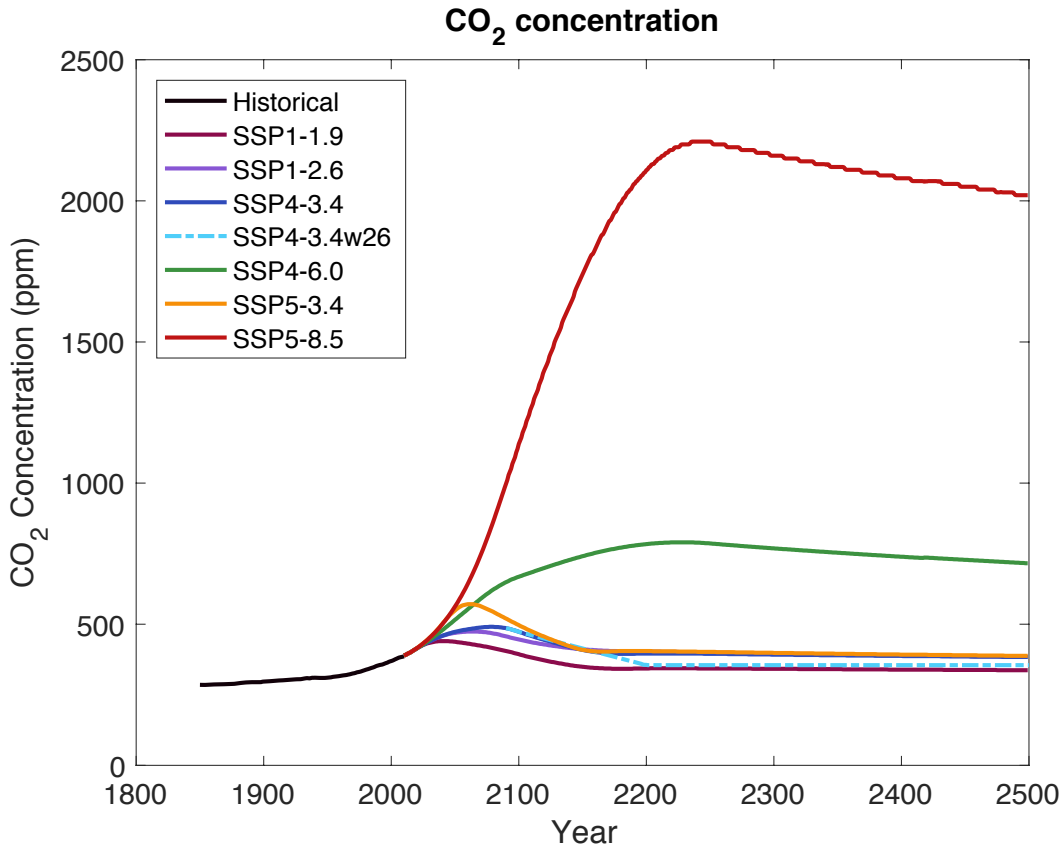

Figure 2.4: Atmospheric CO_2 concentrations for each of the Shared Socio-economic Pathways used in this study.

2.2.4. Future Extensions (2100-2500)

The forcing data used to the year 2100 was extended to allow for simulations to run to the year 2500. In this study, CO_2 concentrations, radiative forcing from non-CO_2 greenhouse gases and ozone were prescribed to the year 2500 (Meinshausen et al., 2017) while aerosols and land-use were held constant at year-2100 levels. Solar forcing is prescribed to 2300 (Matthes et al., 2017) and from 2300 to 2500 repeats the last 13-

year solar cycle. Volcanic forcing is prescribed to 2018 and held at the mean value between 1850 and 2018 to the year 2500.

2.2.5. Stabilizations Scenarios

To investigate the response of permafrost area when global mean surface air temperature remains stable additional scenarios were developed. These scenarios branch off from SSP5-8.5 when a specified warming level is achieved. In the years 2044, 2065 and 2107 global mean surface air temperature was held constant by forcing the UVic ESCM with zero CO_2 emissions and holding all other forcing variables constant. Note that in contrast to the SSP scenarios, carbon released from the different stores (including permafrost) after the year emissions are set to zero affects temperature. The stabilization scenarios are named referring to the forcing they follow (SSP5-8.5) and the target temperature stabilization level (2 °C, 3 °C and 6 °C).

2.3. Model Execution and Model Output

The UVic ESCM simulations were run on the High-Performance Computer Cedar located on the Burnaby campus of Simon Fraser University, BC, Canada accessed through Compute Canada.

The model output is in the form of NetCDF data. The two output formats include spatial annually averaged data (output every year for the historical simulation and every ten years for future simulations) and global, annually averaged data for each year. Any spatial data is formatted internally from grid cell size dimensions to metric units for ease of use.

Chapter 3. Results

3.1. Model Validation

Model validation was done by comparing output from the historical model simulation (1850-2010) with observational data. Variables include the near surface air temperature, active layer thickness, permafrost area and depth, and both ground surface (intercept between atmosphere and the ground) and subsurface temperatures.

While the datasets used in this study include observations covering both Canada and the circumpolar Arctic there are limitations that need to be considered when comparing the observed data to the UVic ESCM simulations. Limitations are discussed in detail within the sections of the variable they pertain to. The permafrost module of the UVic ESCM was evaluated previously for an earlier model version (Avis, 2012).

3.1.1. Near Surface Air Temperature

Surface air temperatures influence not only the ground surface and subsurface temperature but the amount of snow, the type of precipitation and the vegetation that grows. Here, the UVic ESCM near surface air temperature will be compared to the observed near surface air temperature dataset of Jones et al. (1999) for the period of 1961 to 1990. Jones et al. (1999) provide a comprehensive dataset that interpolates observed station data to a grid. Individual station data was required to have at least 20 years of values during this 29-year period and was averaged monthly, and then annually, to allow for comparison to the UVic ESCM simulation.

In Figure 3.1 the difference between the simulation and the observed near surface air temperature shows that there is a warm bias over North America and Russia. Simulated near surface air temperature over northeastern Canada is estimated to be between 5.0 °C and 7.5 °C too warm compared to observations, and over eastern Russia (Sakha Republic) is estimated to be between 7.5 °C and 10.0 °C too warm compared to

observations. Along the coast of the Scandinavian countries the UVic ESCM simulated near surface air temperature is too cold by roughly 5 °C to 7.5 °C.

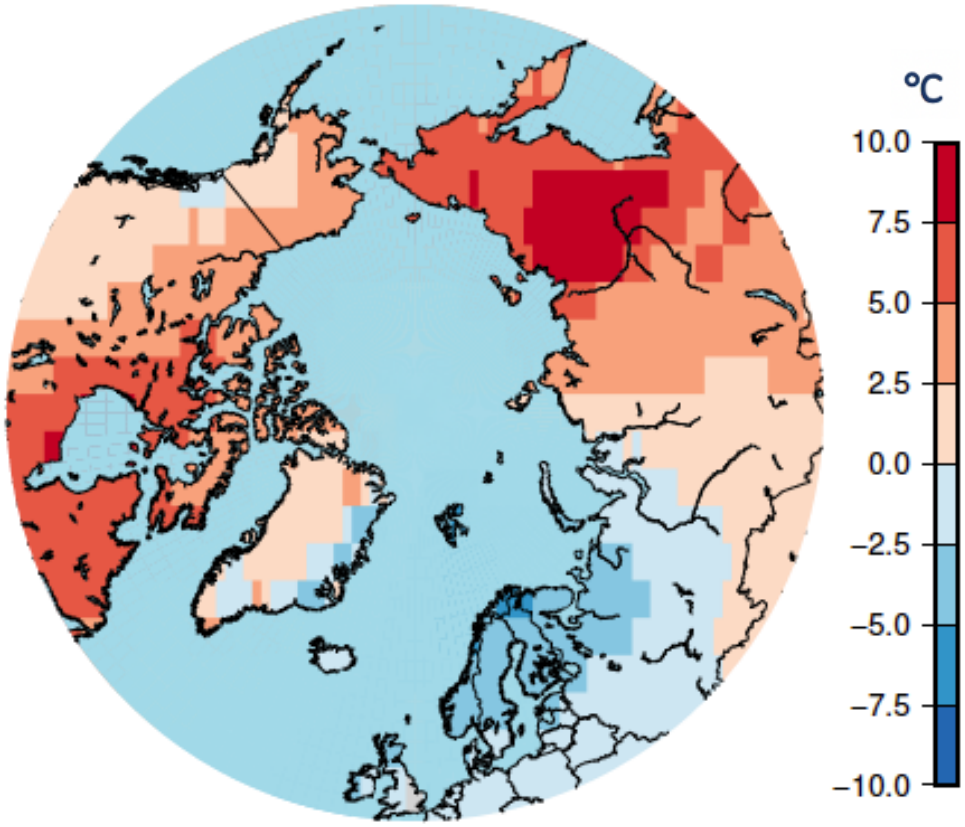

Figure 3.1: Surface air temperature bias in the UVic ESCM for the period 1961 to 1990 compared to the observational dataset of Jones et al. (1999).

3.1.2. Active Layer Thickness

Accurately representing the active layer is important for a number of reasons. Foremost is the fact that an accurate active layer ensures that the heat transfer through the subsurface soil layer is correctly simulated, and therefore, impacting the permafrost layer correctly. The active layer is the layer located above permafrost which seasonally freezes and thaws. A bias in the active layer could introduce bias into the permafrost extent and thickness. Beyond that, the active layer impacts biological, hydrological, pedological and biogeochemical processes (Abbott et al., 2016; Schaefer et al., 2014) .

Active layer thickness observations are sourced from the Circumpolar Active Layer Monitoring Network (CALM) ("Circumpolar Active Layer Monitoring," 2019), which provides a circumpolar active layer thickness dataset for the years 1990 to 2010. Borehole temperatures, in combination with ground temperature measurements and frost and thaw tubes, were used to determine the thickness of the active layer at the end of the thaw season. As a result of borehole and frost/thaw tubes being used, which essentially measure the position of ice in the ground, all the observed data are single measurements. The horizontal and vertical resolution of the UVic ESCM is coarse and covers an area that in reality has varying active layer thickness. Vertical resolution in the model decreases as depth increases (from 0.1 m beneath the surface to 104.4 m at depth). Because of the coarse vertical resolution and the way in which the active layer depth is determined, active layer thickness is underestimated in the model. The model assesses the temperature in each layer and identifies active layer depth as the bottom of the deepest layer that thaws completely. This means that there is a systematic underestimation of active layer depth since layers thawing only partially are not accounted for. Furthermore, the UVic ESCM data are annually averaged, but active layer thickness observations consist of a single measurement taken at the end of the thaw season for a particular year, making this comparison more challenging. As a result of UVic ESCM active layer thickness being annually averaged it is expected that these values will be shallower than the values observed, due to the effects of seasonality on the shallow subsurface.

Figure 3.2 indicates that the model simulates a thicker active layer in Alaska and northern Siberia compared to the observed dataset ("Circumpolar Active Layer Monitoring," 2019) with a difference ranging from approximately 50 cm to 1 m depending on the location. There are a number of areas where the active layer is not simulated correctly. For example, the model does not simulate permafrost or an active layer in eastern Canada, eastern Europe and Mongolia, while the simulated active layer thickness in the Tibetan Plateau is between 100-300 cm too shallow or not simulated at all as a result of no permafrost being simulated.

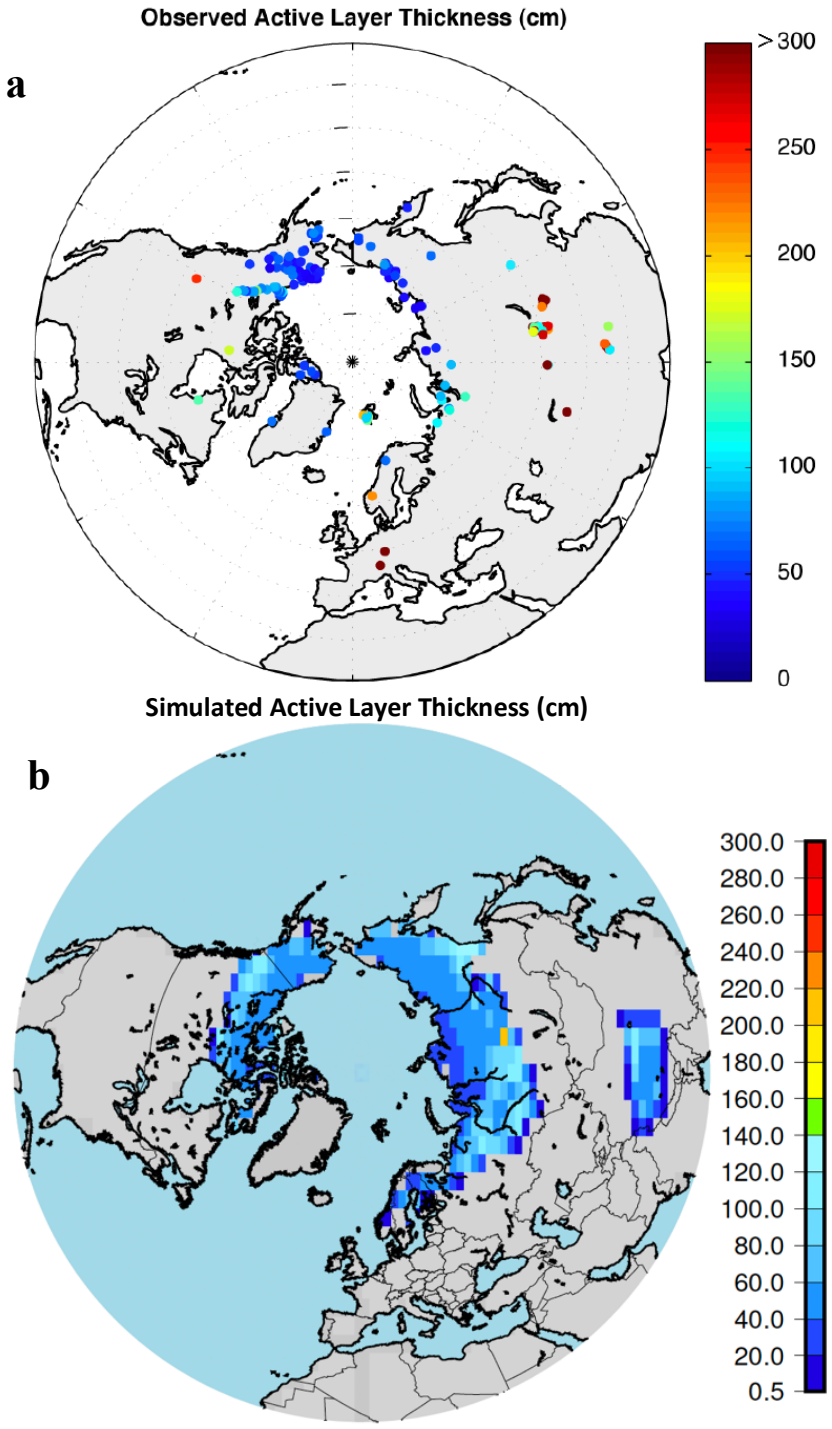

Figure 3.2: (a) Observed mean active layer thickness for the period 1990-2010 from the Circumpolar Active Layer Monitoring Program with additional Canadian Arctic and Sub-Arctic sites ("Circumpolar Active Layer Monitoring," 2019). (b) 1990-2010 annual mean simulated active layer thickness from the UVic ESCM.

Figure 3.3 shows the correlation between the observed active layer thickness ("Circumpolar Active Layer Monitoring," 2019) and simulated active layer thickness. If the active layer was not simulated due to there being no permafrost simulated where that the borehole was located, that location is not represented on the graph (23 observation sites). The clustering of points in the UVic ESCM at specific active layer thicknesses is due to the limited vertical resolution mentioned earlier. Due to the limitations of the model and limited observations this analysis does not provide enough information to evaluate the performance of the model. Previous work with the UVic ESCM found the UVic ESCM to underestimate active layer thickness primarily due to the the coarse vertical resolution of the model (Avis, 2012).

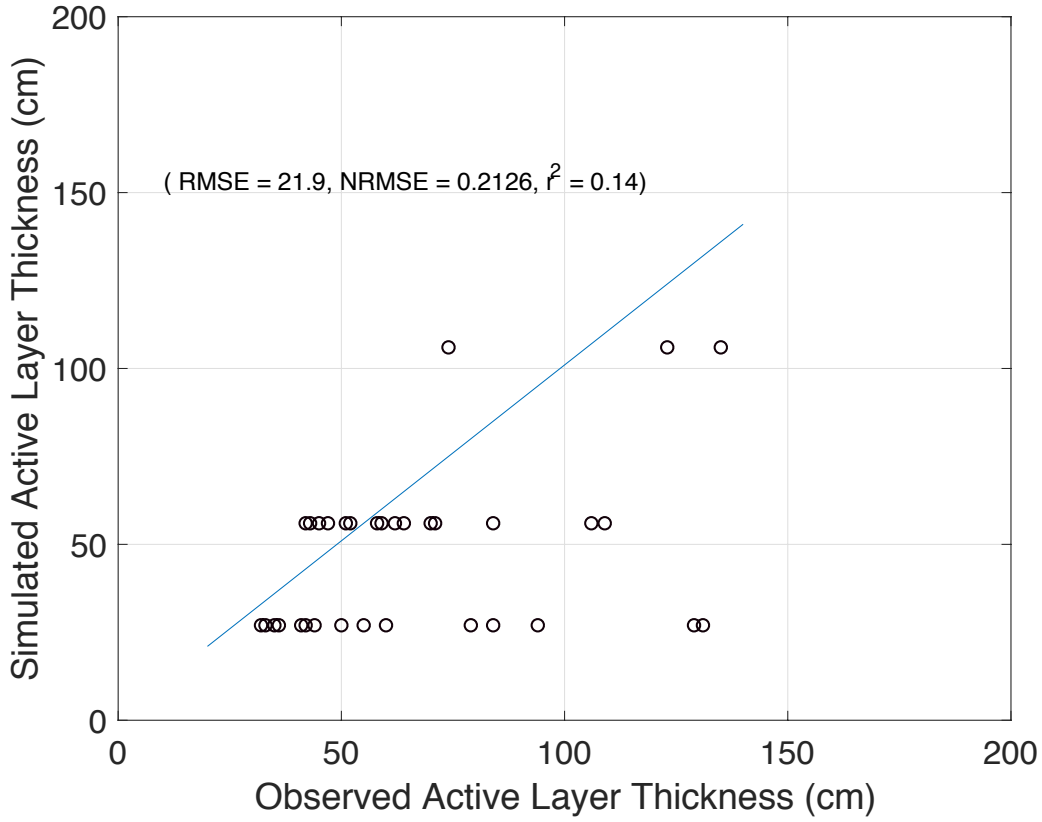

Figure 3.3: Scatter plot comparing the active layer thickness simulated by the UVic ESCM to observations ("CALM Site" 2015) for the period 1990-2000. Root Mean Square Error (RMSE), Normalized Root Mean Square Error (NRMSE) and root squared (r^2) are noted for reference.

3.1.3. Permafrost Area and Depth

The UVic ESCM mean permafrost area for the period 2000-2010 is 16.98 x 10^6 km^2, which underestimates the observed permafrost extent (22.79 x 10^6 km^2; Zhang et al., 2003) by 5.89 x 10^6 km^2 (Table 3.1). Spatial variables in the UVic ESCM are internally calculated; the model equates allocated grid cells to more accessible units, for example, in the case of permafrost, the area is equated to km^2. As discussed in section 2.1.2 a grid cell is allocated as permafrost if a ground layer is deemed to be frozen for two consecutive years.

Brown et al. (1998) created the first permafrost observational dataset. This dataset has since been revised to include more observations and more southern locations. Using a photo editing software, Avis (2012) created a composite permafrost map (Figure 3.4a) composed of the International Permafrost Association (IPA) permafrost map (Brown et al. (1998), created by (Zhang, 2005)) and a map of seasonally frozen ground produced by Zhang et al. (2003). Locations where the permafrost is not accurately simulated in comparison to the permafrost map of Avis (2012; Figure 3.4a) include eastern Siberia and Mongolia where there is a lack of simulated permafrost coverage. In west and central Eurasia simulated permafrost compared to the observations extends too far (Figure 3.4b). For example, in Canada, there is a lack of simulated permafrost near the northern British Columbia and Alberta border (Figure 3.4b). Permafrost area in the UVic model is within the range (11.9 – 26.2 x 10^6 km^2) of other model simulations (Table 3.1).

Table 3.1: Permafrost area estimates from observations (Zhang et al., 2003) ad model simulations.

Reference	**Areal Extent (x 10^6 km^2)**	**Reference Years**	**Comments**
Zhang et al. (2003)	12.1 - 22.79	1998-2000	Observations
Slater & Lawrence, (2013)	11.9	1970-1980	Simulation
Gent et al. (2011)	12.5	1970-1989	Simulation
Koven et al. (2011)	13.5	2000	Simulation (North of 60 deg.)
Saito et al. (2007)	18.1	1980-1990	Simulation
Obu et al. (2019)	21	2000-2016	Simulation
Demchenko et al. (2001)	25.7-26.2	1961-1990	Simulation
Gruber (2012)	13-18	2012	Simulation (North of 60 deg.)
UVic ESCM	**16.9**	**2000-2010**	**Simulation (N. Hemisphere)**

Visual comparison of permafrost area based on observations (Figure 3.4a) to the UVic ESCM distribution (Figure 3.4b) should be limited to continuous (red) and discontinuous (orange) zones, as the UVic cannot simulate isolated or sporadic permafrost due to the definition of permafrost in combination with the land scheme as described in Chapter 2.1.2.

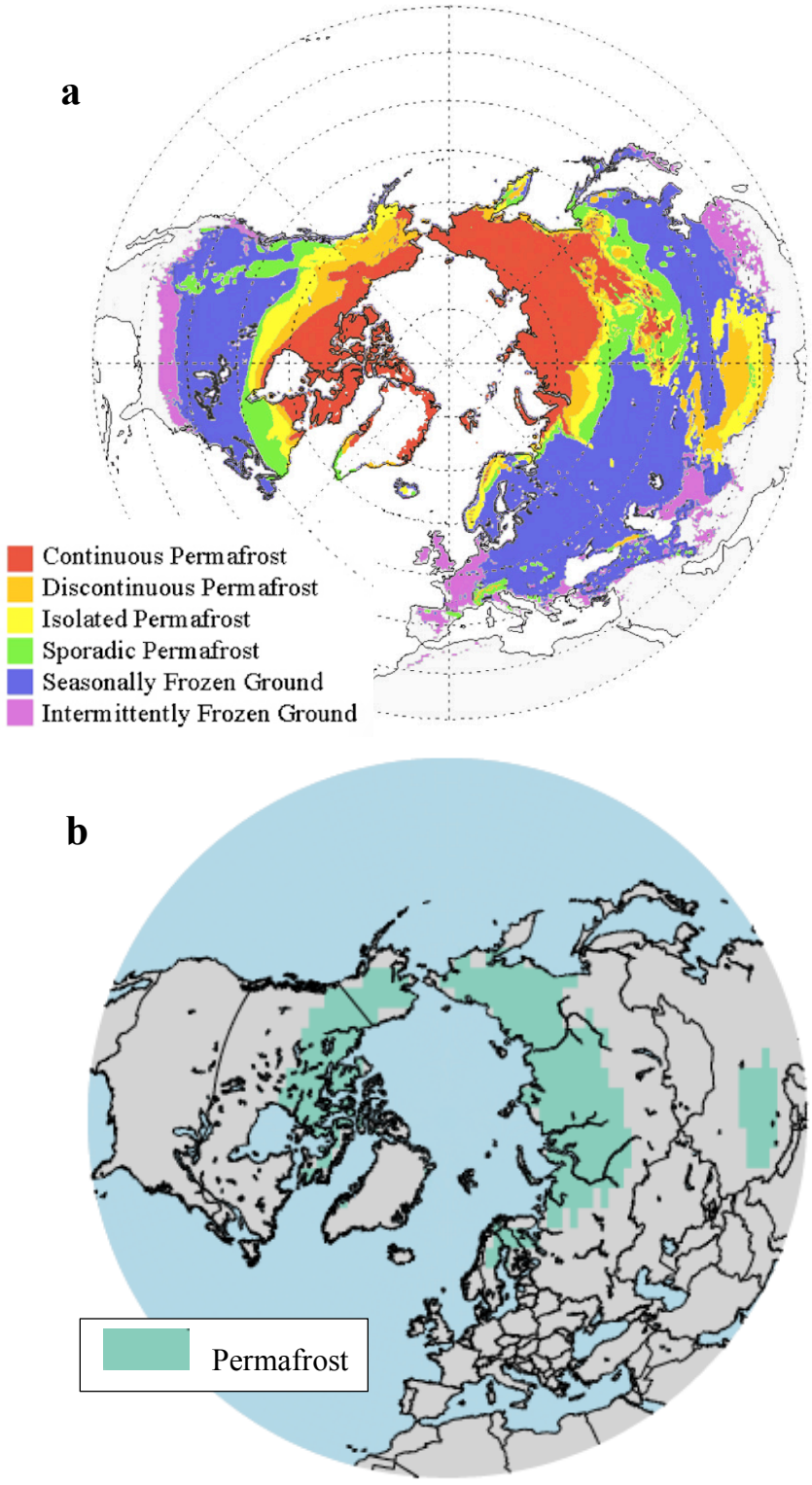

Figure 3.4: (a) Produced by Avis (2012), this map illustrates the permafrost distribution based on observations from Zhang et al. (2003) and Brown et al. (1998). (b) The UVic ESCM model simulation of permafrost thickness (m) for the year 2000-2010. Figure (a) used with permission.

Burgess & Smith (2002) provide a dataset of permafrost depth observations for Canada based on temperature readings. The Burgess & Smith (2002) dataset is a compilation of borehole data across Canada ranging in observation date from 1966 to 1990. Permafrost depth in the observational dataset was determined based on the bottom boundary identified by the temperature gradient to be below 0 °C; thus, each borehole has a single observed value. The data can be accessed from the Government of Canada GEOSCAN database (Burgess & Smith, 2002).

When comparing the simulated permafrost depth and the observed permafrost depth (Figure 3.5) it is important to recall that the soil and bedrock depth of the UVic ESCM is limited to 250 m and the vertical resolution of the model is coarse at deeper soil layers. For the purpose of comparison, the scale for permafrost depth (Figure 3.5) is limited to 250 m, despite the fact that many permafrost observations exceed this depth. Moreover, because the observational data was collected using boreholes, it was only possible to compare the simulation to a snapshot in time, rather than an average. Figure 3.5 suggests that the simulated permafrost distribution in North America broadly agrees with the observed distribution (Burgess & Smith, 2002). Similarly, the correlation plot (Figure 3.6) limits the dataset to permafrost shallower than 250 m. Due to the limited number of observations of permafrost above 250 m and the spatial heterogeneity of permafrost depth and variables that would impact permafrost depth such as snow cover and vegetation, it is difficult to compare these limited observations to the model results. Work by Avis (2012) found that an increase in vertical resolution of the ground in the model greatly improved the representation of permafrost depth, but that despite this increase in vertical resolution, the permafrost area remained similar.

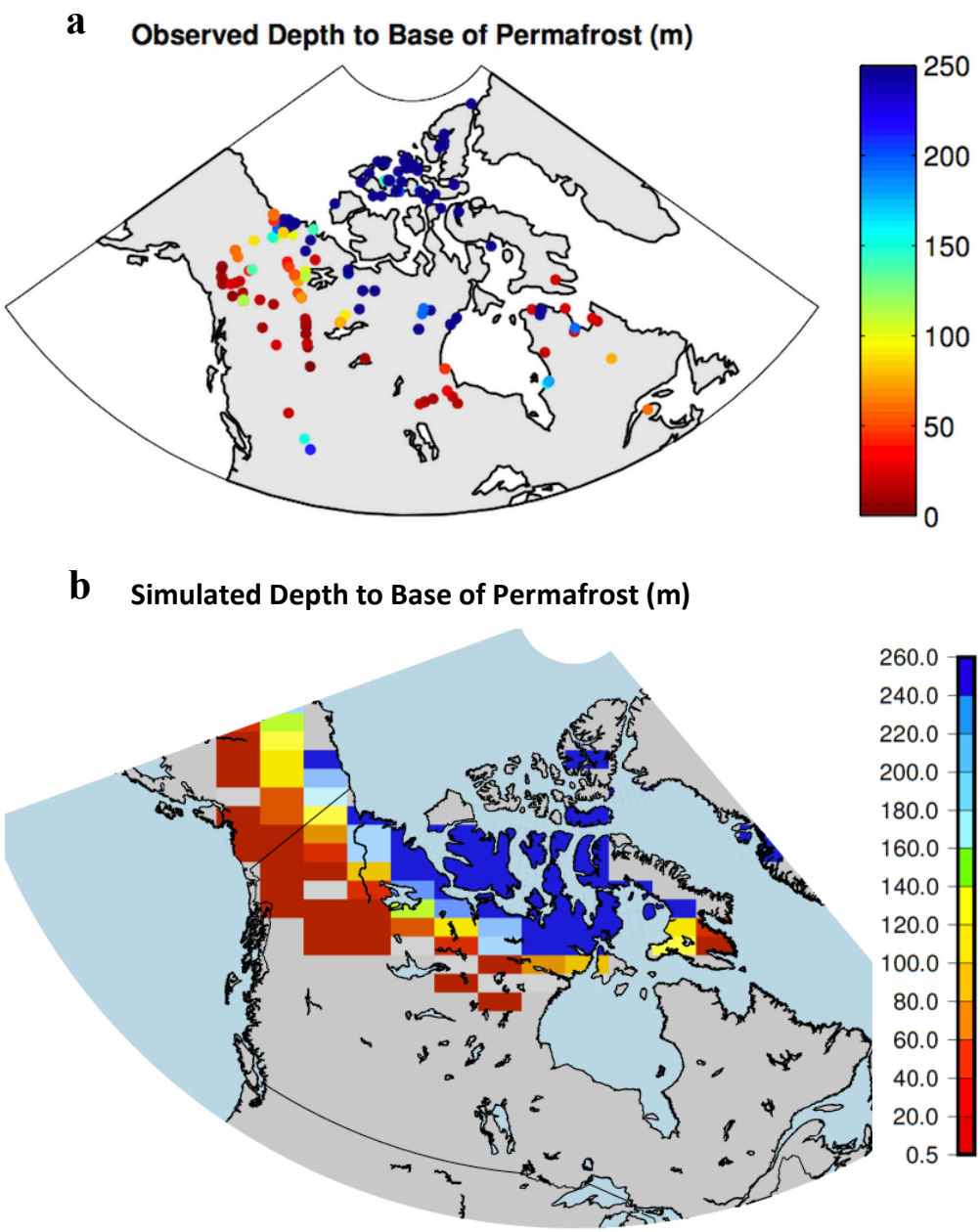

Figure 3.5: (a) Observed depth of permafrost for the region of Northern Canada (data source: Smith & Burgess, 2002, figure source: Avis (2012)), the colour bar has been restricted to 250 m depth to aid in comparison to the UVic ESCM (Avis, 2012) (b) Simulated annual mean permafrost depth for years 1966-1990. Figure (a) used with permission.

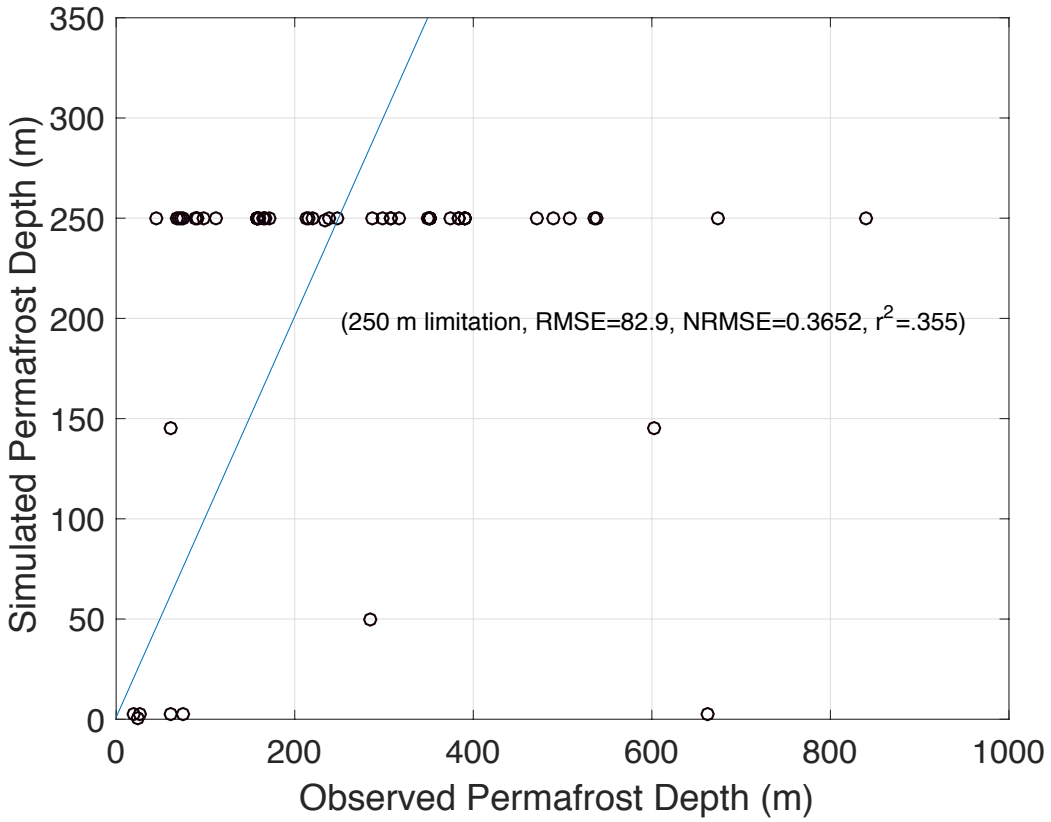

Figure 3.6: Scatter plot comparing observed borehole permafrost depth (Smith & Burgess, 2002) to permafrost depth simulated by the UVic ESCM. The ground depth in the UVic ESCM is limited to a depth of 250 m, so the statistical analysis includes only observed permafrost depths above 250 m. The blue line represents a 1:1 relationship. Root Mean Square Error (RMSE), Normalized Root Mean Square Error (NRMSE) and root squared (r^2) are only calculated for data points with depths above 250 m.

3.1.4. Ground Surface and Subsurface Temperature

Figure 3.7 shows ground surface temperature, defined as the temperature at the intersection of the atmosphere and the surface. To determine the mean annual ground surface temperature, soil temperature sites of Environment Canada were used (as reported in Smith & Burgess, 2000). These sites were located on level ground, exposed to the elements year-round, and in the summer on grass that was maintained. Because of the maintenance of the vegetation on these sites, they are considered to be artificial

(Smith & Burgess, 2000). Ground surface data were accessed from the Government of Canada GEOSCAN database (Smith & Burgess, 2000).

The UVic ESCM values used for comparison to the estimated ground surface data are the temperature at the surface of the uppermost ground layer. This layer is also known as skin temperature, hereafter referred to as ground surface temperature; this is the layer that interacts with the atmosphere.

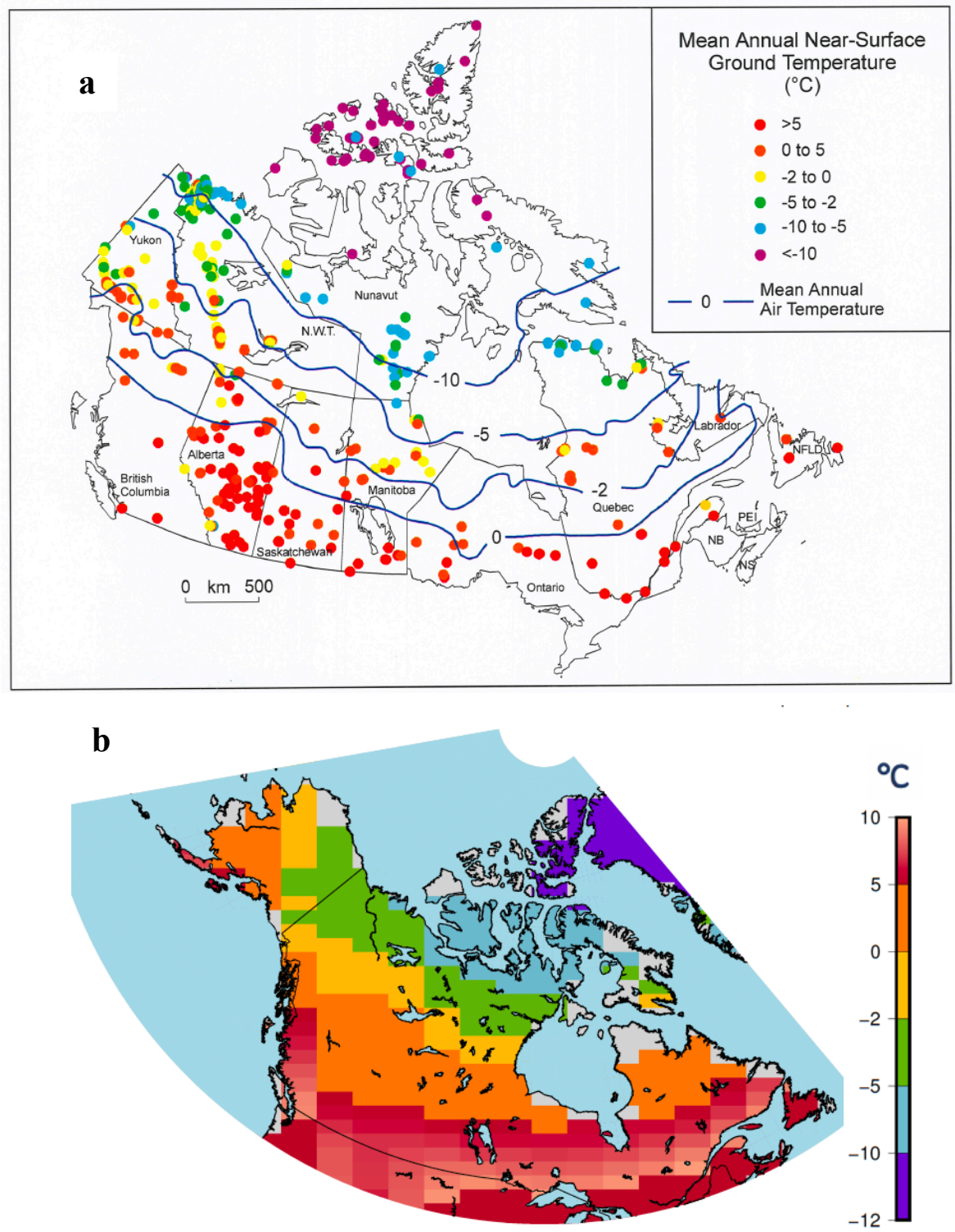

Figure 3.7: (a) Ground surface temperature based on station data from Environment Canada over the period 1951-1980, (Burgess & Smith, 2000) and (b) simulated ground surface temperature averaged over the period 1951-1980.

As shown in Figure 3.7, the model is able to simulate the broad spatial pattern of ground surface temperature evident in observations, with ground surface temperature decreasing poleward. Upon closer examination, a systemic cold bias in the model is evident in the surface ground temperature (Figure 3.7). Particular locations where a cold bias is evident are northern Yukon where the observed values range from 0 °C to -5 °C but are simulated between -2 °C and -5 °C; southern Yukon, where the observed values range from 0 °C to over 5 °C, but are simulated between -2 °C and 5 °C; and in southern Canada where observed values are typically over 5 °C but are simulated between 0 °C and 10 °C. The cold model bias could be the result of the Smith and Burgess (2000) dataset being acquired from stations that have no vegetation cover and are therefore directly exposed to sunlight. As a result, in the summer months the temperatures at these stations would be higher than would be expected to occur naturally due to the absence of vegetation cover. The cold bias in the model could also be due to the way snow is represented in the land surface scheme of the UVic ESCM. Snow cover is an extension of the land surface scheme and, as a result, lower surface temperatures are simulated at 0 m depth in the winter because the model is evaluating from the top of the snow surface and not the top of the ground. In summary, the UVic ESCM is influenced by air temperature in the winter and therefore not acknowledging the effect of snow insulation at the right depth, while the observed temperatures represent exposed ground and therefore are too warm during the summer months.

To further investigate the temperature distribution with depth in the UVic ESCM, subsurface ground temperatures were analysed. Observations of subsurface ground temperature with depth were accessed from the National Snow and Ice Data Center ("Circum-Arctic Map of Permafrost and Ground-Ice Conditions, Version 2 | National Snow and Ice Data Center," 2019) and are a collaboration from the International Polar Year with circumpolar data ranging from 1980 to 2009, but primarily observed between 2007 and 2008. This dataset provides single measurements for a variety of depths.

Figure 3.8 shows that observed temperatures in the range of 0 °C to -3 °C are simulated by the UVic ESCM between -4 °C and -6 °C. Observed temperatures below -4 °C are simulated well, as are those between -2 °C and 2 °C (Figure 3.7). In comparison, there is a cluster at -5 °C (simulated values) where the model simulates temperature too cold. All of the observations for permafrost depth, active layer thickness and permafrost depth are single measurements and therefore specific to a time of year, while the UVic ESCM is providing an average for either a specific year or, in the case of permafrost depth, a span of years. As a result, there will be some discrepancies between the observed and simulated values due to the fact that ground temperature takes times to equilibrate to changes in surface temperature (with the amount of time increasing with depth). Nevertheless, these comparisons are still useful in providing an overall sense of how the UVic ESCM simulates these variables.

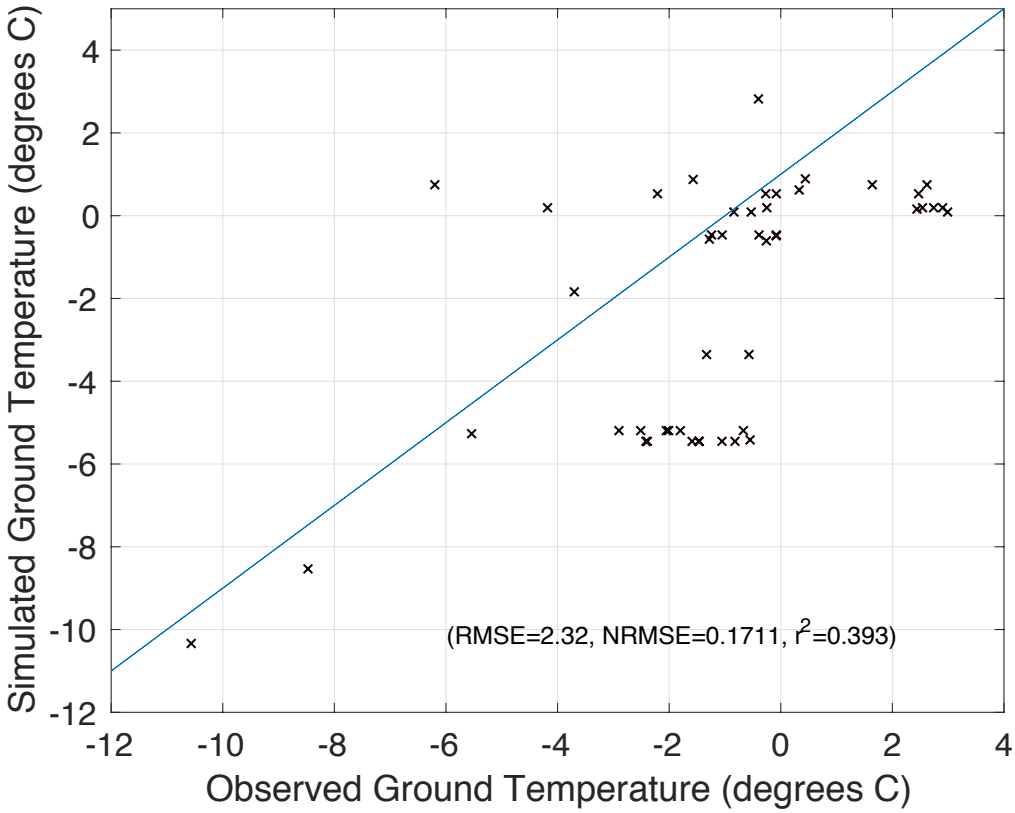

Figure 3.8: Scatter plot comparing observed ground temperature to simulated ground temperature at depths between 5-25 m. Borehole data ("Circum-Arctic Map of Permafrost and Ground-Ice Conditions, Version 2 | National Snow and Ice Data Center," 2019) taken between the years 1980-2009. Blue line represents a 1:1 relationship.

Subsurface temperature logging is one of the most widely used methods of determining temperature at depth, and thus, the presence of an active layer and permafrost. This method essentially involves lowering a thermometer down a borehole to obtain a temperature log or inserting it into the near surface materials to measure ground temperature, in some cases over a prolonged period of time. Recent literature suggests that temperature logging through the active layer can lead to an underestimation of the permafrost extent due to surface subsidence as a result of thawing ice due to increased temperatures (Streletskiy et al., 2017). Nevertheless, temperature logging remains one of the most accurate ways to measure subsurface temperature (*Snow, Water, Ice and Permafrost in the Arctic (SWIPA) 2017*).

Comparison of subsurface ground temperature profiles with observation data for northern Canada:

In the following, ground temperature profiles simulated by the UVic ESCM are compared with observational data for northern Canada derived from boreholes. This dataset is The Canadian Geoscience Data Collection (CGDC) ("Canada - Geoscience Data" 2019). Due to the coarse resolution of the UVic ESCM grid, multiple borehole sites exist within a single UVic ESCM grid cell. In Figure 3.10, boreholes are represented by B1-B5 and are compared to the UVic ESCM model simulation for the corresponding grid cell encompassing those locations. Multiple borehole locations were used within a single UVic ESCM grid cell as subsurface temperature varies considerably from one location to another within the same grid cell.

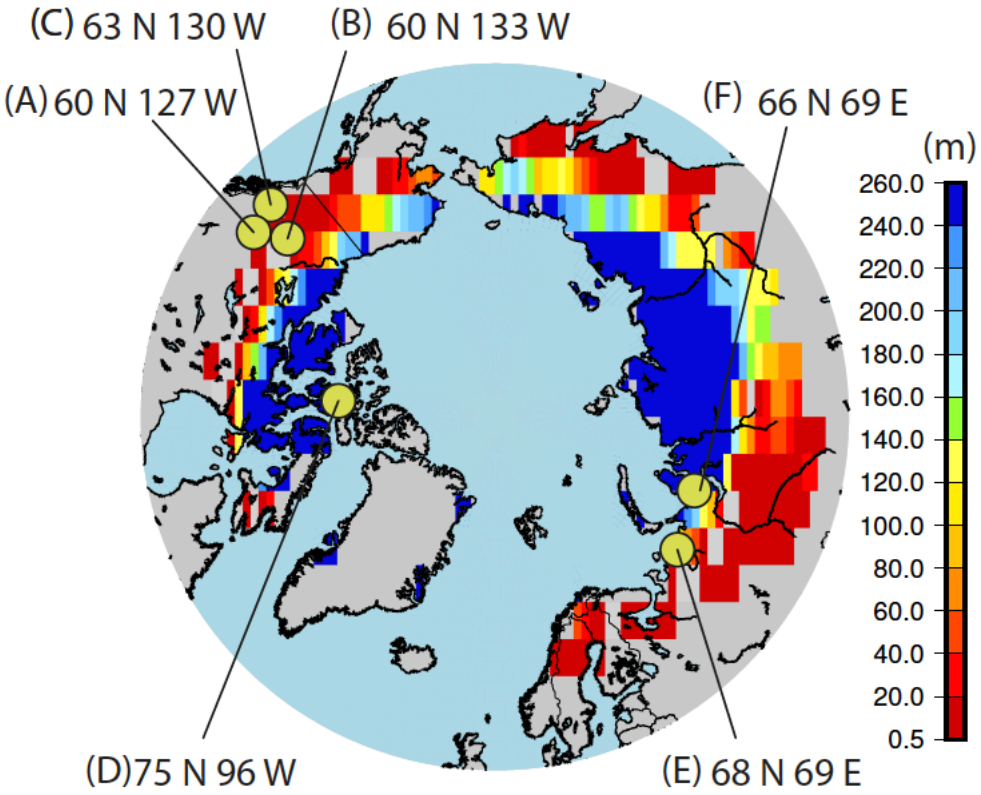

Figure 3.9: Simulated circumpolar permafrost depth for the year 2016. Green circles show the locations of subsurface ground temperature profiles from borehole data shown in Figures 3.10 and 3.11. The coordinate location represents the location of the boreholes used for comparison.

When UVic ESCM simulation results are compared to the observed ground temperature data (Figure 3.10), it is apparent that the UVic ESCM model ground temperature profiles are within the range of observed borehole data, with the exception of the location 63N, 130W (Figure 3.7c) where the UVic ESCM simulation is consistently too cold by approximately 1 °C. Figure 3.10a, b and c indicated that the temperature gradients simulated by the UVic ESCM are comparable to the observed gradients. For example, the slope of the UVic profile in Figure 3.10a is -49.7 m/°C and the average gradient of the observed profiles is -39.8 m/°C.

The negative kink seen in the simulated ground temperature profiles is caused by snow cover being considered an extension of the land surface scheme in the UVic ESCM as previously discussed in this section. This means that the UVic ESCM is interpreting the top of the snow surface as the top of the ground layer, so what is being represented as the ground surface temperature in the winter months is not the surface of the ground which would be insulated due to snow cover but the surface of the snow layer that is interacting directly with the atmosphere.

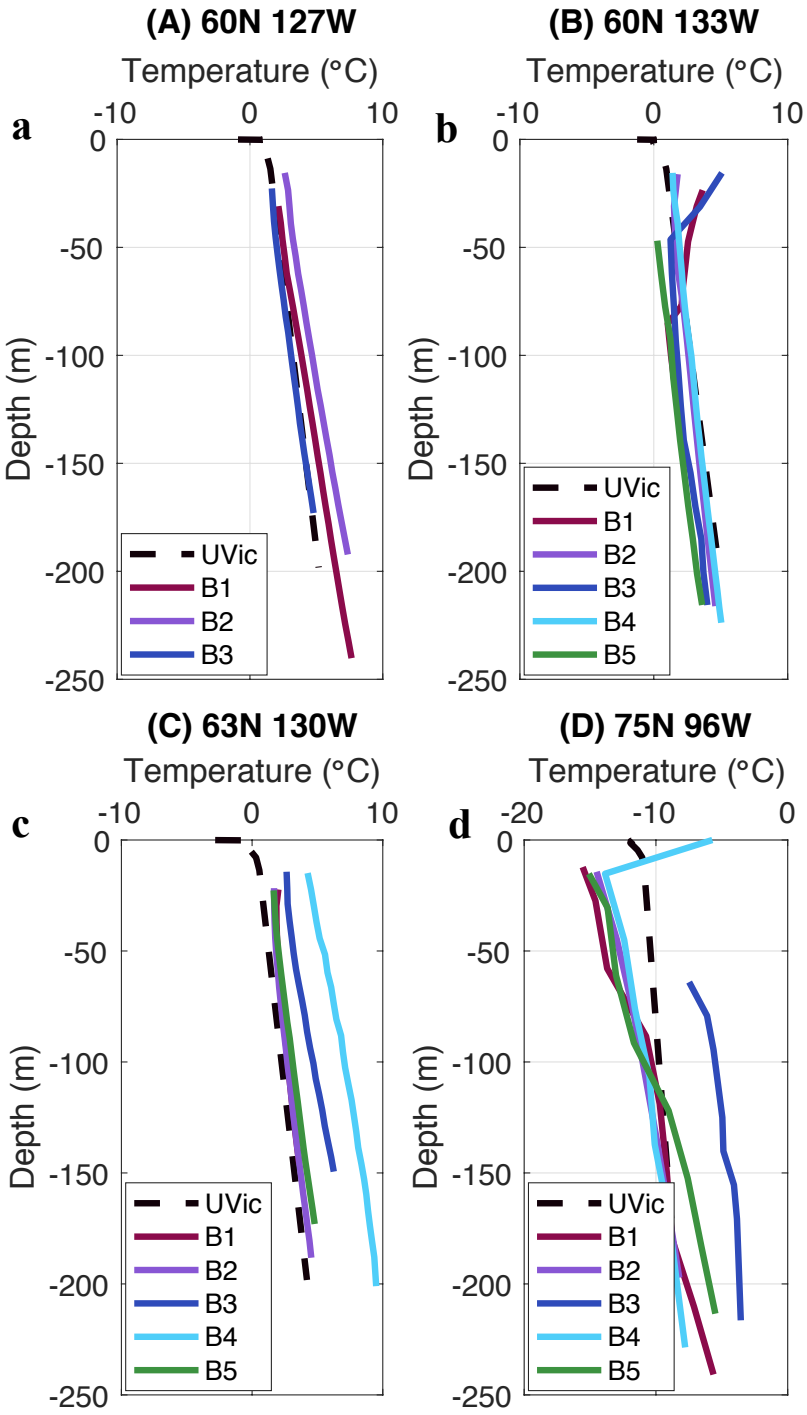

Figure 3.10: Ground temperature profiles for multiple Canadian Geoscience Data Collection (CGDC) boreholes for the year 1980. Boreholes are labeled B1, B2, etc. and represent specific borehole observations (see Figure 3.9 for the location of the boreholes in panels a through d), while UVic represents the model output averaged over the corresponding grid cell.

Comparison of soil temperature profiles with observation data for northern Russia:

This section compares simulated UVic ESCM sub-surface ground temperatures with a Russian ground temperature dataset provided by the Global Terrestrial Network for Permafrost (GTN-P) (Global Terrestrial Network for Permafrost (GTN-P), 2019). Compared to the work of the CGDC, the dataset for Russia is more limited in terms of the number of boreholes available within a single grid cell, and the depth of the boreholes, which extend to only 10 m. Nevertheless, this dataset provides a comparison of shallow subsurface ground temperature that the Canadian dataset (Burgess & Smith, 2002) does not.

Due to the lack of locations with multiple boreholes within a single UVic grid cell, it is challenging to draw a conclusion as to the accuracy of the UVic ESCM in simulating subsurface ground temperature profiles in northern Russia. As shown in Figure 3.8, the subsurface ground temperatures simulated by the UVic ESCM at mid Arctic latitudes in Russia are too cold by approximately 1 °C to 6 °C. This cold model bias in these locations is consistent with what was found in the near surface air temperature bias (Figure 3.1). The regions with a cold bias of between 1 °C to 6 °C in the ground temperature profiles correspond to locations that have a cold bias of -2.5 °C to 5 °C near surface air temperature. As seen in the comparison for northern Canada, the temperature gradients simulated by the UVic ESCM and from borehole observations in Russia for locations e (Figure 3.11 panel a) are quite similar, -10.48 m/°C and -14.06 m/°C, respectively.

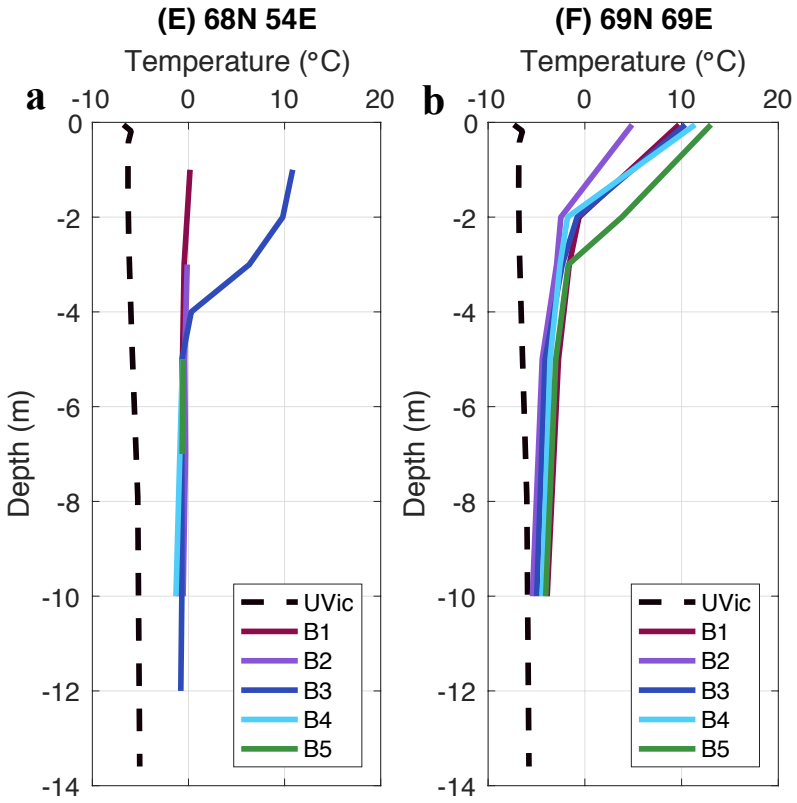

Figure 3.11: Subsurface ground temperature profiles for multiple boreholes in northern Russia (see borehole locations Figure 3.9) for the year 2016. Boreholes are labeled B1, B2, etc. and represent specific boreholes observations. UVic represents the model output averaged over the corresponding grid cell.

3.2. Projected changes in northern permafrost

This section discusses the effects of temperature change on permafrost under different types of scenarios (Shared Socio-Economic Pathways (SSPs)) as discussed in section 2.2.3. The scenarios can be classified generally as either stabilization (e.g. SSP4-6.0) or overshoot scenarios (e.g. SSP5-3.4-OS). Overshoot scenarios are scenarios in which the surface air temperature peaks and then declines and can be further classified as having a high or low overshoot with respect to a stabilization temperature. Table 3.2 gives an overview of scenarios used in this study and describes the scenario type, peak change in surface air temperature, the global mean surface air temperature at which the scenario stabilizes, and the type of permafrost response associated with it. In

general, permafrost area in all scenarios declines with increasing surface air temperature. Furthermore, high temperature stabilization scenarios result in a continued decline in permafrost area while overshoot scenarios result in a partial reversal of permafrost thaw (Figure 3.12).

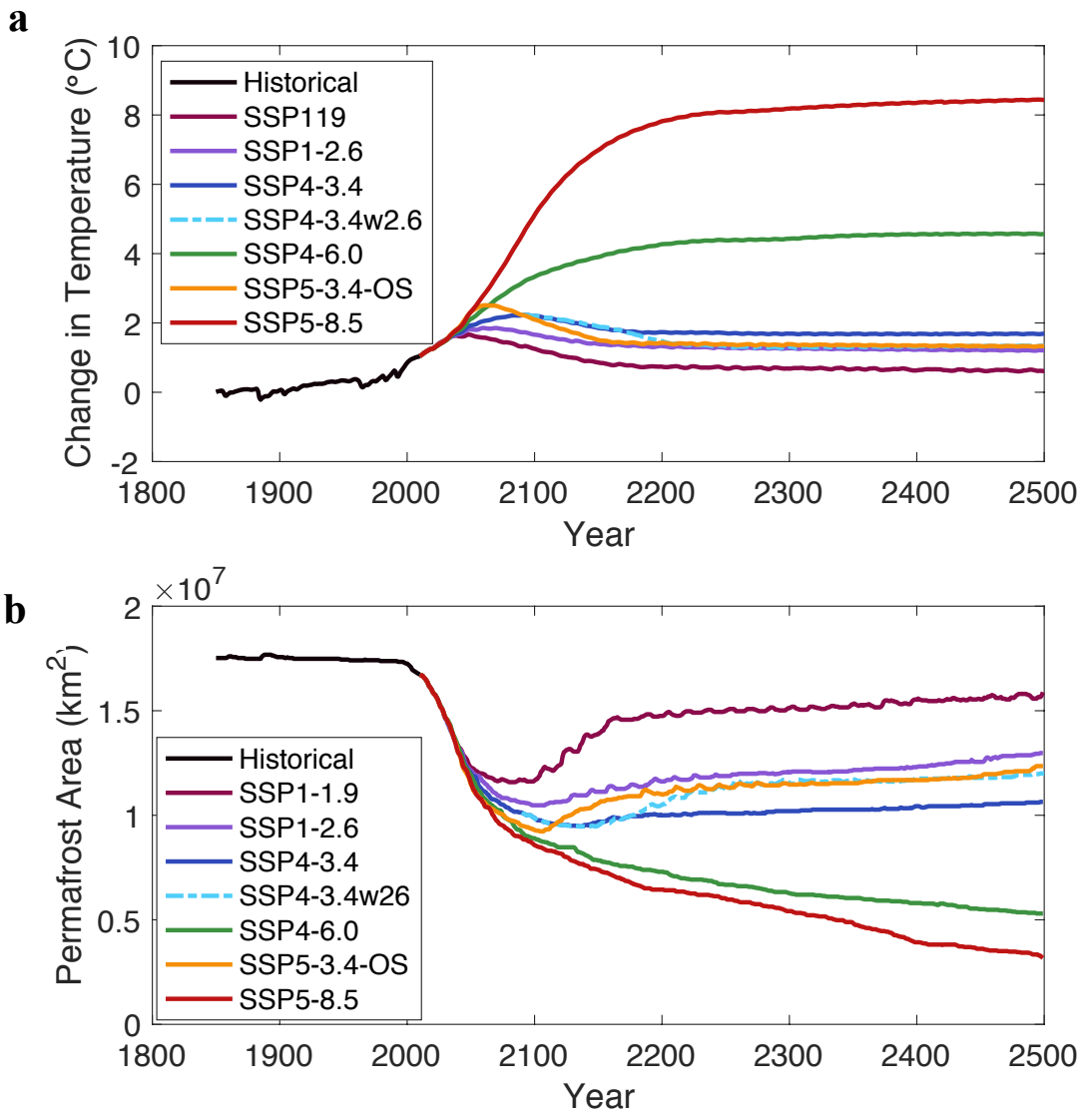

Figure 3.12: (a) Change in global mean surface air temperature relative to pre-industrial (1850-1900) for each Shared Socio-Economic Pathway (SSP) and (b) the resulting changes in northern permafrost area with time.

Table 3.2: Scenario descriptions. From left to right the type of scenario (Overshoot (OS) or stabilization (ST), continued warming (CW)), the peak change in surface air temperature (°C) relative to pre-industrial (1850-1900), the change in surface air temperature at which the scenario stabilizes (°C) relative to pre-industrial, the year of stabilization, and the permafrost (PF) response type.

Scenario	Type	Peak ΔT (°C)	Stabilization ΔT (°C) and year	PF Response
SSP1-1.9	Low OS	1.66	0.73, 2200	Partial reversal
SSP1-2.6	Low OS	1.84	1.33, 2200	Partial reversal
SSP4-3.4	High OS	2.23	1.42, 2200	Partial reversal
SSP4-3.4w2.6	High OS	2.23	1.42, 2210	Partial reversal
SSP4-6.0	ST	4.56	4.30, 2210	Decline
SSP-8.5	CW	8.44	n/a	Decline

The remainder of this chapter discusses the effects of different scenarios on permafrost area in more detail. Section 3.2.1 shows the effects on permafrost at different levels of warming if there is no time allowed for the subsurface to reach equilibrium. The effect of temperature overshoot scenarios on permafrost reversibility is discussed in Section 3.2.2, and the commitment to permafrost thaw due to high temperature stabilization scenarios is discussed in Section 3.2.3.

3.2.1. Influence of different temperatures on permafrost extent

To determine the effect of different surface air temperature levels on permafrost thickness and permafrost extent, the high emissions scenario, SSP5-8.5, is used to compare the permafrost area at different levels of global mean surface air warming relative to pre-industrial. As expected, with an increase in global mean surface air temperature there is a decline in both permafrost extent and thickness (Figure 3.13). As surface air temperature increases, relative to pre-industrial values, permafrost in the northern hemisphere is projected to decrease by 2.88 x 10^6 km^2 (16.4 %) with a change of 1.5 °C, 5.22 x 10^6 km^2 (29.7 %) with a change of 2 °C, 6.60 x 10^6 km^2 (37.9 %) with a change of 2.5 °C and 7.25 x 10^6 km^2 (41.3 %) with a change of 3 °C.

With a change of 1.5 °C, permafrost near 60 °N in Russia begins to thin and as temperature rises to a 2 °C change, permafrost ceases to exist south of 60 °N in Russia (Figure 3.13). Furthermore, in the transition from 1.5 °C to 2 °C, permafrost south of 66 °N in Canada and Alaska begins to thin or disappear completely. The permafrost lost as a response to an increase in surface air temperature from a 1.5 °C to 2 °C is 2.40 x 10^6 km^2 (16.8 %), relative to the area existing at 1.5 °C. After a change of 2 °C, permafrost is less than 5 m thick in Sweden, Norway and Finland, and in north eastern Russia it almost completely thaws (Figure 3.13). With an increase of 2.5 °C and 3 °C the permafrost begins to thin on the southern permafrost boundary in northern Canada and north central Russia. These 0.5 °C surface air temperature changes from 2 °C to 2.5 °C and 2.5 °C to 3 °C cause a loss of 1.22 x 10^6 km^2 (9.8 %) and 6.40 x 10^6 km^2 (5.8 %) permafrost area, respectively. Therefore, permafrost sees the greatest loss per 0.5 °C surface air temperature from 1.5 °C to 2 °C and the greatest overall loss of permafrost area at a surface air temperature change of 3 °C (Figure 3.13). The slope of the SSP5-8.5 curve in Figure 3.14 illustrates this loss per 0.5 °C well, the steeper the slope, the more permafrost lost per degree of warming. Model simulations show that at a change of 3°C, only locations north of 60 °N in Russia and permafrost bordering or north of the Arctic Circle in North America are still present. Results indicate a thinning of permafrost as a result of increases in surface air temperature. However, due to the time required for heat to penetrate to greater depth in the soil, there is a lag in the response of permafrost to warming. This lag in permafrost response implies that the results shown in Figure 3.13 do not show the full extent of the change in permafrost resulting from a specific level of warming. To account for this temperature penetration lag, section 3.2.3 discusses the impact on permafrost area in the case of a temperature change that stabilizes over time. An increase in surface air temperature results in more immediate permafrost thaw near the ground surface (i.e. permafrost thaw from the top). Over the long term, the heat gained at the surface will propagate deeper into the subsurface, and eventually result in thaw at the base of the permafrost. As such, there is a time lag in the thawing of deep permafrost that is not represented in Figure 3.13. Instead, Figure

3.13 reflects permafrost that has been impacted closer to the surface because that is as far as the heat has travelled in the prescribed simulation time. The rate at which surface air warming penetrates into the subsurface is dependent on many factors, such as, the composition of the ground, vegetation cover, the moisture level and insulation due to snow (Barrere et al., 2018; Kholodov et al., 2016; Wang et al., 2019).

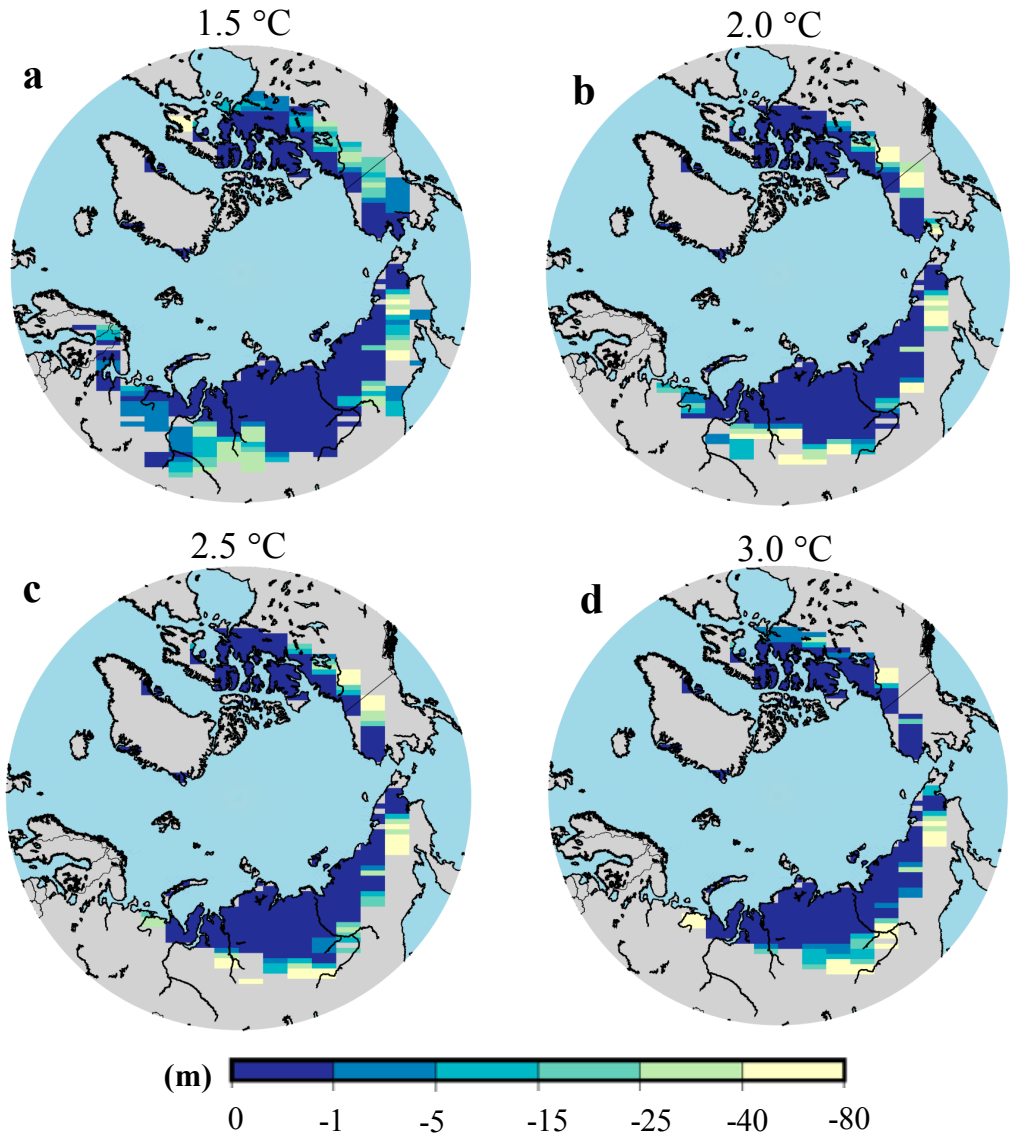

Figure 3.13: Change in permafrost thickness relative to pre-industrial for different levels of warming following SSP5-8.5. From top left to bottom right the levels of warming are a) 1.5 °C, b) 2 °C, c) 2.5 °C and d) 3 °C relative to the pre-industrial period (1850-1900). More negative values indicate a greater loss of permafrost is projected in the future. Grey areas indicate areas without permafrost.

3.2.2. Impact of temperature overshoot

This section focuses on overshoot scenarios and the effects that this type of scenario has on permafrost thickness and area. The examined overshoot scenarios include SSP1-2.6, which is here classified as a low overshoot scenario, and SSP4-3.4w26 and SSP5-3.4-OS, which are here classified as high overshoot scenarios. The scenarios differ in their magnitude and duration of overshoot. Table 3.2 describes changes in peak surface air temperature and the year in which temperature peaks and the duration of each of these overshoots is also slightly different. Figure 3.12 suggests that for all overshoot scenarios, permafrost area increases as a result of decreasing global mean surface air temperature. Although permafrost area is shown to recover, permafrost recovery lags the decrease in surface air temperature (Figure 3.14). The amount of time required for permafrost to recover depends on the scenario, as the peak temperature and duration of the overshoot are different. The required time before permafrost starts to recover following a decrease in temperature ranges from 30-50 years (Table 3.3).

Table 3.3: Lag time and permafrost (PF) loss for overshoot scenarios by 2200 relative to the same temperature prior to the overshoot. Lag time is defined as the amount of time between when surface air temperature begins to decrease and permafrost recovery begins.

Scenario	Lag time for PF to begin to recover (years)	PF area loss (%)
SSP1-1.9	40	15.5
SSP1-2.6	40	27.8
SSP4-3.4w2.6	50	22.6
SSP4-3.4	50	28.9
SSP5-3.4	30	28

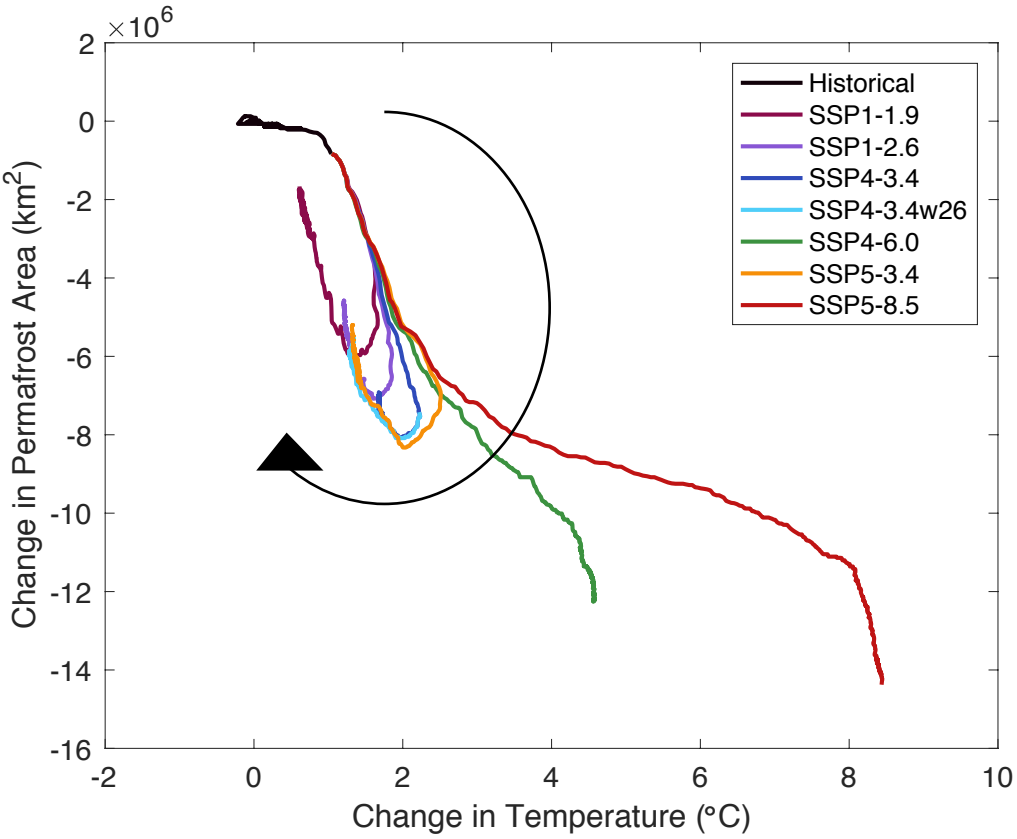

Figure 3.14: Change in permafrost area as a function of change in surface air temperature for all scenarios to the year 2500 realtive to the pre-industrial period (1850-1900). The arrow illustrates the direction in which the trajectories are followed.

To further investigate the effect of surface air temperature overshoot on permafrost extent the differences between permafrost area were explored between two high overshoot scenarios, SSP5-3.4-OS and SSP4-3.4w26, and the low overshoot scenario SSP1-2.6. Relative to the low overshoot scenario SSP1-2.6, the difference in peak warming for overshoot scenarios SSP4-3.4w26 and SSP5-3.4-OS are 0.38 °C and 0.65 °C, respectively (Table 3.2). Surface air temperature in SSP5-3.4-OS and SSP4-3.4w2.6 converges with that in SSP1-2.6 in years 2170 and 2210, respectively, from which point on surface air temperature in the three scenarios remains similar. At the time that SSP1-2.6, SSP4-3.4w26 and SSP5-3.4-OS reach a similar temperature (year 2170 and 2210) the difference in permafrost extent relative to SSP1-2.6 is - 4.7 % and -7.9 % for SSP5-3.4-OS and SSP4-3.4w2.6, respectively (Figure 3.12).

The largest difference in permafrost extent in SSP5-3.4-OS and SSP4-3.4w2.6 relative to SSP1-2.6 at the time that surface air temperature in the scenarios converges (2170 and 2210, respectively) occurs at the southern border of the permafrost region (Figure 3.15a, b). This difference in permafrost extent indicates that the peak temperature of the overshoot impacts the amount of permafrost lost. Between the years 2200 and 2500, the difference in surface air temperature between SSP5-3.4-OS/SSP4-3.4w26 and SSP1-2.6 increases slightly (roughly 0.1 °C). While the slight temperature difference does somewhat limit the comparison over time, a difference in permafrost area and depth of up to 20 m in some locations is observed in the high overshoot scenarios relative to SSP1-2.6 in the year 2500. Permafrost extent in the year 2500 also differs between the high overshoot scenarios, despite a very small surface air temperature difference (0.01 °C). SSP5-3.4-OS, which has a larger but shorter overshoot than SSP4-3.4w2.6, has 3.5 x 10^5 km^2 more permafrost than SSP4-3w2.6 in the year 2500. This indicates that the duration of the overshoot has a larger impact on permafrost area than the magnitude of the overshoot.

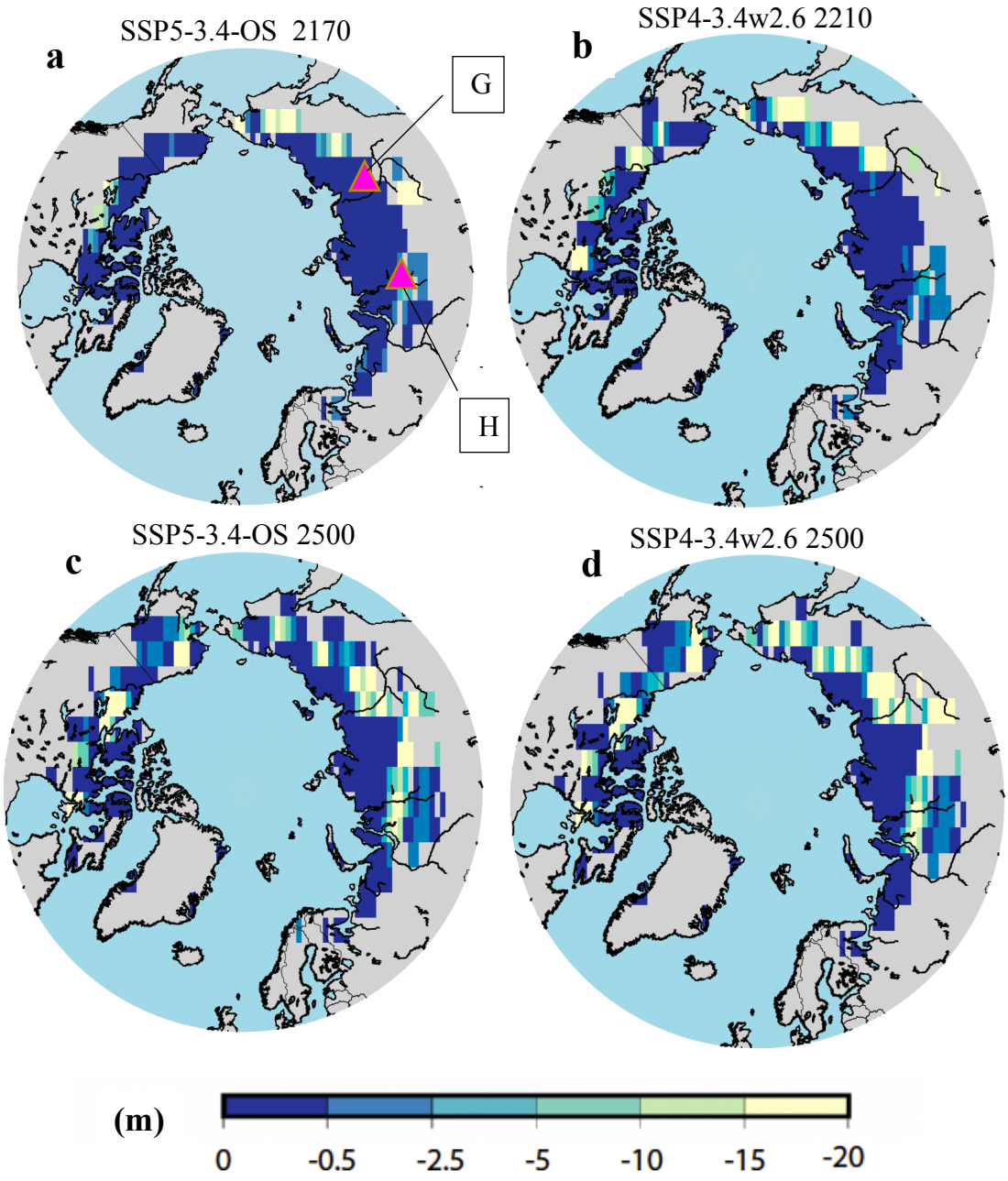

Figure 3.15: Difference in permafrost thickness under scenarios SSP5-3.4-OS (left) and SSP4-3.4w2.6 (right) relative to SSP1-2.6 for the year temperature converges, either 2170 or 2210 (top), and 2500 (bottom). Majeta triangles in panel (a) are the locations of ground profiles in Figure 3.16.

To better understand the effect of temperature overshoot on permafrost, it is useful to look at what is occurring in the subsurface at different points in time. Figure 3.16 shows the ground temperature profiles comparing SSP4-3.4w2.6 (panels a and b) and SSP5-3.4-OS to SSP1-2.6 (panels c and d) for different years for locations G and H in Figure 3.15. The profiles show that ground temperature recovery at depth lags the reversal in near surface air temperature. This is visible in the groud temperature profiles by looking at the difference between the 2170 (green) or 2200 (orange) line and the 2500 (red) line. Near the surface, the temperature profiles overlap but as the profile goes deeper the temperatures are no longer the same. This effect is due to the time required for heat to penetrate to depth. Figure 3.16 panels a and b show the difference in ground temperature profiles between SSP4-3.4w2.6 (dashed line) and SSP1-2.6 (solid line) for different years and two different locations. For the year 2200, the difference in subsurface temperatures is illustrated by the dashed and solid orange lines most clearly visible below 25 m. In the year 2200 the high overshoot scenario, SSP5-3.4-OS (dashed line) has a warmer temperature below a depth of 25 m than the referennce scenario SSP1-2.6 (solid line). This gap between the scenarios is representative of the impact of the overshoot. In the 2500 profile (red), the previous temperature gap between the scenarios has nearly closed, indicating that the warming that persisted at depthas a result of the overshoot has moved through the soil column, and by the year 2500 the two scenarios have similar subsurface ground temperature. Figure 3.16 panel c and d show the differences in ground temperature profiles between SSP4-3.4-OS and SSP1-2.6. SSP1-2.6 is consistently cooler than SSP5-3.4-OS below 25 m despite global surface air temperature in 2170 being similar. The evolution of the ground temperature in SSP5-3.4-OS is similar to SSP4-3.4w2.6 following the overshoot.

The cause of different permafrost thickness over time as seen in Figure 3.15 can be understood by looking at Figure 3.16 and the difference in ground temperature profiles between the solid lines (SSP1-2.6) and the dashed lines (SSP4-3.4w2.6 or SSP5-3.4-OS). The scenarios with higher overshoot (SSP5-3.4-OS and SSP4-3.4w2.6) relative to the low overshoot scenario SSP1-2.6 have consistently wamer subsurface temperatures between the years 2200 and 2500.

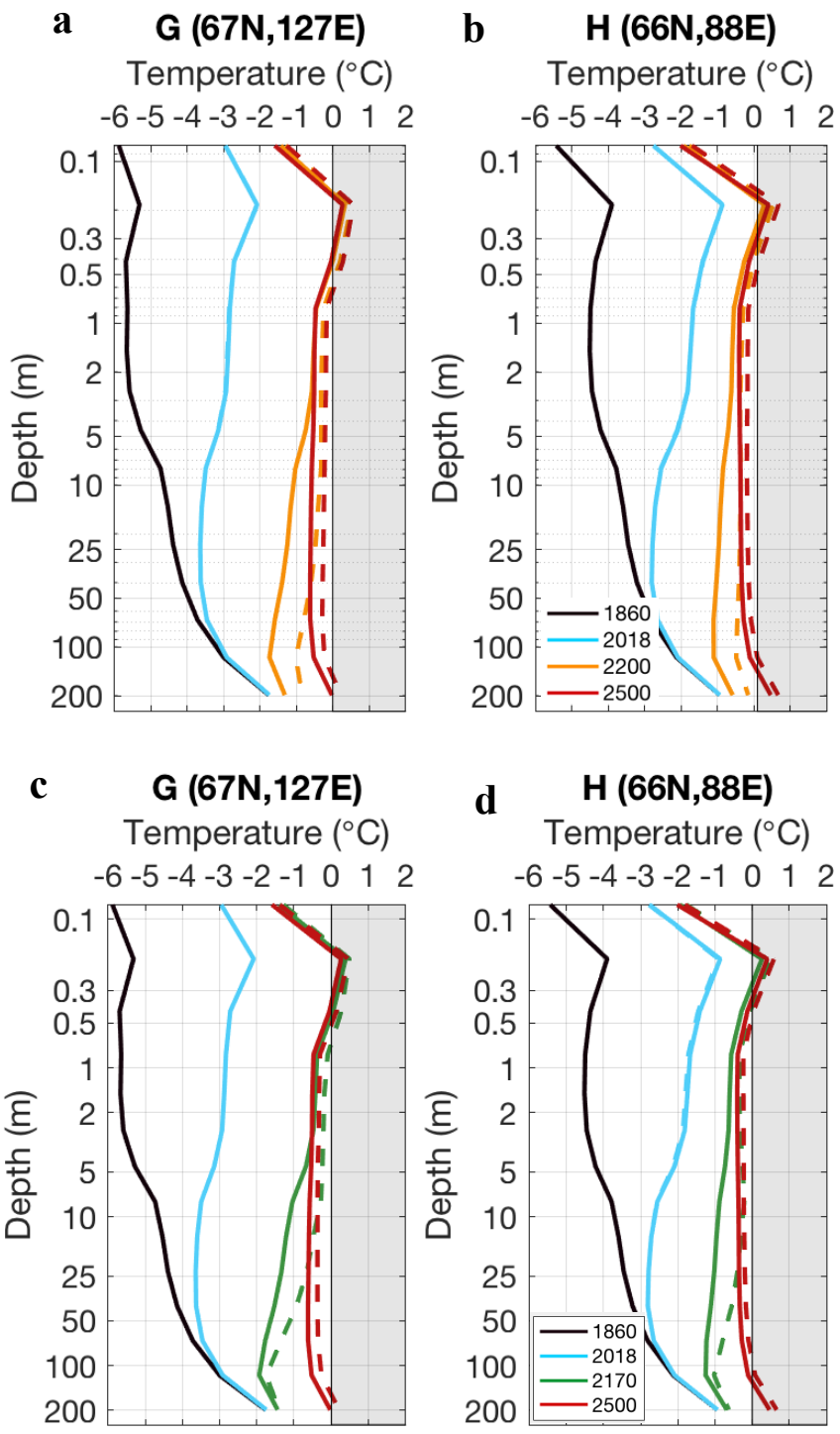

Figure 3.16: Subsurface temperature profiles for scenarios SSP4-3.4w2.6 (dashed line, panels a and b), SSP5-3.4-OS (dashed line panels c and d) and SSP1-2.6 (solid line, all panels). The location of these plots are indicated on the top left map of Figure 3.15. Note that the scale is nonlinear and emphasizes the ground layer close to the surace. The grey area indicates temperatures above 0 °C.

3.2.3. Committed permafrost thaw

This section focuses on scenarios in which global mean surface air temperature stabilizes at specific levels (Figure 3.17).

The response of the permafrost to this type of temperature trajectory does not mirror temperature; instead of stabilizing, permafrost is projected to continue to thaw. This continuation of permafrost thaw despite temperature stabilization is referred to as "committed" permafrost thaw in this section. In stabilization scenarios such as SSP4-6.0 global mean surface air temperature remains relatively constant (Figure 3.17) but northern surface air temperatures continue to increase (Figure 3.18 panel a). Despite this stabilization in global mean air temperature, permafrost continues to decline between 6.6 % and 50.4 % depending on the scenario between 2200 and 2500. Scenarios with higher stabilization temperatures see a greater loss in permafrost area between the time of stabilization and 2500 than those that stabilize at lower temperatures, with the exception of SSP4-6.0. The temperature stabilization in SSP4-6.0 occurs over a longer period of time compared to the stabilization scenarios that branch from SSP5-8.5 scenarios and therefore is not found to match the trend. Relative to 2210 permafrost area, by the year 2500 SSP5-8.5-2deg loses 6.11×10^5 km^2 (6.6 %), SSP5-8.5-3deg loses 1.73×10^6 km^2 (22.8 %) and SSP4-6.0 loses 1.77×10^6 km^2 (25.1 %). Scenarios SSP5-8.5-6deg and SSP5-8.5 lose the greatest area, amounting to 2.75×10^6 km^2 (42.8 %) and 3.23×10^6 km^2 (50.4 %) respectively.

The difference in surface air temperature between the years 2210 and 2500 for SSP4-6.0 and the effects that this has on the permafrost thickness are shown in Figure 3.18. The largest changes in permafrost thickness (Figure 3.18 b) occur where surface air temperature continues to increase in the northern hemisphere (Figure 3.18 a). In the UVic ESCM, this difference ranges between 0.3 °C and 1.4 °C depending on the scenario and the point in time with the largest difference seen in SSP5-8.5 in the year 2189 of 1.35 °C. The difference in temperature for the majority of the scenarios is between 0.5 °C to 0.7 °C after 2010.

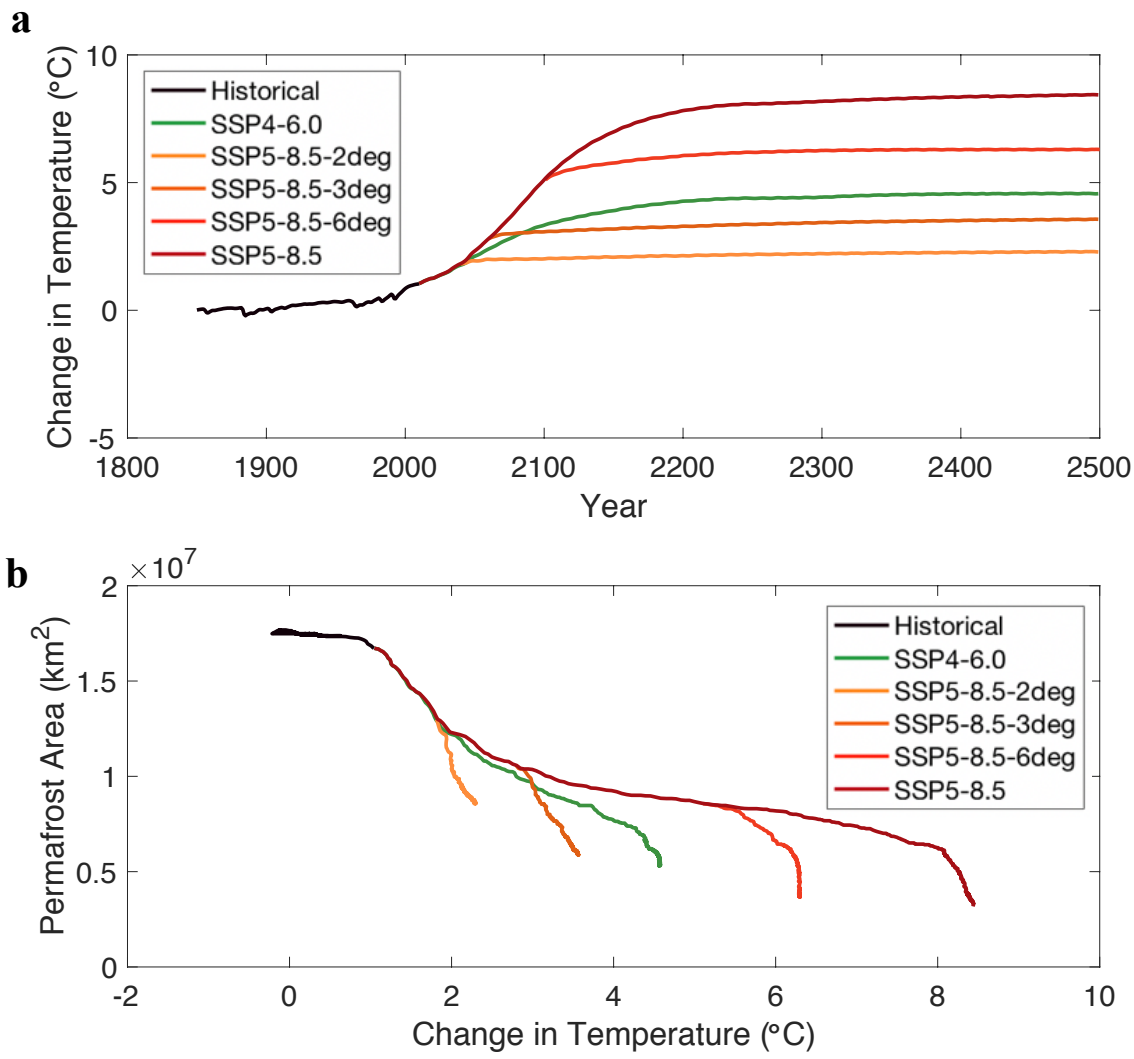

Figure 3.17: (a) Change in surface air temperature over time for stabilization scenarios. (b) Change in permafrost area with respect to change in surface air temperature for stabilization scnearios.

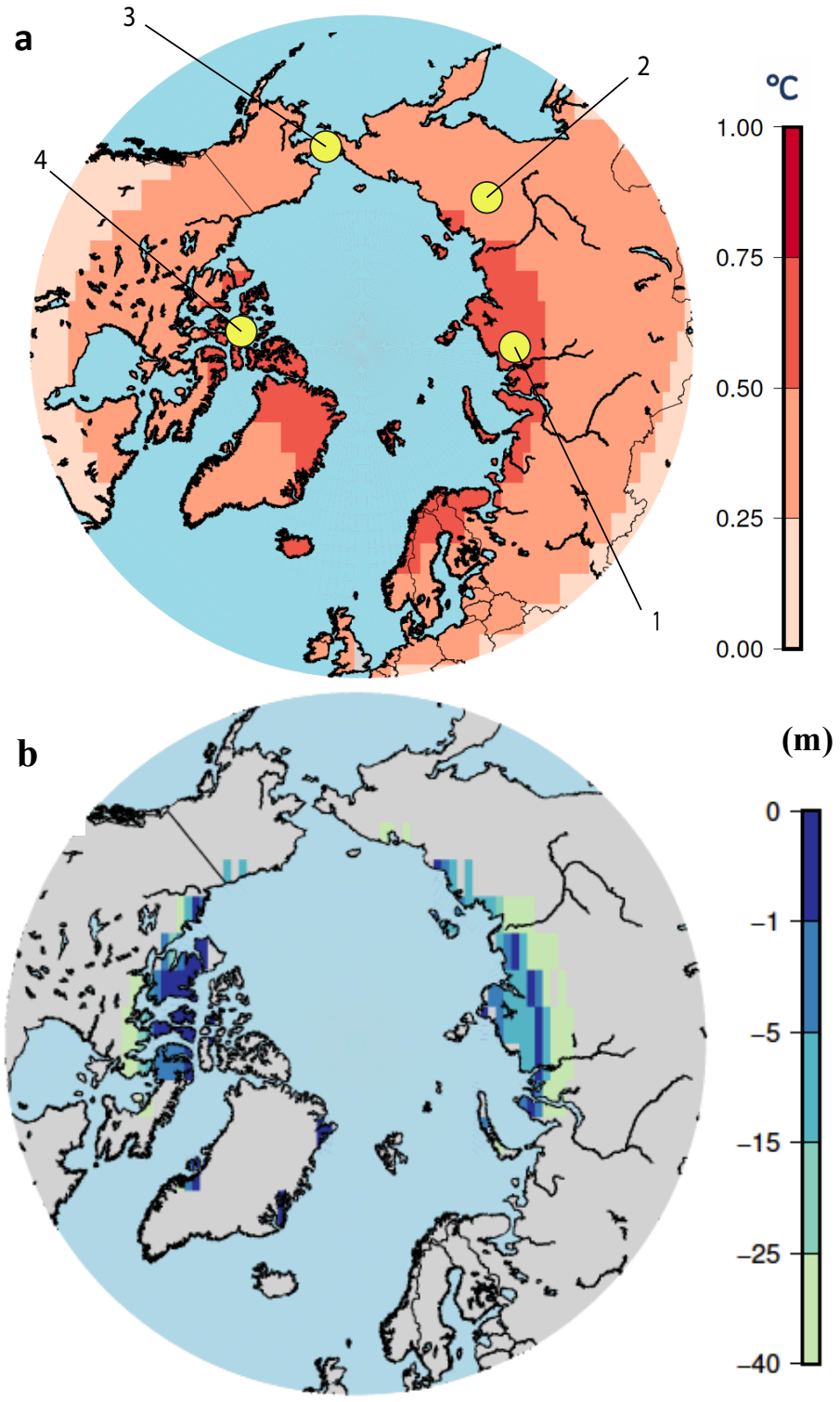

Figure 3.18: a) Difference in global mean surface air temperature between 2500 and 2210 for scenario SSP4-6.0. Yellow circles show the locations of profiles in Figure 3.19. (b) Difference in permafrost thickness between 2500 and 2210 for scenario SSP4-6.0.

When the global surface air temperature in SSP4-6.0 stabilizes, the permafrost area does not stabilize. This continued thaw differs from the permafrost response at lower temperatures following temperature overshoot (Figure 3.12). For example, in the overshoot scenarios SSP1-1.9, SSP1-2.6 or SSP4-3.4 after the year 2200 when they become stable, the permafrost area remains relatively stable or continues to increase with time. Ground temperature profiles for SSP4-6.0 provide insight as to how much time is required for temperature to penetrate through the full depth of the soil column (Figure 3.19). Comparison of the ground temperature profiles in year 2200 (orange line) and year 2500 (red line) indicates that temperature continues to increase particularly below 5 m with the exception of location 2 where temperature above roughly 7 m decreases between 2200 and 2500. The continued warming of deep ground layers is the cause of the continued permafrost thaw.

Figure 3.19, panels c and d show that the entire ground temperature profile is above 0 °C from 2100 to 2500. In panels b and c, as a result of ground temperatures remaining above 0 °C shortly after 2100 permafrost will be lost in those locations. This loss of permafrost is consistent with Figure 3.18 which shows there is no permafrost in those locations between 2200 and 2500. As shown in subsurface temperature profiles, it will require centuries for changes in surface air temperatures to reach deeper geologic layers. These ground temperature profiles further support the findings in that there is a lag time in permafrost response due to the time required for heat to penetrate to the full depth of permafrost. This illustration of temperature profiles for the years 1850-2500 shows that the global mean temperature threshold will vary for different locations.

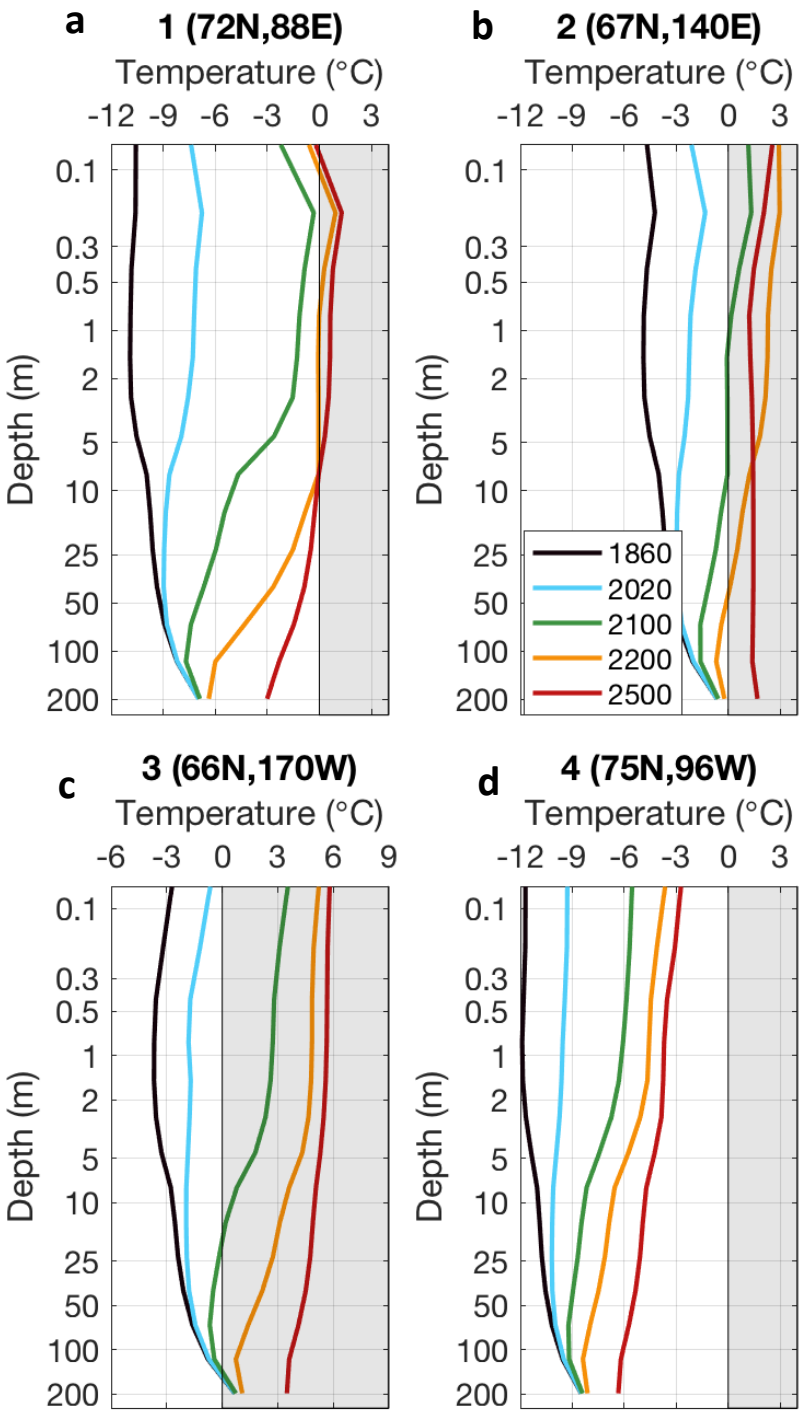

Figure 3.19: Subsurface temperature profiles for SSP4-6.0 at four different locations (1, 2, 3 and 4) as shown in Figure 3.18 panel a. Note that the scale is nonlinear and emphasizes the ground layer close to the surace. The grey area indicates temperatures at which permafrost would be absent.

Chapter 4. Discussion

Results show that the magnitude and the duration of a temperature overshoot in a given scenario directly influences the area of permafrost lost. The loss of permafrost area is between 15-30 % of permafrost area depending on the scenario relative to a similar temperature prior to the overshoot. The scenarios also show that permafrost recovery has a hysteresis effect, indicating an incomplete recovery of permafrost given similar temperature levels after the overshoot. The centennial time scale required for permafrost recovery is due to the rate at which heat penetrates into the ground. While overshoot scenarios showed a hysteresis effect for permafrost response, the high temperature stabilization scenarios, for example, SSP4-6.0, showed continued permafrost thaw after surface air temperatures stabilized.

Results provide evidence that under all scenarios, including those in which global mean temperature stabilizes, the northern high-latitudes continue to warm, and therefore, affect the soil temperatures at depth, causing further permafrost degradation. This is an important finding because it draws attention to the continued increase in surface air temperature in the northern high-latitudes compared to the approximately stable global mean temperature. Thus, while global mean temperature is a suitable indicator for global climate effects, my results suggest that especially for Arctic regions, the impact of this continued increase in surface air temperature should be considered. This finding suggests that any projection that uses global mean surface temperature as a primary indicator will underestimate the impacts at northern high latitudes.

Relative to the permafrost area in the year 2210, stabilization scenarios show there is a loss of permafrost area of between 6.6 % and 50.4 % by 2500. The amount of permafrost area lost varied depending on the scenario. In general, the higher the stabilization temperature, the more permafrost area lost over time. Due to the high surface air temperature associated with high stabilization scenarios, there is a continued

decline in permafrost extent and thickness due to heat penetrating into the subsurface. Thus, while near surface air temperature is the primary driver of permafrost thaw (Schuur et al., 2015), the rate of heat penetration through the soil and bedrock determines the time lag in permafrost response. The lag time of permafrost response following a change in surface air temperature presented in my results is an average over the area of a grid cell. Lag time naturally will vary depending on the rock type, bedrock depth, moisture content of the soil, porosity etc. Any variable that influences the time scale of the mechanisms of heat penetration through the soil column will affect the response time of permafrost.

Recent studies have projected that permafrost thaw will increase with increasing surface air temperature and the severity of the thaw will depend on the emissions scenarios (Koven et al., 2013; Slater & Lawrence, 2013; Wang & Guo, 2016). Wang & Guo (2016) analyzed the loss of permafrost area projected for different regions under different Representative Concentration Pathways (RCPs) to the year 2100. In the scenarios analyzed by Wang & Guo (2016), Arctic temperature is projected to increase, and by 2099 Arctic permafrost extent declines by 32 % - 79 % relative to 1986-2005, depending on the scenario. For example, for a business as usual scenario, RCP8.5, Wang & Guo (2016) found that permafrost declined by 79 % by the year 2100 with a temperature change of 8.0 °C, but for more ambitious mitigation scenarios with a temperature change of 2.2 °C, there was a decline of 32 %. Although the results from the research of Wang & Guo (2016) are not directly comparable to my results due to pathway differences, the overall conclusions remain similar. In scenarios with less mitigation, the overall loss of permafrost extent is greater. Comparing temperature changes in this study to those of Wang & Guo (2016), this study suggests a loss 50.4 % of permafrost area by the year 2100 relative to the 1986-2005 mean following SSP5-8.5 (change of 4.45 °C) and a 42.8 % loss relative to 1986-2005 mean by the year 2100 following SSP4-3.4 (change of 1.54 °C).

The findings presented in this work on the effect of overshoot scenarios on permafrost area are supported by other studies (e.g. Boucher et al., 2012). Boucher et al. (2012) used the Hadley Centre Earth System Model (HadGEM2-ES) with idealized climate change scenarios to analyze the reversibility of a number of different climate variables, including permafrost area. In their scenarios, CO_2 concentration increases by 1 % from pre-industrial levels to four times the pre-industrial level (ramp up phase) before decreasing at the same rate (ramp down phase). Boucher et al. (2012) found that land permafrost area has a hysteresis effect with a loss of about 20 % in the ramp down, relative to the same CO_2 concentration level from the ramp up. I found a similar hysteresis effect, with continental permafrost area in the overshoot scenarios recovering to between 71.1 % - 84.5 % when temperature recovers to the temperature seen prior to the overshoot (Table 3.1). Due to scenario differences, the results of Boucher et al. (2012) are not directly comparable to the results in this thesis. However, Boucher et al. (2012) and the results of this work agree that in overshoot scenarios permafrost area recovery is roughly 80 % relative to the area at a similar temperature prior to the overshoot. This suggests that temperature overshoot will have irreversible effects on permafrost degradation across the Arctic by the year 2500.

Compared to earlier studies, this research is based on model simulations for longer time horizons, allowing more time for permafrost to respond to the surface air temperature change. The ability to run simulations for longer periods of time is important because of the centuries required for heat to penetrate to deeper soil layers, and therefore adequately represent the delayed effect of the warming on permafrost. Results suggest that effects on permafrost area and thickness will be more severe in high temperature overshoot scenarios compared to low overshoot scenarios due to the continued thaw of permafrost following a higher temperature overshoot. This continued thaw is a result of the time required for the ground to equilibrate with cooler temperatures. The lower the surface air temperature following the overshoot, the more likely that permafrost can be restored.

It should be noted that while the UVic model simulates northern permafrost and variables that affect it, such as the active layer thickness, surface air and ground temperature, there are a few limitations within the model. For instance, the model simulates a warm temperature bias in parts of central Yukon and southern Canada and a lack of permafrost in eastern Canada and sections of Europe and northern Asia. While the warm near surface air temperature bias discussed in section 3.1.1 could have implications on the results, model validation suggested that the warm near surface air temperature bias did not penetrate to depth and therefore permafrost simulation was likely not impeded. Some of these limitations are the result of using a model with a coarse resolution. I chose to use the UVic ESCM for this study for its computational efficiency, which allowed me to run multiple scenarios until the year 2500. This meant that the spatial resolution of the model was rather coarse, limiting the representation of small-scale effects. Kokelj et al. (2013) determined that abrupt permafrost thaw due to surface water pooling, loss of insulation and erosion, among other factors, are important to represent in the modelling of permafrost distribution and change. The UVic ESCM, like the majority of large-scale models, does not represent these processes due to the small scale (up to hundreds of meters) at which they occur. There is also a lack of land processes affected by sea level rise due to the resolution, such as bank erosion. Within the land surface scheme of the UVic ESCM, there is no lateral movement of groundwater within the soil and associated heat transfer is not represented. Consideration of lateral movement of ground water could lead to further melt of permafrost when soil temperatures are above freezing. The lack of small-scale process representation likely results in an underestimation of permafrost thaw due to the limitations thereby set on heat movement through the movement of water through the subsurface. A further limitation, although minor in affecting permafrost simulations in the UVic ESCM (Avis, 2012), is that the prescribed bedrock is limited to granite and fixed at a depth of 10 m. This limitation affects the heat transfer through the subsurface as different types of bedrock will have different specific heat capacities and thermal conductivities, and bedrock exists naturally at depths starting both above and below 10

m. The accurate movement of heat through the ground is important when modelling temperature sensitive variables. There is no sub-sea permafrost implemented in the UVic model and thus this work is limited to continental permafrost.

While this work does cover a broad range of scenario types, one caveat of the scenarios is that SSP1-2.6 and SSP5-3.4-OS following the overshoot do not reach exactly the same temperature and instead run parallel to each other. This scenario temperature difference makes isolating the impact of the overshoot more challenging.

Future work in the area of stabilization and overshoot scenarios and their implications is required to determine how different types of scenarios will affect other Earth system components and what the consequences are. This study illuminates a number of policy relevant research gaps in Earth system response that require further scenarios to be run, ideally with many different models. A knowledge gap that this research highlights is the temperature threshold at which permafrost will not be able to recover due to the soil column remaining above zero degrees. My results raise the question of whether or not there is a surface air temperature change value between 1.5 °C and 2.0 °C, relative to the pre-industrial that corresponds to the re-freezing of permafrost. Permafrost re-freezing when surface air temperature stabilized (below a 1.5 °C change) was seen in overshoot scenarios following the temperature overshoot, but in stabilization scenarios (all of which stabilized above 2 °C) no permafrost was found to re-freeze. Future work and model modifications that would improve the accuracy would include an in-depth look at the temperature sensitivities of processes that affect permafrost thaw or growth, such as snow cover and the inclusion of additional processes within the UVic model, of particular interest lateral movement of water, and surface pooling. In addition, a missing process that could be further investigated and eventually added to the permafrost component of the UVic ESCM is the concept of sudden thaw.

Chapter 5. Conclusions

With an increased use of climate change scenarios in policy the need for further research in the field of Earth system response is vital to informing future decisions. Research in the field of climate change scenarios, both stabilization and overshoot scenarios and their subsequent long term impact on the natural systems such as permafrost is limited. The results of this study show permafrost extent and thickness are affected by a change in near surface air temperature and under all scenarios permafrost thaw continues after global mean temperature stabilizes. When temperature increases following SSP5-8.5, the largest decrease in permafrost area extent, per 0.5 °C increase in surface air warming, was between 1.5 °C and 2 °C, while the largest overall decrease in permafrost was seen after a 3 °C change. The relationship between permafrost thaw and surface air temperature is non-linear. In the case of overshoot scenarios, when temperature recovers, permafrost re-freezes, but only to a fraction (70 % to 85 %) of the extent observed prior to the surface air temperature overshoot.

Research on how future climate change scenarios will impact permafrost extent and thickness is limited. This study contributes to not only a greater understanding of the effects of temperature change on the Northern Hemisphere permafrost but provides long-term projections that are lacking in many other modeling studies, which typically end at year 2100. In using the Shared Socio-economic Pathways (SSPs), this work provides up-to-date projections, which follow policy relevant scenarios. While the limitations of the UVic ESCM do impact the accuracy of results because of the missing small-scale interactions and processes, the model allows for long-term simulations while still including the majority of interactions between Earth system components. The ability to run long-term simulations is key to understanding the full effects of warming on permafrost as it takes centuries for heat to penetrate through the ground. The key findings of this research, the impact of overshoot scenarios on Arctic permafrost and the impact of long-term high temperature stabilization scenarios, have not been discussed in other studies.

My study supports the argument that there will be lasting change in the permafrost, and therefore, in northern landscapes even if global temperature stabilizes. In the best-case scenario from this study, a low-overshoot scenario, Arctic permafrost will not return by the year 2500 to the extent it was at prior to the overshoot should surface air temperature cool. The results of this work are far reaching. Globally, policy initiatives are using climate change scenarios, specifically the Coupled Model Intercomparison Phase 6 (CMIP6) scenarios, to help understand the possible consequences of climate change on different regions around the world. The north is a region being affected disproportionately by climate change. This work addresses the knowledge gap existing between future climate change scenarios, the current understanding Earth systems and the resulting effects on permafrost regions in the northern hemisphere in policy relevant scenarios.

Bibliography

Abbott, B. W., Jones, J. B., Schuur, E. A. G., Chapin III, F. S., Bowden, W. B., Bret-Harte, M. S., … Zimov, S. (2016). Biomass offsets little or none of permafrost carbon release from soils, streams, and wildfire: an expert assessment. *Environmental Research Letters*, *11*(3), 034014. https://doi.org/10.1088/1748-9326/11/3/034014

AMAP, 2017. Snow, Water, Ice and Permafrost in the Arctic (SWIPA) 2017. Arctic Monitoring and Assessment Programme (AMAP), Oslo, Norway. (n.d.). Retrieved from https://www.amap.no/documents/doc/snow-water-ice-and-permafrost-in-the-arctic-swipa-2017/1610

Anisimov, O. A., D.G., V., Callaghan, T., Furgal, C., Merchant, H., Prowse, T. D., … Walsh, J. E. (2007). Polar regions (Arctic and Antarctic). In *Climate Change 2007: Impacts, Adaption and Vulnerability. Contributionn of Working Group II to the Fourth Assessment Report of the International Panel on Climate Change*. Retrieved from http://scholar.google.com/scholar?q=related:i9IfiKZTJk4J:scholar.google.com/&hl=en&num=30&as_sdt=0,5

Avis, C. A. (2012). *Simulating the Present-Day and Future Distribution of Permafrost in the UVic Earth System Climate Model, PhD Thesis*. University of Victoria.

Avis, C. A., Weaver, A. J., & Meissner, K. J. (2011). Reduction in areal extent of high-latitude wetlands in response to permafrost thaw. *Nature Geoscience*, *4*(7), 444–448. https://doi.org/10.1038/ngeo1160

Barrere, M., Domine, F., Belke-Brea, M., Sarrazin, D., Barrere, M., Domine, F., … Sarrazin, D. (2018). Snowmelt Events in Autumn Can Reduce or Cancel the Soil Warming Effect of Snow–Vegetation Interactions in the Arctic. *Journal of Climate*, *31*(23), 9507–9518. https://doi.org/10.1175/JCLI-D-18-0135.1

Berteaux, D., Gauthier, G., Domine, F., Ims, R. A., Lamoureux, S. F., Lévesque, E., & Yoccoz, N. (2017). Effects of changing permafrost and snow conditions on tundra wildlife: critical places and times. *Arctic Science*, *3*(2), 65–90. https://doi.org/10.1139/as-2016-0023

Biskaborn, B. K., Smith, S. L., Noetzli, J., Matthes, H., Vieira, G., Streletskiy, D. A., … Lantuit, H. (2019). Permafrost is warming at a global scale. *Nature Communications*, *10*(1), 1–11. https://doi.org/10.1038/s41467-018-08240-4

Bokhorst, S., Pedersen, S. H., Brucker, L., Anisimov, O., Bjerke, J. W., Brown, R. D., … Callaghan, T. V. (2016). Changing Arctic snow cover: A review of recent developments and assessment of future needs for observations, modelling, and impacts. *Ambio*, *45*(5), 516–537. https://doi.org/10.1007/s13280-016-0770-0

Boucher, O., Halloran, P. R., Burke, E. J., Doutriaux-Boucher, M., Jones, C. D., Lowe, J., … Wu, P. (2012). Reversibility in an Earth System model in response to CO 2 concentration changes. *Environmental Research Letters*, *7*(2), 024013. https://doi.org/10.1088/1748-9326/7/2/024013

Boucher, O., D. Randall, P. Artaxo, C. Bretherton, G. Feingold, P. Forster, V.-M. Kerminen, Y. Kondo, H. Liao, U. Lohmann, P. Rasch, S.K. Satheesh, S. Sherwood, B. Stevens and X.Y. Zhang, 2013: Clouds and Aerosols. In: Climate Change 2013: The Physical Science Basis. Contribution of Working Group I to the Fifth Assessment Report of the Intergovernmental Panel on Climate Change [Stocker, T.F., D. Qin, G.-K. Plattner, M. Tignor, S.K. Allen, J. Boschung, A. Nauels, Y. Xia, V. Bex and P.M. Midgley (eds.)]. Cambridge University Press, Cambridge, United Kingdom and New York, NY, USA.

Brown, J., Ferrians, O. J., Heginbottom, J. A., & Melnikov, E. S. (1997). *Circum-Arctic Map of Permafrost and Ground Ice Conditions*.

Brown, R. J. E. (2014). The Distribution of Permafrost and Its Relation to Air Temperature in Canada and the U.S.S.R. *Arctic*, *13*(3), 163–177. https://doi.org/10.14430/arctic3697

Burgess, B., & Smith, S. (2002). A digital database of permafrost thickness in Canada. https://doi.org/doi: doi:10.4095/213043.

Chadburn, S. E., Burke, E. J., Cox, P. M., Friedlingstein, P., Hugelius, G., & Westermann, S. (2017). An observation-based constraint on permafrost loss as a function of global warming. *Nature Climate Change*, *7*(5), 340–344. https://doi.org/10.1038/nclimate3262

Circum-Arctic Map of Permafrost and Ground-Ice Conditions, Version 2 | National Snow and Ice Data Center. (2019). Retrieved October 31, 2019, from https://nsidc.org/data/GGD318/versions/2

Circumpolar Active Layer Monitoring. (2019). Retrieved October 31, 2019, from https://www2.gwu.edu/~calm/

Daniel, J., Velders, G. J. M., Morgenstern, O., Toohey, D., Wallington, T., & Wuebbles, D. (2011). *A Focus on Options and Information for Policymakers, in UNEP/WMO Scientific assessment of ozone depletion: 2010*.

Eby, M., Zickfeld, K., Montenegro, A., Archer, D., Meissner, K. J., & Weaver, A. J. (2009). Lifetime of anthropogenic climate change: Millennial time scales of potential CO2 and surface temperature perturbations. *Journal of Climate*, *22*(10), 2501–2511. https://doi.org/10.1175/2008JCLI2554.1

Ehlert, D., & Zickfeld, K. (2018). Irreversible ocean thermal expansion under carbon dioxide removal. *Earth System Dynamics*, *9*(1), 197–210. https://doi.org/10.5194/esd-9-197-2018

Etminan, M., Myhre, G., Highwood, E. J., & Shine, K. P. (2016). Etminan, M., Myhre, G., Highwood, E. J., & Shine, K. P. (2016). Radiative forcing of carbon dioxide, methane, and nitrous oxide: A significant revision of the methane radiative forcing. *Geophysical Research Letters*, *43*(24), 12,614-12,623. https://doi.org/10.1002/2016GL071930

Eyring, V., Bony, S., Meehl, G. A., Senior, C. A., Stevens, B., Stouffer, R. J., & Taylor, K. E. (2016). Overview of the Coupled Model Intercomparison Project Phase 6 (CMIP6) experimental design and organization. *Geoscientific Model Development*, *9*(5), 1937–1958. https://doi.org/10.5194/gmd-9-1937-2016

Fanning, A. F., & Weaver, A. J. (1996). An atmospheric energy-moisture balance model: Climatology, interpentadal climate change, and coupling to an ocean general circulation model. *Journal of Geophysical Research: Atmospheres*, *101*(D10), 15111–15128. https://doi.org/10.1029/96JD01017

Fuss, S., Jones, C. D., Kraxner, F., Peters, G. P., Smith, P., Tavoni, M., … Yamagata, Y. (2016). Research priorities for negative emissions. *Environmental Research Letters*, *11*(11), 115007. https://doi.org/10.1088/1748-9326/11/11/115007

Gent, P. R., Danabasoglu, G., Donner, L. J., Holland, M. M., Hunke, E. C., Jayne, S. R., … Zhang, M. (2011). The community climate system model version 4. *Journal of Climate*, *24*(19), 4973–4991. https://doi.org/10.1175/2011JCLI4083.1

Gibson, C. M., Chasmer, L. E., Thompson, D. K., Quinton, W. L., Flannigan, M. D., & Olefeldt, D. (2018). Wildfire as a major driver of recent permafrost thaw in boreal peatlands. *Nature Communications*, *9*(1), 3041. https://doi.org/10.1038/s41467-018-05457-1

Gillett, N. P., Arora, V. K., Zickfeld, K., Marshall, S. J., & Merryfield, W. J. (2011). Ongoing climate change following a complete cessation of carbon dioxide emissions. *Nature Geoscience*, *4*(2), 83–87. https://doi.org/10.1038/ngeo1047

Global Terrestrial Network for Permafrost (GTN-P). (n.d.). Retrieved September 30, 2019, from https://gtnp.arcticportal.org/data/data-download

Gruber, S. (2012). Derivation and analysis of a high-resolution estimate of global permafrost zonation. *The Cryosphere*, *6*(1), 221–233. https://doi.org/10.5194/tc-6-221-2012

Guo, D., & Wang, H. (2016). CMIP5 permafrost degradation projection: A comparison among different regions. *Journal of Geophysical Research*, *121*(9), 4499–4517. https://doi.org/10.1002/2015JD024108

Hjort, J., Karjalainen, O., Aalto, J., Westermann, S., Romanovsky, V. E., Nelson, F. E., … Luoto, M. (2018). Degrading permafrost puts Arctic infrastructure at risk by mid-century. *Nature Communications*, *9*(1), 5147. https://doi.org/10.1038/s41467-018-07557-4

Intergovernmental Panel on Climate Change. (2014). Anthropogenic and Natural Radiative Forcing. In Climate Change 2013 – The Physical Science Basis: Working Group I Contribution to the Fifth Assessment Report of the Intergovernmental Panel on Climate Change (pp. 659-740). Cambridge: Cambridge University Press. doi:10.1017/CBO9781107415324.018

Jeong, D. Il, Sushama, L., Diro, G. T., Khaliq, M. N., Beltrami, H., & Caya, D. (2016). Projected changes to high temperature events for Canada based on a regional climate model ensemble. *Climate Dynamics*, *46*(9–10), 3163–3180. https://doi.org/10.1007/s00382-015-2759-y

Johnston, E. R., Hatt, J. K., He, Z., Wu, L., Guo, X., Luo, Y., … Konstantinidis, K. T. (2019). Responses of tundra soil microbial communities to half a decade of experimental warming at two critical depths. *Proceedings of the National Academy of Sciences of the United States of America*, 201901307. https://doi.org/10.1073/pnas.1901307116

Jolly, W. M., Cochrane, M. A., Freeborn, P. H., Holden, Z. A., Brown, T. J., Williamson, G. J., & Bowman, D. M. J. S. (2015). Climate-induced variations in global wildfire danger from 1979 to 2013. *Nature Communications*, *6*, 7537. Retrieved from https://doi.org/10.1038/ncomms8537

Jones, B. M., Grosse, G., Arp, C. D., Miller, E., Liu, L., Hayes, D. J., & Larsen, C. F. (2015). Recent Arctic tundra fire initiates widespread thermokarst development. *Scientific Reports*, *5*(1), 15865. https://doi.org/10.1038/srep15865

Jones, C. D., Ciais, P., Davis, S. J., Friedlingstein, P., Gasser, T., Peters, G. P., … Wiltshire, A. (2016). Simulating the Earth system response to negative emissions. *Environmental Research Letters*, *11*(9), 1–11. https://doi.org/10.1088/1748-9326/11/9/095012

Kanevskiy, M., Shur, Y., Jorgenson, M. T., Ping, C.-L., Michaelson, G. J., Fortier, D., … Tumskoy, V. (2013). Ground ice in the upper permafrost of the Beaufort Sea coast of Alaska. *Cold Regions Science and Technology*, *85*, 56–70. https://doi.org/10.1016/J.COLDREGIONS.2012.08.002

Keller, D. P., Oschlies, A., & Eby, M. (2012). A new marine ecosystem model for the University of Victoria Earth System Climate Model. *Geoscientific Model Development*, *5*(5), 1195–1220. https://doi.org/10.5194/gmd-5-1195-2012

Kholodov, A. L., Natali, S., Loranty, M. M., & Romanovsky, V. E. (2016). Mechanisms of vegetation protective effect on thermal state of permafrost in Alaska. *American Geophysical Union, Fall Meeting 2016, Abstract #B43C-0619*. Retrieved from http://adsabs.harvard.edu/abs/2016AGUFM.B43C0619K

Kokelj, S. V., Lacelle, D., Lantz, T. C., Tunnicliffe, J., Malone, L., Clark, I. D., & Chin, K. S. (2013). Thawing of massive ground ice in mega slumps drives increases in stream sediment and solute flux across a range of watershed scales. *Journal of Geophysical Research: Earth Surface*, *118*(2), 681–692. https://doi.org/10.1002/jgrf.20063

Koven, C. D., Riley, W. J., Stern, A., Koven, C. D., Riley, W. J., & Stern, A. (2013). Analysis of Permafrost Thermal Dynamics and Response to Climate Change in the CMIP5 Earth System Models. *Journal of Climate*, *26*(6), 1877–1900. https://doi.org/10.1175/JCLI-D-12-00228.1

Koven, C. D., Ringeval, B., Friedlingstein, P., Ciais, P., Cadule, P., Khvorostyanov, D., … Tarnocai, C. (2011). Permafrost carbon-climate feedbacks accelerate global warming. *Proceedings of the National Academy of Sciences of the United States of America*, *108*(36), 14769–14774. https://doi.org/10.1073/pnas.1103910108

Li, X. (2017). *Exploring the Reversibility of Marine Climate Change Impacts under CO 2 Removal from the Atmosphere, MSc Thesis*. Simon Fraser University.

Loranty, M. M., Abbott, B. W., Blok, D., Douglas, T. A., Epstein, H. E., Forbes, B. C., … Walker, D. A. (2018). Reviews and syntheses: Changing ecosystem influences on soil thermal regimes in northern high-latitude permafrost regions. *Biogeosciences*, *15*(17), 5287–5313. https://doi.org/10.5194/bg-15-5287-2018

Lowe, J. A., Hewitt, C. D., van Vuuren, D. P., Johns, T. C., Stehfest, E., Royer, J.-F., & van der Linden, P. J. (2009). New Study For Climate Modeling, Analyses, and Scenarios. *Eos, Transactions American Geophysical Union*, *90*(21), 181–182. https://doi.org/10.1029/2009EO210001

Macdougall, A. H. (2013). Reversing climate warming by artificial atmospheric carbon-dioxide removal: Can a Holocene-like climate be restored? *Geophysical Research Letters*, *40*(20), 5480–5485. https://doi.org/10.1002/2013GL057467

MacDougall, A. H., Zickfeld, K., Knutti, R., & Matthews, H. D. (2015). Sensitivity of carbon budgets to permafrost carbon feedbacks and non-CO2 forcings. *Environmental Research Letters*, *10*(12), 125003. https://doi.org/10.1088/1748-9326/10/12/125003

Matthes, K., Funke, B., Andersson, M. E., Barnard, L., Beer, J., Charbonneau, P., … Versick, S. (2017). Solar forcing for CMIP6 (v3.2). *Geoscientific Model Development*, *10*(6), 2247–2302. https://doi.org/10.5194/gmd-10-2247-2017

Matthes, K., Funke, B., Kruschke, T., & Wahl, S. (2017). *input4MIPs.SOLARIS-HEPPA.solar.CMIP.SOLARIS-HEPPA-3-2*. https://doi.org/10.22033/ESGF/input4MIPs.1122

Matthews, H. D., & Caldeira, K. (2008). Stabilizing climate requires near-zero emissions. *Geophysical Research Letters*, *35*(4), L04705. https://doi.org/10.1029/2007GL032388

Meinshausen, M., Vogel, E., Nauels, A., Lorbacher, K., Meinshausen, N., Etheridge, D. M., … Weiss, R. (2017). Historical greenhouse gas concentrations for climate modelling (CMIP6). *Geoscientific Model Development*, *10*(5), 2057–2116. https://doi.org/10.5194/gmd-10-2057-2017

Mengis, N., Keller, D., MacDougall, A., Eby, M., Wright, N., Meissner, K., Oschlies, A., Schmittner, A., Matthews, D., Zickfeld, K. (n.d.). Evaluation of the University of Victoria Earth System Climate Model version 2.10 (UVic ESCM 2.10). *Geoscientific Model Development*.

Mladjic, B., Sushama, L., Khaliq, M. N., Laprise, R., Caya, D., & Roy, R. (2011). Canadian RCM projected changes to extreme precipitation characteristics over Canada. *Journal of Climate*, *24*(10), 2565–2584. https://doi.org/10.1175/2010JCLI3937.1

Movilla, J. (2019). *45 A Case Study: Variability in the Calcification Response of Mediterranean Cold-Water Corals to Ocean Acidification*. https://doi.org/10.1007/978-3-319-91608-8_45

Myhre, G., Shindell, D., Bréon, F.-M., Collins, W., Fuglestvedt, J., Huang, J., … Zhan, H. (2013). Anthropogenic and Natural Radiative Forcing: In Climate Change 2013: The Physical Science Basis. Contribution of Working Group I to the Fifth Assessment Report of the Intergovernmental Panel on Climate Change. *Cambridge University Press, Cambridge, United Kingdom and New York, NY, USA*, 659–740. https://doi.org/10.1017/ CBO9781107415324.018

Natali, S. M., Schuur, E. A. G., Webb, E. E., Pries, C. E. H., & Crummer, K. G. (2014). Permafrost degradation stimulates carbon loss from experimentally warmed tundra. *Ecology*, *95*(3), 602–608. https://doi.org/10.1890/13-0602.1

Nitze, I., Grosse, G., Jones, B., Arp, C., Ulrich, M., Fedorov, A., & Veremeeva, A. (2017). Landsat-Based Trend Analysis of Lake Dynamics across Northern Permafrost Regions. *Remote Sensing*, *9*(7), 640. https://doi.org/10.3390/rs9070640

O'Neill, B. C., Tebaldi, C., Van Vuuren, D. P., Eyring, V., Friedlingstein, P., Hurtt, G., … Sanderson, B. M. (2016). The Scenario Model Intercomparison Project (ScenarioMIP) for CMIP6. *Geoscientific Model Development*, *9*(9), 3461–3482. https://doi.org/10.5194/gmd-9-3461-2016

Obu, J., Westermann, S., Bartsch, A., Berdnikov, N., Christiansen, H. H., Dashtseren, A., … Zou, D. (2019). Northern Hemisphere permafrost map based on TTOP modelling for 2000–2016 at 1 km2 scale. *Earth-Science Reviews*, *193*(April), 299–316. https://doi.org/10.1016/j.earscirev.2019.04.023

Olefeldt, D., Goswami, S., Grosse, G., Hayes, D., Hugelius, G., Kuhry, P., … Turetsky, M. R. (2016). Circumpolar distribution and carbon storage of thermokarst landscapes. *Nature Communications*, *7*, 13043. Retrieved from https://doi.org/10.1038/ncomms13043

Pacanowski, R. C., Dixon, K., & Rosati, A. (1993). *The GFDL Modular Ocean Model User's Guide, Version 1.0*. Retrieved from https://www.gfdl.noaa.gov/wp-content/uploads/files/model_development/ocean/gfdl_tech_report_2_mom1_manual_v1.0_1991.pdf

Pachauri and others. (2014). *IPCC, 2014: Climate Change 2014: Synthesis Report. Contribution of Working Groups I, II and III to the Fifth Assessment Report of the Intergovernmental Panel on Climate Change [Core Writing Team, R.K. Pachauri and L.A. Meyer (eds.)]. IPCC, Geneva, Switzer*. https://doi.org/10.1017/CBO9781107415324

Pastick, N. J., Duffy, P., Genet, H., Rupp, T. S., Wylie, B. K., Johnson, K. D., … Knight, J. F. (2017). Historical and projected trends in landscape drivers affecting carbon dynamics in Alaska. *Ecological Applications*, *27*(5), 1383–1402. https://doi.org/10.1002/eap.1538

Pastick, N. J., Jorgenson, M. T., Goetz, S. J., Jones, B. M., Wylie, B. K., Minsley, B. J., … Jorgenson, J. C. (2019). Spatiotemporal remote sensing of ecosystem change and causation across Alaska. *Global Change Biology*, *25*(3), 1171–1189. https://doi.org/10.1111/gcb.14279

Pendleton, L., Hoegh-Guldberg, O., Albright, R., Kaup, A., Marshall, P., Marshall, N., … Hansson, L. (2019). The Great Barrier Reef: Vulnerabilities and solutions in the face of ocean acidification. *Regional Studies in Marine Science*, 100729. https://doi.org/10.1016/J.RSMA.2019.100729

Purdie, H., Anderson, B., Chinn, T., Owens, I., Mackintosh, A., & Lawson, W. (2014). Franz Josef and Fox Glaciers, New Zealand: Historic length records. *Global and Planetary Change*, *121*, 41–52. https://doi.org/10.1016/J.GLOPLACHA.2014.06.008

Quinton, W. L., Adams, J. R., Baltzer, J. L., Berg, A. A., Craig, J. R., & Johnson, E. (2016). *Permafrost Ecosystems in Transition : Understanding and Predicting Hydrological and Ecological Change in the Southern Taiga Plains , Northeastern British Columbia and Southwestern Northwest Territories*. 89–94.

Raynolds, M. K., Walker, D. A., Ambrosius, K. J., Brown, J., Everett, K. R., Kanevskiy, M., … Webber, P. J. (2014). Cumulative geoecological effects of 62 years of infrastructure and climate change in ice-rich permafrost landscapes, Prudhoe Bay Oilfield, Alaska. *Global Change Biology*, *20*(4), 1211–1224. https://doi.org/10.1111/gcb.12500

Rogelj, J., Den Elzen, M., Höhne, N., Fransen, T., Fekete, H., Winkler, H., … Meinshausen, M. (2016). Paris Agreement climate proposals need a boost to keep warming well below 2 °C. *Nature*, *534*(7609), 631–639. https://doi.org/10.1038/nature18307

Schaefer, K., Lantuit, H., Romanovsky, V. E., Schuur, E. A. G., & Witt, R. (2014). The impact of the permafrost carbon feedback on global climate. *Environmental Research Letters*, *9*(8), 085003. https://doi.org/10.1088/1748-9326/9/8/085003

Schäfer, S., Lawrence, M., Stelzer, H., Born, W., Low, S., Aaheim, A., … Vaughan, N. (2015). *Final report of the FP7 CSA project EuTRACE Removing Greenhouse Gases from the Atmosphere and Reflecting Sunlight away from Earth*. Retrieved from https://www.iass-potsdam.de/sites/default/files/files/rz_150715_eutrace_digital.pdf

Schmidt, A., Mills, M. J., Ghan, S., Gregory, J. M., Allan, R. P., Andrews, T., … Toon, O. B. (2018a). Volcanic Radiative Forcing From 1979 to 2015. *Journal of Geophysical Research: Atmospheres*, *123*(22), 12,491-12,508. https://doi.org/10.1029/2018JD028776

Schmidt, A., Mills, M. J., Ghan, S., Gregory, J. M., Allan, R. P., Andrews, T., … Toon, O. B. (2018b). Volcanic Radiative Forcing From 1979 to 2015. *Journal of Geophysical Research: Atmospheres*, *123*(22), 12491–12508. https://doi.org/10.1029/2018JD028776

Scholes, R. J., & Brown de Colstoun, E. (2011). ISLSCP II Global Gridded Soil Characteristics. *Daac.Ornl.Gov*, 1–3. https://doi.org/10.3334/ORNLDAAC/1004

Schuur, E. A. G., McGuire, A. D., Schädel, C., Grosse, G., Harden, J. W., Hayes, D. J., … Vonk, J. E. (2015). Climate change and the permafrost carbon feedback. *Nature*, *520*(7546), 171–179. https://doi.org/10.1038/nature14338

Schuur, Edward A. G., & Abbott, B. (2011). Climate change: High risk of permafrost thaw. *Nature*, *480*(7375), 32–33. https://doi.org/10.1038/480032a

Schuur, Edward A. G., Vogel, J. G., Crummer, K. G., Lee, H., Sickman, J. O., & Osterkamp, T. E. (2009). The effect of permafrost thaw on old carbon release and net carbon exchange from tundra. *Nature*, *459*(7246), 556–559. https://doi.org/10.1038/nature08031

Search, H., Journals, C., Contact, A., Iopscience, M., Jones, C. D., Ciais, P., … Wiltshire, A. (2016). Simulating the Earth system response to negative emissions. *Environmental Research Letters*, *11*(9), 095012. https://doi.org/10.1088/1748-9326/11/9/095012

Slater, A. G., & Lawrence, D. M. (2013). Diagnosing present and future permafrost from climate models. *Journal of Climate*, *26*(15), 5608–5623. https://doi.org/10.1175/JCLI-D-12-00341.1

Smith, C. J., Forster, P. M., Allen, M., Leach, N., Millar, R. J., Passerello, G. A., & Regayre, L. A. (2018). FAIR v1.3: a simple emissions-based impulse response and carbon cycle model. *Geosci. Model Dev*, *11*, 2273–2297. https://doi.org/10.5194/gmd-11-2273-2018

Smith, P., Davis, S. J., Creutzig, F., Fuss, S., Minx, J., Gabrielle, B., … Yongsung, C. (2016). Biophysical and economic limits to negative CO2 emissions. *Nature Climate Change*, *6*(1), 42–50. https://doi.org/10.1038/nclimate2870

Smith, S., & Burgess, M. (2000a). *Ground temperature database for northern Canada*. https://doi.org/10.4095/211804

Smith, S., & Burgess, M. (2000b). *Ground Temperature Database for Northern Canada*.

Stevens, B., Fiedler, S., Kinne, S., Peters, K., Rast, S., Müsse, J., … Mauritsen, T. (2017). MACv2-SP: A parameterization of anthropogenic aerosol optical properties and an associated Twomey effect for use in CMIP6. *Geoscientific Model Development*, *10*(1), 433–452. https://doi.org/10.5194/gmd-10-433-2017

Tokarska, K. B., & Zickfeld, K. (2015a). The effectiveness of net negative carbon dioxide emissions in reversing anthropogenic climate change. *Environmental Research Letters*, *10*(9). https://doi.org/10.1088/1748-9326/10/9/094013

Tokarska, K. B., & Zickfeld, K. (2015b). The effectiveness of net negative carbon dioxide emissions in reversing anthropogenic climate change. *Environmental Research Letters*, *10*(9), 94013. https://doi.org/10.1088/1748-9326/10/9/094013

Ulrich, M., Matthes, H., Schirrmeister, L., Schütze, J., Park, H., Iijima, Y., & Fedorov, A. N. (2017). Differences in behavior and distribution of permafrost-related lakes in Central Yakutia and their response to climatic drivers. *Water Resources Research*, *53*(2), 1167–1188. https://doi.org/10.1002/2016WR019267

Vaughan, N. E., & Gough, C. (2016). Expert assessment concludes negative emissions scenarios may not deliver. *Environmental Research Letters*, *11*(9). https://doi.org/10.1088/1748-9326/11/9/095003

Walvoord, M. A., & Kurylyk, B. L. (2016). Hydrologic Impacts of Thawing Permafrost—A Review. *Vadose Zone Journal*, *15*(6), 0. https://doi.org/10.2136/vzj2016.01.0010

Wang, Z., Kim, Y., Seo, H., Um, M.-J., & Mao, J. (2019). Permafrost response to vegetation greenness variation in the Arctic tundra through positive feedback in surface air temperature and snow cover. *Environmental Research Letters*, *14*(4), 044024. https://doi.org/10.1088/1748-9326/ab0839

Weaver, A. J., Eby, M., Wiebe, E. C., Ewen, T. L., Fanning, A. F., MacFadyen, A., … Wang, H. (2001). The UVic earth system climate model: Model description, climatology, and applications to past, present and future climates. *Atmosphere - Ocean*, *39*(4), 361–428. https://doi.org/10.1080/07055900.2001.9649686

Zhang, T, Barry, R., Knowles, K., Ling, F., & Armstrong, R. (2003). *Distribution of seasonally and perennially frozen ground in the Northern Hemisphere*.

Zhang, Tingjun. (2005). Influence of the seasonal snow cover on the ground thermal regime: An overview. *Reviews of Geophysics*, *43*(4), RG4002. https://doi.org/10.1029/2004RG000157

Zhang, Z., Zimmermann, N. E., Stenke, A., Li, X., Hodson, E. L., Zhu, G., … Poulter, B. (2017). Emerging role of wetland methane emissions in driving 21st century climate change. *Proceedings of the National Academy of Sciences of the United States of America*, *114*(36), 9647–9652. https://doi.org/10.1073/pnas.1618765114

Zickfeld, K., MacDougall, A. H., & Damon Matthews, H. (2016). On the proportionality between global temperature change and cumulative CO2 emissions during periods of net negative CO2 emissions. *Environmental Research Letters*, *11*(5). https://doi.org/10.1088/1748-9326/11/5/055006

Appendix A. CMIP6 Forcing Data

In this study, anthropogenic forcing from greenhouse gases (GHGs), stratospheric and tropospheric ozone, aerosols and stratospheric water-vapour from methane oxidization are considered. Natural forcing includes solar and volcanic. All data used in the creation of this dataset can be accessed from Input4Mip (https://esgf-node.llnl.gov/projects/input4mips/)on the Earth System Grid Federation (ESGF) unless otherwise specified. In the following, I describe how the input data file for the simulations with the University of Victoria Earth system climate model (UVic ESCM) was created. At the end of this section is an overview of each of the forcings created compared to the observational dataset of Piers Forster (Figure A.3).

Greenhouse gas (GHG) forcing

The UVic ESCM was forced with CO_2 concentration data (ppm) (Meinshausen et al., 2017). The model then internally calculates the radiative forcing. In contrast to that, radiative forcing for non-CO_2 gases are calculated externally and summed to be used as an additional model input, using concentration data of 45 GHGs (Meinshausen et al., 2017).

CO_2, N_2O and CH_4

In this study, I use updated radiative forcing formulations for CO_2, CH_4 and N_2O following the findings of Etminan et al. (2016).

Table A1: Calculations for CO_2, N_2O and CH_4 radiative forcing from (Etminan et al., 2016). Where C is the concentration of CO_2 (ppm), N is the concentration of N_2O (ppb) and M is the concentration of CH_4 (ppb). Source: (Etminan et al., 2016)

Gas	Simplified Expression	Coefficients
CO_2	$[a_1(C-C_o)^2+b_1\lvert C-C_o\rvert+c_1N+5.36]\times\ln(C/C_o)$	a1=-2.4 x 10^{-7} Wm-2 ppm^{-1} b1=7.2 x 10^{-4} Wm-2 ppm^{-1} c1=-2.1 x 10^{-4} Wm-2 ppb^{-1}
N_2O	$[a_2\boldsymbol{C}+b_2\boldsymbol{N}+c_2M+.0117](\sqrt{N}-\sqrt{N_o})$	a2=-8.0 x 10^{-6} Wm-2 ppm^{-1} b2=4.2 x 10^{-6} Wm-2 ppb^{-1} c2=-4.9 x 10^{-6} Wm-2 ppb^{-1}
CH_4	$[a_3\boldsymbol{M}+b_3\boldsymbol{N}+0.043]](\sqrt{M}-\sqrt{M_o})$	a3=-1.3 x 10^{-6} Wm-2 ppb^{-1} b3=-8.2 x 10^{-6} Wm-2 ppb^{-1}

Note: C,N and M are concentrations for the time that forcing is required. C_o, N_o and M_o are initial concentrations. Any terms in square brackets are the mean of the gas initial and final concentrations, e.g., **M**=0.5(M+M_o) for methane). The expressions are valid in the ranges of 180-2000 ppm for CO_2, 200-525 ppb for N_2O, and 340-3500 ppb for CH_4. For further reference refer to Etminan et al., 2016.

Radiative forcing of other greenhouse gases (GHGs) was calculated using the formulations in Table 8.A.1 from the IPCC AR5 (Myhre et al., 2013). Meinshausen et al. (2017) introduced three options for calculating radiative forcing from GHG concentrations; for this study I chose to use the option which uses specific calculations from all available 44 GHGs, rather than treating some species in a similar manner, consistent with Option 1 from Meinshausen et al. (2017). Figure A1 shows the difference in radiative forcing between each of these methods.

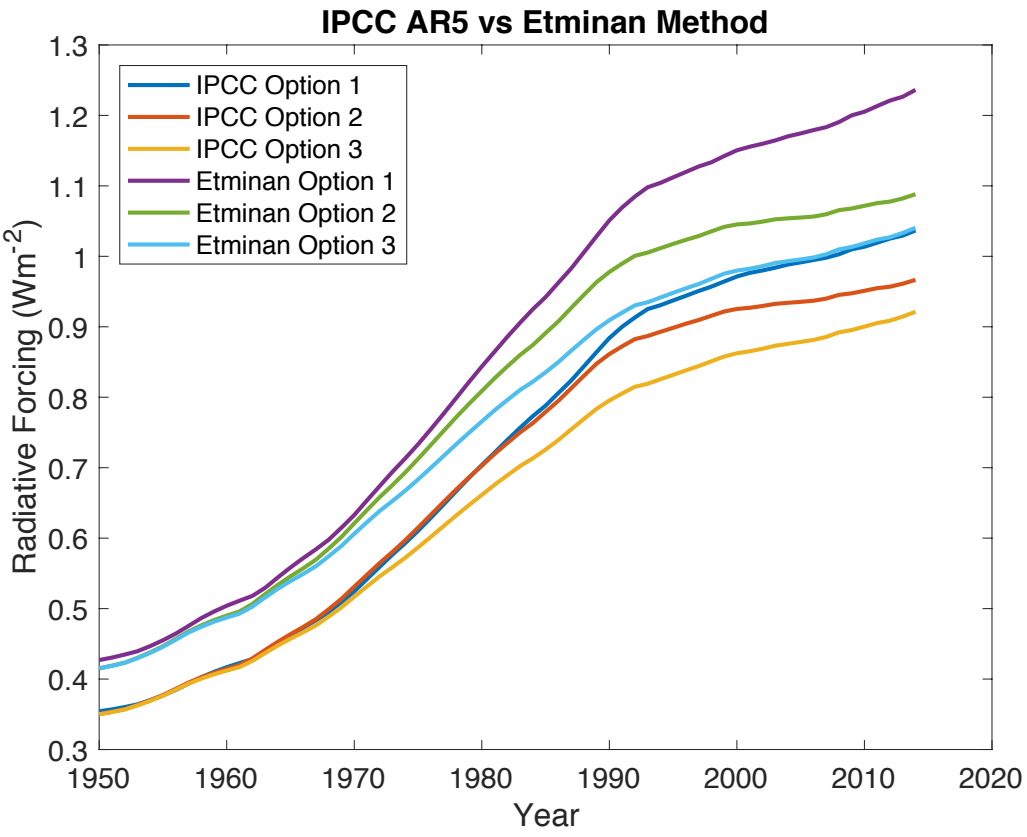

Figure A.1: Possible methods for calculating radiative forcing for CO_2, CH_4 and N_2O from 1750 to 2015..

Aerosol Optical Depth

Aerosol optical depth (AOD) 3D input data for the UVic ESCM was created using a UVic grid with the scripts and data provided by Stevens et al. (2017). Data provided describes nine different plumes globally which are scaled with time to produce monthly

aerosol optical depth forcing for the years 1850-2018 (Stevens et al., 2017). For the future projection of the years 2018-2100, I used the same scripts but with input data from Fiedler et al. (2019). The input data is historical aerosol forcing scaled to represent the 2018 to 2100 period for different Shared Socio-Economic Pathways (SSPs). To extend aerosol optical depth data from 2100 to 2500, the last year of available data was repeated so to include the seasonal cycles. Figure A.2 illustrates the spatial pattern of the AOD data for the year 2011.

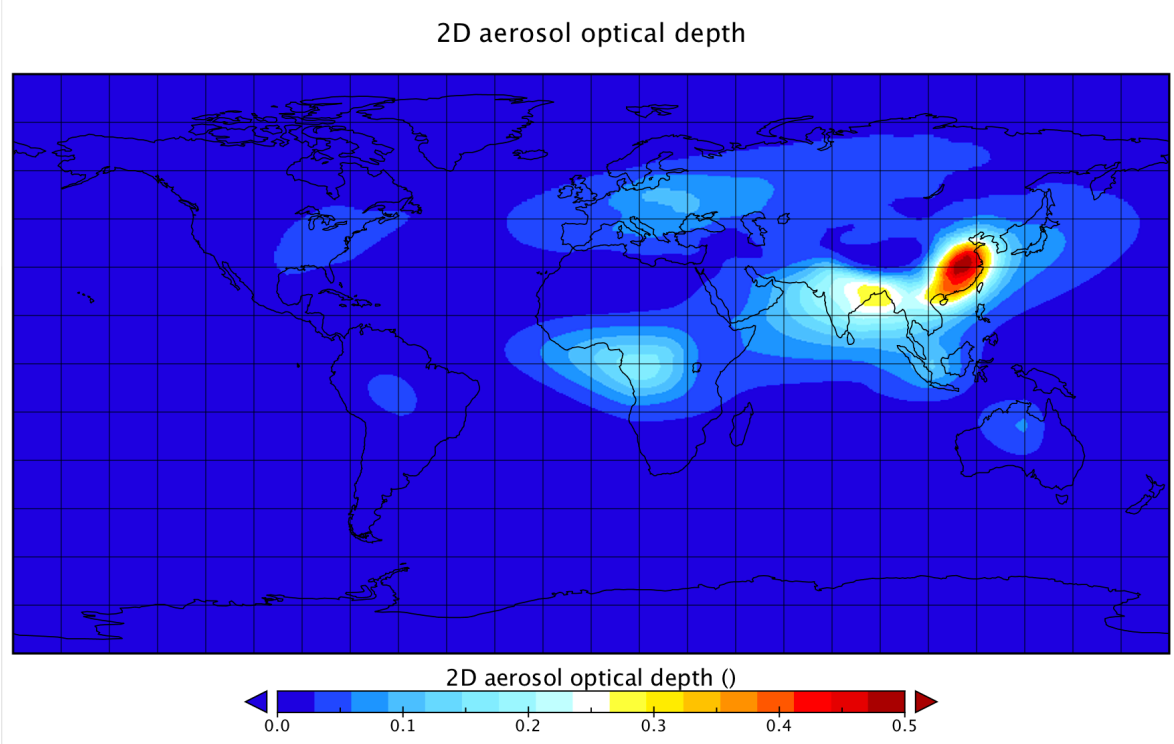

Figure A.2: Mean Aerosol optical depth for the year 2011 with no scaling factor applied.

Realizing that the AOD input caused too great a negative forcing in the historical period, a scaling factor was implemented into the UVic ESCM, which allows to scale aerosol forcing from AOD data. For this study, the scaling factor was set to 0.7, which gives a globally averaged forcing of -1.0331 Wm^{-2} in 2011, consistent with the IPCC AR5 range estimate of between -2.3 and .2 Wm^{-2} (Boucher et al., 2013).

Stratospheric water-vapour from methane oxidation (CH_4ox)

To calculate the radiative forcing of stratospheric water-vapour from methane oxidation, I followed the formulation of Smith et al. (2018) and simply multiplies CH_4 effective radiative forcing (ERF) by 12%. The radiative forcing calculation of CH_4ox accordingly requires the same concentrations as the formulation of CH_4 radiative forcing: (A1)

$$RF\_CH_4ox(t) = ((-1.3e-6*(\frac{CH4(n)+CH4pi}{2})-8.2e-6*(\frac{N2O(n)+N2Opi}{2})+.043) * (\sqrt{(CH4(n))}-\sqrt{CH4pi})*.12 \quad \text{(A1)}$$

where Xpi represents the pre-industrial value for the respective GHG and methane ERF is calculated according to Table A.1.

Ozone

Tropospheric Ozone

To calculate the radiative forcing of tropospheric ozone, the equations from Smith et al. (2018) were used:

$$FO_{3tr} = \beta_{CH4}(C_{CH_4}-C_{CH_4,pi})+\beta_{NO_x}(E_{NO_x}-E_{NO_{x,pi}})+\beta_{CO}(E_{CO}-E_{CO,pi}) + \beta_{NMVOC}(E_{NMVOC}-E_{NMVOC,pi})+f(T) \quad \text{(A2)}$$

$$f(T) = \min\{0, 0.032ext(-1.35T)-0.032 \quad \text{(A3)}$$

where $\boldsymbol{\beta}$ are transfer coefficients, $\boldsymbol{C_X}$ are concentrations and $\boldsymbol{E_X}$ are emissions of the respective species, *pi* are the pre-industrial constant for their specific species. Note that *f(T)* was not included in the calculations because the atmospheric model being applied is not dynamic. Pre-industrial (*pi*) values were taken from Table 4 of Smith et al. (2018).

Stratospheric Ozone

Following Smith et al. (2018) radiative forcing of stratospheric ozone was calculated using:

$$F_{O_{sst}} = a(bs)^c \tag{A4}$$

$$a = -1.46E^{-5}, b = 2.05E^{-3}, c = 1.03$$

$$s = r_{CFC11} \sum_{i \in ODS} (n_{Cl}(i)Ci \frac{r_i}{r_{CFC11}} + 45 n_{Br}(i) C_i \frac{r_i}{r_{CFC11}}) \tag{A5}$$

where a, b and c are curve fitting parameters. Equivalent stratospheric chlorine of all ozone depleting substances (ODS) is represented by equation $(A5)$ as a function of ODS concentrations. The parameters r_i are fractional release values for each ODS as defined by Daniel et al. (2011) and can be found in Table 2 of Smith et al., 2016. Halon 1202 data are not provided by Input4Mips and therefore were not included.

Volcanic Forcing

Volcanic radiative forcing data is provided to the year 2018 (Schmidt et al., 2018a). To extend the volcanic forcing to the year 2500, the last value of the forcing was set to zero. Following CMIP6 spin-up forcing recommendations (Eyring et al., 2016) volcanic forcing is applied as an anomaly relative to the 1850 to 2014 period in the UVic ESCM.

Solar Forcing

Solar constant data for 1850 to 2300 was accessed from Input4Mips (Matthes et al., 2017). Following CMIP6 spin-up forcing recommendations (Eyring et al., 2016) spin-up values were set to the mean of 1850-1873, equal to 1360.7471 Wm-1. The available monthly data was annually averaged. From 2300, the dataset was extended to 2500 by repeating the last 13-year solar cycle. This is consistent with CMIP6 protocol.

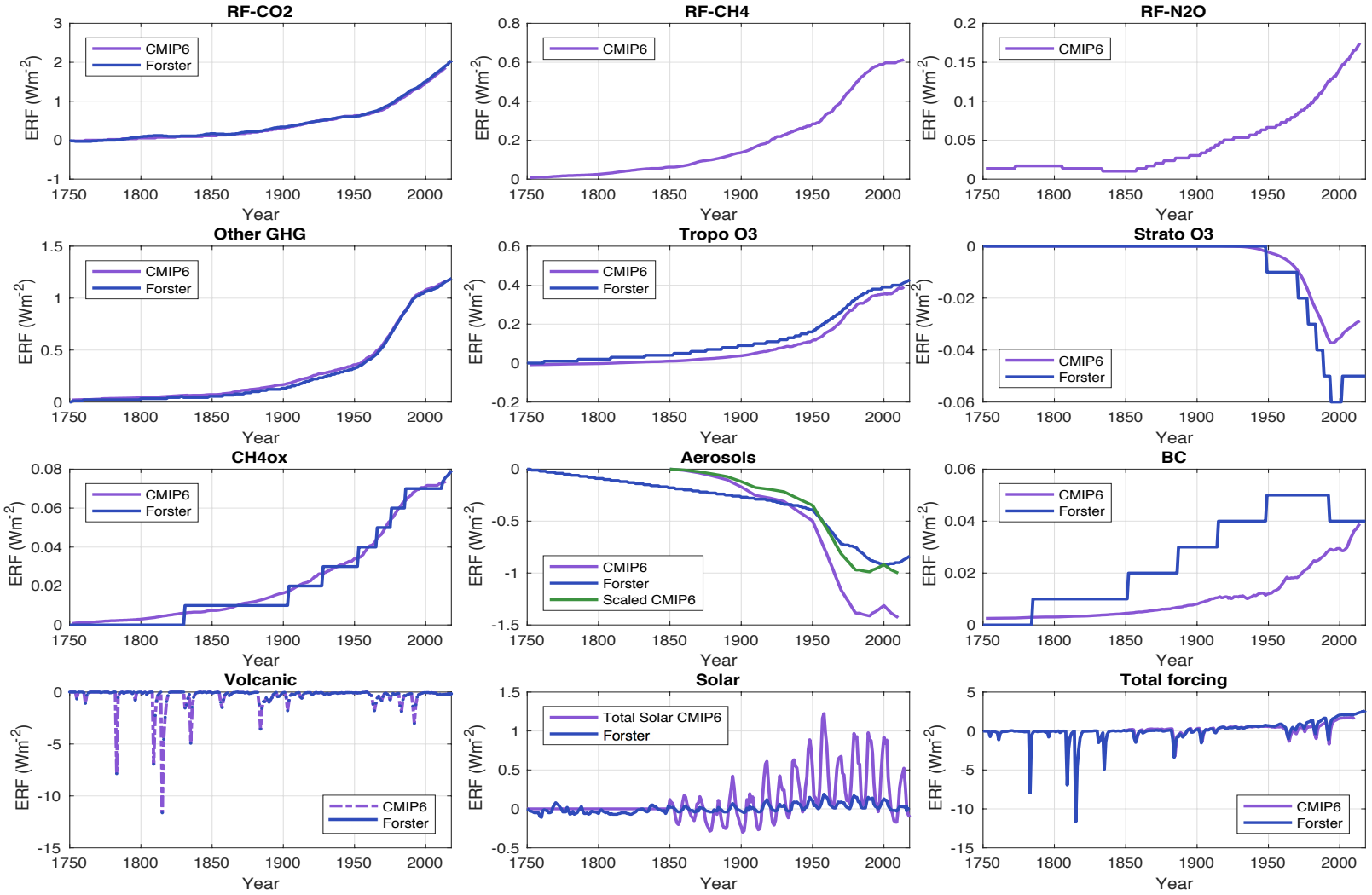
RF-CO2
RF-CH4
RF-N2O
Other GHG
Tropo O3
Strato O3
CH4ox
Aerosols
BC
Volcanic
Solar
Total forcing
CMIP6
Forster
Scaled CMIP6
Total Solar CMIP6
ERF (Wm-2)
Year

Figure A.3. Calculated effective radiative forcing (ERF) compared to the compiled observation dataset provided by Piers Forster through personal communication to be used in IPCC AR6. Aerosol radiative forcing is scaled by a factor of 0.7 in the UVic ESCM from CMIP6 data. Other GHG includes 42 greenhouse gases as described in Meinshausen et al. (2017). Solar forcing is total incoming solar (CMIP6 data) compared to incoming solar at the top of the atmosphere (Forster) from (Matthes et al. (2017). RF-GHG represents the radiative forcing (RF) from a specific greenhouse gas (GHG), the observational dataset is from Myhre et al. (2013), and Tropo O3 and Strato O3 are the radiative forcing from tropospheric and stratospheric ozone, respectively. CH4ox is radiative forcing from oxidized CH_4 and BC is black carbon. Observed volcanic forcing is from Schmidt et al. (2018b).

Appendix B

Table B1: Permafrost depth data used to compare to UVic ESCM model simulations. Further information on this dataset can be accessed from *("Circum-Arctic Map of Permafrost and Ground-Ice Conditions, Version 2 | National Snow and Ice Data Center," 2016.)*

SITE LOCATION	SITE IDENTIFIER	LAT (°N)	LONG (°W)	Base IBPF (m)
Fort Providence A47	EPB #70	61.44	117.37	71
West Whitefish	EPB #151	65.56	124.60	299
Hume River D53	EPB #100	65.87	129.18	390
Tedji Lake K24	EPB #253	67.73	126.83	375
Aklavik F17		68.10	135.07	161
Aklavik F38		68.12	135.15	841
Aklavik A37		68.27	135.13	67
Napoiak F31		68.33	134.90	92
Beaver House H13	EPB # 89	68.37	135.55	112
Wolverine H34		68.38	130.63	471
Scurry Inuvik D54		68.38	133.73	384
Crossley Lake SK60		68.50	129.48	215
Napartok M01		68.52	134.53	71
Kuglauk N02		68.53	131.52	98
Skakgatlatachig D50		68.65	133.95	675
East Reindeer P60		68.67	133.72	158
East Reindeer A01		68.67	134.00	214
Unak B11		68.67	135.32	158
Ogeoqeoq J06		68.77	133.77	164
Ikhil I37	EPB #193	68.78	134.13	351
East Reindeer C38		68.78	133.65	490
Kipnik O20		68.83	134.80	76
Sadene D02	EPB #281	68.85	126.79	307
Parsons P41		68.85	133.67	220
Ogruknang M31		68.85	134.42	539
Tulugak K31		68.85	135.15	73
Parsons L43	EPB #272	68.88	133.70	247
Kugpik O13	EPB #192	68.88	135.30	171
Parsons A44		68.88	133.68	352
Parsons P53		68.88	133.72	307
Kugpik L24		68.88	135.37	88
Parsons N17	EPB #275	68.95	133.57	286
Kamik F38		68.95	133.40	536
Kamik D58		68.95	133.50	317
Parsons O27		68.95	133.60	348
Atigi O48	EPB #194	68.95	133.94	509

SITE LOCATION	SITE IDENTIFIER	LAT (°N)	LONG (°W)	Base IBPF (m)
Kamik D48	EPB #273	68.95	133.46	390
Parsons F09		68.97	133.53	384
Tununuk F30		68.98	134.62	166
Tununuk K10		69.00	134.78	96
Ellice O14		69.07	135.80	38
Titalik O15		69.08	135.05	97
Titalik K26	EPB #177	69.09	135.11	55
Kurk M39		69.15	135.42	61
Unipkat	92GSCUnipkat	69.19	135.34	48
Unipkat I22	EPB #167	69.20	135.34	58
North Ellice J23	EPB #271	69.21	135.85	158
Eskimo J07		69.28	132.52	155
Kumak E58	EPB #280	69.29	135.25	217
Langley E29		69.30	135.60	67
Niglintagak M19	EPB #270	69.31	135.32	58
Niglintgak H30	EPB #173	69.32	135.34	89
Adgo C15		69.40	135.82	38
Adgo P25	EPB #255	69.42	135.84	170
Kiligvak I29		69.48	131.33	158
Amaguk H16		69.58	131.05	210
Victoria Island F36		72.75	117.18	235
Nanuk D76		73.08	123.40	603
Winter Harbour	EPB #73	74.80	110.51	384
Sarpik B35		69.40	135.38	34
Ikattok J17		69.28	136.30	162
Nektoralik K59		70.48	136.28	168
W. Hecla N52		76.37	110.85	209
Desbarats B73		76.70	105.95	86
Balaena D58		77.62	100.37	60
Cisco C42		77.35	106.28	177
Ross River School		62.00	132.50	24
Sourdough Hill	Bellekeno Mine	63.88	135.27	75
Galena Hill	Elsa Mine	63.90	135.42	90
Galena Hill	Silver King Mine	63.90	135.42	60
Mayo	recent alluvial sed	63.62	135.87	20
Mayo	RCMP compound	63.62	135.87	26
N. Parkin YT D61		66.33	137.22	61
North Cath B62	EPB #62	66.19	138.70	244
Blow River		68.77	137.45	238
Spring River YT N58		69.13	138.73	46
Roland Bay Yt L41		69.33	138.95	142

Table B2: Active layer thickness observation data accessed from CALM database ("CALM Site," 2016.).

Site Code	Site Name	Location		SITE AVERAGES OF THE ANNUAL END-OF-SEASON THAW DEPTH (cm)										
		LAT	LONG	1990	1991	1992	1993	1994	1995	1996	1997	1998	1999	2000
U2	Barrow, CRREL Plots	71 19' N	156 35' W	-	23	23	29	34	34	35	37	40	37	36
U3	Atkasuk	70 27' N	157 24' W	-	-	-	-	-	44	47	45	51	49	43
U5	West Dock 1 km grid	70 22' N	148 34' W	-	-	-	48	55	51	55	52	58	51	46
U6	Deadhorse	70 10' N	148 28' W	-	-	-	-	-	-	64	65	70	71	61
U7 A	Betty Pingo 1 km grid	70 17' N	148 52' W	-	-	-	52	54	55	55	55	60	54	47
U7 B	Betty Pingo MNT	70.2835 N	148.8928 W	-	-	-	-	-	41	44	42	44	39	37
U7 C	Betty Pingo WET	70.275 N	148.919 W	-	-	-	-	-	43	48	41	46	42	41
U9 B	Happy Valley 1 km grid	69 06' N,	148 30' W	-	-	-	44	45	43	43	48	48	44	40
U11 A	Imnavait Creek 1 km grid	68 30' N	149 30' W	-	-	56	60	60	48	45	50	56	50	44
U11 B	Imnavait Creek WET	68.611 N	149.3145 W	-	-	-	-	-	53	54	56	54	53	45
U11 C	Imnavait Creek MAT	68.611 N	149.30933 W	-	-	-	-	-	43	43	47	46	47	37
U12 A	Toolik 1 km grid	68 37' N	149 36' W	-	-	-	-	-	45	47	49	54	48	44
U12 B	Toolik MAT	68.624 N	149.61817 W	-	-	-	-	-	43	47	45	51	52	41
U13	Toolik LTER	68 37' N	149 36' W	36	28	40	46	36	43	33	46	44	45	38
U32 A	Sagwon Hills MNT	69.441 N	148.67033 W	-	-	-	-	-	60	61	58	67	59	55
U32 B	Sagwon Hills MAT	69.401 N	148.8056 W	-	-	-	-	-	40	40	40	43	41	37
U17	Wickersham	65° 16' N	148° 03' W	43	41	42	45	44	47	36	40	43	39	49
U18	Bonanza Creek LTER	64° 45' N	148° 00' W	47	49	50	*	55	58	45	50	51	40	59

Site Code	Site Name	Location		SITE AVERAGES OF THE ANNUAL END-OF-SEASON THAW DEPTH (cm)										
		LAT	LONG	1990	1991	1992	1993	1994	1995	1996	1997	1998	1999	2000
C3 A	North Head (thaw tube)	69°43'11" N	134°27'43" W	-	61	62	63	64	62	60	<66	70	66	59
C4 A	Taglu (Thaw tube)	69°22' 9" N	134°56'55" W	-	-	111	<119	118	>124	112	118	>148	>132	-
C5 A	Lousy Point (Thaw tube)	69°13' 8" N	134°17'28" W	-	81	78	80	86	85	75	<89	91	84	64
C6	Parsons Lake	68° 58' N	133° 33' W	79	80	85	84	91	89	84	90	80	75	78
C7 A	Reindeer Depot (Thaw tube)	68°41' 5" N	134° 8'45" W	-	-	127	129	132	136	134	135	140	137	134
C8 A	Rengleng River (Thaw tube)	67°47'42" N	134° 7'34" W	-	-	102	106	111	111	108	110	116	111	110
C9 A	Mountain River (Thaw tube)	65°40'25" N	128°49'45" W	-	-	58	59	62	62	58	59	62	57	59
C10	Pump Station	65° 17' N	126° 53' W	62	66	64	58	60	63	61	77	78	77	80
C12	Great Bear River	64° 55' N	125° 35' W	71	72	72	72	69	69	63	69	87	86	86
C13	Ochre River	63°27'59" N	123°41'34" W	-	-	-	<58	60	58	63	<65	66	65	65
C14 A	Willowlake River	62°41'48" N	123° 3'54" W	-	-	-	79	83	84	90	87	89	91	82
C15 A	Fort Simpson	61°53'16" N	121°36' 6" W	-	-	-	95	106	123	-	-	-	-	-
C17	Sheldrake River	56° 38' N	76° 06' W	121	134	107	131	134	-	154	157	-	-	-
C21	Marmot Mountain	52° 48' N	118° 07' W	336	352	362	220	354	272	240	192	-	342	96
R3	Marre Sale, Yamal Peninsula	69° 43' N	66° 45' E	-	-	-	-	-	131	110	92	93	92	106
R4	Parisento, Gydan Peninsula	70° 07' N	75° 35' E	-	-	82	91	-	94	-	-	-	-	-
R5	Vaskiny Dachy, Yamal Peninsula	70° 17' N	68° 54' E	-	-	-	84	85	95	89	81	93	87	92
R6	Labaz Lake, Taimyr	72° 23' N	99° 30' E	-	-	-	-	42	50	-	-	-	-	-

Site Code	Site Name	Location		SITE AVERAGES OF THE ANNUAL END-OF-SEASON THAW DEPTH (cm)										
		LAT	LONG	1990	1991	1992	1993	1994	1995	1996	1997	1998	1999	2000
R9	Cape Rogozhny; Chukotka	64° 47' N	176° 58' E	-	-	-	-	43	42	49	50	38	39	42
R10	Upper Kargoplgyno River; Chukotka	64° 05' N	177° 04' E	-	-	59	51	56	-	-	-	-	-	-
P1	Calypsos Tranda, Svalbard	77 34' N	14 30' E	135	141	140	147	-	144	134	-	137		134
S1	Kapp Linne, Svalbard	78 03' N	13 37' E	74	89	91	113	99	97	101	97	109	99	104
S2	Abisko area, Sweden	68 20' N	18 50' E	61	57	56	54	55	51	58	65	72	62	73
CH1	Murtel-Corvatsch	49 26' N	9 50' E	327	337	340	345	348	344	338	343	347	343	345
CN1	Yutulihe; Northeast China	50° 56' N	121° 20' E	-	96	100	109	112	-	-	-	-	-	-
K0	Northern Tien Shan; Cosmostation	43 05' N	76 55' E	480	510	510	470	490	480	470	480	480	490	490
K1	Northern Tien Shan; Cosmostation	43 05' N	76 55' E	450	490	460	420	500	510	490	500	500	520	510

Table B3: Borehole data for temperature of the subsurface. Further information on this dataset can be accessed from Natural Resources Canada ((Burgess & Smith, 2002; S. Smith & Burgess, 2000b)

Country Borehole ID	Responsible Investigator	Borehole Name	Longitude	Latitude	MAGT (C)	MAGT Depth (m)	Year Drilled
CA 12	S.Smith	Liard spruce/97TC4	-121.391667	61.545000	-0.1	5.0	1997
CA 13	S.Smith	Wrigley trans/97TC5	-121.883333	61.966667	1.1	10.0	1997
CA 18	S.Smith	Canyon Ck. N. Slope - T4/84-2B	-126.520556	65.232222	-1.2	8.0	1984
CA 26	S.Smith	Table Mt. C/T4/85-7C	-123.629722	63.606667	-0.8	10.0	1985
CA 33	S.Smith	Petitot River S/T4/84-6	-119.246111	59.461389	-0.4	4.0	1984
CA 35	S.Smith	Gibson Gap	-127.916667	65.766667			1989
CA 50	S.Harris	Plateau Mountain	-114.519167	50.250833	-0.6	20.0	1975
CA 61	M. Allard	Quaqtaq/HT156	-69.616667	61.033333	-3.3	19.6	1987
CA 72	S.Smith	Trail River 84-4A-T2 (off row)	-121.987222	62.070000	2.6	18.0	1984
CA 79	Environment Canada	Churchill RCT-1	-94.056222	58.758306	-1.7	14.9	1973
CA 83	S.Smith	Police Island PI-01	-125.014709	64.834156	-0.1	3.0	2007
CA 84	S.Smith	Police Island PI-02	-125.013866	64.833315	-0.3	6.4	2007
CA 85	S.Smith	Old Fort Point OFP-01	-124.837783	64.652314	-0.7	6.0	2007
CA 86	S.Smith	Little Smith LS-02	-124.732468	64.427751	-0.1	11.4	2007
CA 88	S.Smith	Saline River SR-02	-124.485264	64.287919	-0.4	20.0	2007
CA 89	S.Smith	River Between Two Mountains RBTM-01	-123.204772	62.947048	3.0	10.0	2007
CA 90	S.Smith	River Between Two Mountains RBTM-02	-123.179804	62.930989	-0.5	7.5	2007
CA 91	S.Smith	Willow Lake River WLR-01	-123.084362	62.713377	-0.5	3.4	2007
CA 92	S.Smith	Billy Creek North BCN-01	-127.473575	62.705105	-0.2	5.0	2007
CA 93	S.Smith	Oscar Creek OC-01	-127.438248	65.436571	-1.1	12.0	2007
CA 95	S.Smith	Elliot Creek EC-02	-127.621861	65.522667	-0.8	9.7	2007

Country Borehole ID	Responsible Investigator	Borehole Name	Longitude	Latitude	MAGT (C)	MAGT Depth (m)	Year Drilled
CA 96	S.Smith	Hanna River HR-01	-127.833516	65.669744	-0.8	7.0	2007
CA 97	S.Smith	Gibson Lake GL-01	-127.888145	65.747303	-0.6	20.0	2007
CA 98	S.Smith	Jackfish Creek JF-02	-128.469375	66.284942	-1.3	20.0	2007
CA 99	S.Smith	Fort Good Hope South FGHS-01	-128.495835	66.209794	-0.3	7.5	2007
CA 101	S.Smith	Snafu Creek SC-01	-128.350544	66.001887	-0.9	7.8	2007
CA 102	S.Smith	Chick Lake CL-01	-128.283929	65.895801	-2.2	12.0	2007
CA 103	S.Smith	Vermillion Creek VC-01	-126.137301	65.098087	-1.3	6.0	2007
CA 104	S.Smith	Vermillion Creek VC-02	-126.126767	65.095425	-0.3	3.5	2007
CA 105	S.Smith	Ebbutt Hill EH-01	-122.405083	62.316600			2007
CA 106	S.Smith	Trail River TR-01	-121.760000	62.089167	2.9	10.0	2007
CA 107	S.Smith	Harris River HAR-01	-121.289800	61.877100	2.5	15.0	2007
CA 108	S.Smith	Manners Sources MS-01	-121.105783	61.626583	2.9	15.0	2007
CA 109	S.Smith	Manners Sources MS-02	-121.104433	61.626583	2.5	10.0	2007
CA 110	S.Smith	Jean-Marie Creek JMC-01	-120.947817	61.439350	2.7	5.0	2007
CA 111	S.Smith	Jean-Marie Creek JMC-02	-120.948467	61.440100	2.5	5.0	2007
CA 112	S.Smith	Trout River Trout R.	-120.588533	61.019450	2.4	5.0	2007
CA 113	S.Smith	Trout Road Crossing TRC	-120.484650	60.834217	2.4	10.0	2007
CA 114	S.Smith	Steep Creek Top Steep-02	-124.374783	64.181183	1.4	15.0	2007
CA 116	S.Smith	T5 upland	-133.731883	68.992200	-5.5	10.0	2006
CA 119	S.Smith/D.Forbes	M049014Langley	-135.136009	69.083242	-0.7	12.0	2007
CA 120	S.Smith	Norris Creek NC-01	-133.290050	68.406617	-4.7	8.8	2007
CA 121	S.Smith	Campbell Lake CaL-01	-133.095650	68.242967	-1.1	4.6	2007
CA 122	S.Smith	Campbell Lake CaL-02	-133.094433	68.242950	-0.8	5.0	2007
CA 123	S.Smith	Campbell Lake CaL-03	-133.095600	68.243617	-2.4	3.0	2007
CA 124	S.Smith	North Caribou Lake NCL-01	-132.932800	68.147500	-1.6	5.0	2007
CA 125	S.Smith	North Caribou Lake NCL-02	-132.931883	68.147017	-1.5	5.0	2007

Country Borehole ID	Responsible Investigator	Borehole Name	Longitude	Latitude	MAGT (C)	MAGT Depth (m)	Year Drilled
CA 126	S.Smith	Hill Lake HL-01	-132.490517	67.989067	-1.5	5.0	2007
CA 127	S.Smith	Hill Lake HL-02	-132.490133	67.988600	-2.4	4.3	2007
CA 128	S.Smith	Wood Bridge Lake WBL-01	-132.177983	67.902133	-4.2	4.3	2007
CA 129	J.Kanigan/ S. Smith	CD100	-134.848178	68.349617	-2.0	20.3	2006
CA 134	J.Kanigan/ S. Smith	CD105	-134.687473	68.317266	-2.1	20.8	2006
CA 135	J.Kanigan/ S. Smith	CD106	-134.374303	68.711988	-1.8	20.1	2006
CA 136	J.Kanigan/ S. Smith	CD107	-134.329615	68.737934	-2.5	20.4	2006
CA 144	J.Kanigan /S.Smith	SD103A	-134.301823	67.945704	-2.9	19.8	2006
CA 161	S.Smith	84-4B	-121.986000	62.069840	1.6	18.0	1985
CA 162	S.Smith	Arctic Bay	-85.166667	73.033333	-10.6	15.0	2008
CA 163	S.Smith	Clyde River	-68.594444	70.468056	-7.2	15.0	2008
CA 164	S.Smith	Igloolik	-81.800000	69.383333	-8.5	15.0	2008
CA 171	Chris Burn	Paulatuk	-124.068889	69.350278	-6.2	27.0	2008
CA 172	S.Smith	York Factory 1TCT	-92.300000	57.000000	3.5	15.0	2007
CA 174	A. Lewkowicz	Carmacks	-136.671667	62.324722	0.3	22.5	2007
CA 175	A. Lewkowicz	Northern Dancer	-131.599722	60.008056	0.4	20.0	1978/inst 2008
CA 178	A. Lewkowicz	Mt McIntyre	-135.143333	60.622222	-1.6	20.0	2009
CA 181	Chris Burn	Old Crow	139.640300	67.926000	-3.7	16.5	2006